INHIBITION MECHANISM OF EPAC

EXAMINING THE INHIBITION MECHANISM OF AN EPAC COMPETITIVE

INHIBITOR USING NMR SPECTROSCOPY

By HONGZHAO SHAO, B.S.Chem

A Thesis Submitted to the School of Graduate Studies in Partial Fulfilment of the

Requirement for the Degree Master of Science

McMaster University MASTER OF SCIENCE (2019) Hamilton, ON (Chemistry)

TITLE: Examining the Inhibition Mechanism of an EPAC Competitive Inhibitor Using NMR Spectroscopy

AUTHOR: Hongzhao Shao, B.S.Chem (University of Minnesota, Twin Cities)

SUPERVISOR: Professor Giuseppe Melacini

NUMBER OF PAGES: xv, 102

Lay Abstract

The exchange protein activated by cAMP (EPAC) is a receptor for the classical secondary messenger cAMP. EPAC is present in multiple human systems and plays a pivotal role in the development of a wide range of diseases. In this study, we aim to establish the inhibition mechanism of a novel small molecule EPAC inhibitor/partial agonist I942 using NMR spectroscopy with the goal of achieving a better understanding of EPAC inhibition and paving the way for new small molecule EPAC inhibitors that can potentially treat EPAC-related diseases such as heart failure and diabetes.

Abstract

A novel partial agonist of the exchange protein activated by cAMP isoform 1 (EPAC1), I942, was recently discovered and shown to reduce the guanine exchange factor activity of cAMP-bound EPAC1 to approximately 10% relative to cAMP activation. However, the inhibition mechanism of I942 remains unknown. Here, we utilize NMR spectroscopy to probe the inhibitory I942 - EPAC1 interactions at atomic resolution. The EPAC1 - I942 interface was mapped through intermolecular NOEs measured by ^{15}N and ^{13}C filtered NOESY-HSQC experiment. Intermolecular NOE mapping combined with other protein NMR methods, such as saturation transfer difference, transfer Nuclear Overhauser Effect spectroscopy and chemical shift mapping, we revealed that I942 interacts with the phosphate binding cassette (PBC) and base binding region (BBR) of the EPAC1 cyclic nucleotide binding (CNB) domain, similar to cAMP. The PBC controls the conformation of the hinge region, and subsequently, allosterically shifts the hinge region between its active/inactive states. Molecular dynamics simulation based on the NMR spectroscopy data revealed that EPAC1-CNB adopts an intermediate conformation between its inactive and active states, which explains the partial agonist nature of I942.

Acknowledgements

I would like to express my appreciation to my graduate thesis supervisor Dr. Giuseppe Melacini for his patient support and understanding during to past two years. Without his help and encourage, I would have faced a much harder transition to the realm of protein nuclear magnetic resonance.

Another round of thanks goes to my fellow colleagues in the Melacini lab. I would like to specially thank Dr. Stephen Boulton, who laid the foundation to EPAC inhibitor projects in our lab and helped me start this project, Dr. Bryan VanSchouwen, who initially taught me the basis of bench work in our wet lab, and Jinfeng Huang, who helped me with simulation and modeling. Additional thanks to Dr. Madoka Akimoto, Rashik Ahmed, Olivia Byun, Naeimah Jafari and Katherine Van for the discussion and help along the way.

I would also like to thank the staff at McMaster University NMR Facility, Dr. Bob Berno, Dr. Hilary Jenkins and Megan Fair. Your help during the instrument malfunction has been valuable.

Table of Contents

Chapter 2

Chapter 3

Chapter 4

Discussion and Proposal of a Mechanism for I942 - EPAC1 Binding and Partial Agonism

List of Figures and Tables

List of Abbreviations

cAMP   3',5'-cyclic Adenosine Monophosphate

CCS   Compounded Chemical Shift

CHESCA   CHEmical Shift Covariance Analysis

CHESPA   CHEmical Shift Projection Analysis

CNB   Cyclic Nucleotide Binding domain

CR   Catalytic Region

BBR   Base Binding Region

EPAC   Exchange Protein Activated by cAMP

GEF   Guanine Exchange Factor

HSQC   Heteronuclear Single Quantum Coherence

I942   N-((2,4-dimethylphenyl)sulfonyl)-2-(naphthalen-2-yloxy)acetamide

IL   Ionic Latch

MD   Molecular Dynamics

NMR   Nuclear Magnetic Resonance

NOE   Nuclear Overhauser Effect

NOESY   Nuclear Overhauser Effect Spectroscopy

PBC   Phosphate Binding Cassette

PECAN   Protein Energetic Conformational Analysis from NMR Chemical Shifts

ROESY   Rotational frame nuclear Overhauser Effect Spectroscopy

RR   Regulatory Region

STD   Saturation Transfer Difference

STR	Saturation Transfer Reference
WT	Wild-Type
X	Fractional Activation

Declaration of Academic Achievement

The majority of NMR and fluorescence experimental work was done by the author Hongzhao Shao with the exception of some HSQC spectra for chemical shift analysis was previously acquired and published by Dr. Rajeevan Selvaratnam as well as few HSQC spectra regarding CE3F4R were acquired by Dr. Stephen Boulton and the molecular dynamics simulation was performed by Jinfeng Huang. The content was written by Hongzhao Shao and co-edited by Hongzhao Shao and Dr. Giuseppe Melacini, with the exception of the materials corresponding to the molecular dynamics simulation, which were created by Jinfeng Huang.

Chapter 1

The Exchange Protein Activated by cAMP (EPAC) and its Therapeutic Potential

1.1 EPAC and its Translational Potential

The Exchange Protein Activated by cAMP (EPAC) is a guanine exchange factor (GEF) for the Rap1 GTPase.[1,2] EPAC is a receptor for the secondary messenger cAMP and contributes to the control of cAMP signaling. There are two major isoforms of EPAC, 1 and 2, that share similar structure to a certain extent but yet different in tissue distributions and physiological functions. Structurally, EPAC2 differs from EPAC1 by including another cyclic nucleotide binding domain at the N-terminus of EPAC2 proceeding the Disheveled Egl-10 Plectstrin.[1,3] However, this additional domain is not required for GEF activity.[3] The tissue distribution of both isomers is distinctly different. EPAC2 is considerably less widely distributed than EPAC1, as EPAC2 is expressed predominately in adrenal gland and brain tissues, and to the lesser extent, heart tissues.[1] EPAC1 is more widely distributed through human system, especially in heart, kidney, prostate, ovary, pancreas, small intestine, spleen, thyroid tissues and spinal cord.[1] Notably, both isoforms are missing in liver and lung tissues as well as peripheral blood and bone marrow.[1]

EPAC has shown great potential as a therapeutic target, as it is involved in multiple physiological effects[4,5] on the nervous[6,7], cardiovascular[8–11], endocrine[12–19], digestion[20,21] and immune[22–24] systems. The regulation of EPAC activity has been hypothesized to be key in developing treatment strategies for Alzheimer's disease[25],

bacterial[22] and viral[23] infections, breast[18], ovarian cancer[12,13,17] and pancreatic cancer[20,21], cardiomyopathy[8,9], chronic pain[26,27], diabetes[14,16], drug dependence[28] and obesity[14,16,19].

The activation or suppression of the EPAC isoform 1 or 2 activity leads to different physiological outcomes due to their differential distribution in different tissues. For example, the suppression of EPAC1 activity decreases the adhesion and invasion of Rickettsiae[22], inhibits the replication of Middle East Respiratory Syndrome Coronavirus[23], reduces the migration and increases apoptosis of breast[18] and pancreatic[20,21] cancer cells, and decreases the proliferation of ovarian[17] and pancreatic[21] cancer cells, whereas inducing EPAC1 activity relieves chronic pain[26,27] and reduces cocaine dependence.[28] Decreasing in EPAC1, while increasing in G Protein Kinase 2 activity could alleviate chronic pain.[26,27] In one case of obesity, inhibiting EPAC1 activity leads to a lower risk for diabetes and obesity[14,16]. On the contrary, inhibiting EPAC2 increases the risk for obesity[19]. Thus, the strategy of EPAC drug targeting needs to be isoform specific, depending on which disease is being targeted. However, targeting EPAC1, as a more widely distributed isoform than EPAC2, could potentially serve as a valuable therapeutic approach for a broader spectrum of diseases than EPAC2.

1.2 Structural Architecture of EPAC1

The EPAC isoform 1 is organized in two major regions, the regulatory region (RR) and the catalytic region (CR), and can be furtherly separated into the Disheveled Egl-10 Plectstrin (DEP) and Cyclic Nucleotide Binding (CNB) domain within the RR, and the RAS-Exchange Motif (REM), RAS Association (RA) domain and CDC25

Homology Domain (CDC25HD) within the CR[4,5,29] (Figure 1.1). In its apo form, EPAC samples primarily a closed topology, which autoinhibits guanine exchange as the active site in the catalytic domain is occluded by the RR of EPAC which forms multiple salt bridges with the CR, collectively referred to as "ionic latch" (Figure 1.2).[30–34]

cAMP modulates EPAC allosterically by binding to the cyclic nucleotide binding (CNB) domain and changing the conformation of the hinge region on the CNB to its active form. The cAMP binding also allosterically weakens the ionic latch at the N-terminal region of EPAC1-CNB causing the release of the catalytic domain from the regulatory domain.[30–34] Upon the release of catalytic domain from the autoinhibitory RR, the catalytic domain is accessible to the Rap1 GTPase substrate, which binds to it promoting GDP to GTP exchange[1,2] (Figure 1.2). Hence, the CNB of EPAC1 serves as its central controlling unit.

The CNB domain consists of two distinct subdomains, the α-subdomain and β-subdomain. The α-subdomain starts with an N-terminal α-helical bundle (NTHB) that includes helices $\alpha1$-$\alpha4$ as well as the ionic latch forming salt bridge with the CR.[30–35] The $\alpha5$ and $\alpha6$ helices are distinct from the NTHB, with $\alpha5$ embedded within the β-barrel and $\alpha6$ located C-terminal to the β-barrel.[30,34,35] The $\alpha5$ helix is part of the phosphate binding cassette (PBC). The PBC, along with the base binding region (BBR) on the β-subdomain, are crucial for cAMP docking at the CNB domain.[30,34,35] The $\alpha6$ helix is responsible for the hinge rotation of the RR relative to the CR and ultimately for the release of the CR upon binding to cAMP.[30,34,35]

The CNB domain undergoes a distinct conformational change upon binding to cAMP. cAMP binds specifically with the PBC and the BBR and allosterically affects the conformation of the β2-β3 loop and α6 hinge helix in the EPAC1-CNB.[31,33,36] The simplest thermodynamic cycle arising from the coupling of the cAMP binding and conformational equilibria sampled by EPAC1-CNB includes four different states[37] (Figure 1.3). The interaction between cAMP and the PBC is particular important. The cAMP interacts with the PBC primarily through hydrogen bonding[34,35] (Figure 1.4) and changes the conformation of the α5 helix in the PBC from an "out" to an "in" orientation and subsequently shifts the conformation of the α6 helix (*i.e.* the hinge region) from "out" to "in"[30,34,35] (Figure 1.3). The coupling between the PBC and hinge regions relies on the L273-F300 interaction (Figure 1.4) to close the lid, release the regulatory region away from the catalytic region and ultimately activate EPAC from its autoinhibitory state.[30,31,34,35].

1.3 EPAC Inhibitor Overview

Given the potential of EPAC as a therapeutic target, over the years, several EPAC specific small molecule inhibitors were identified through high throughput screening (HTS) (Figure 1.6). The inhibitors screened exhibit a wide spectrum of inhibition mechanisms and isoform specificities. Through 8-NBD-cAMP competitive fluorescence HTS assays, the EPAC competitive inhibitors ESI-05 and ESI-07 were identified as EPAC2 specific inhibitors (ESI).[38] Through the same assay, ESI-09 was also identified as a EPAC competitive inhibitor but rather non-isoform specific[20,39] Two non-competitive

inhibitors 5225554[40] and 5376753[41] were the first inhibitors of the category screened through bioluminescence resonance energy transfer (BRET) assay and a EPAC1 specific non-competitive inhibitor AM-001[42] was also discovered through BRET assay. Interestingly, through bGDP fluorescence enzymatic HTS assay, an uncompetitive inhibitor CE3F4R was discovered and characterized to be EPAC1 specific.[43–46] Recently, a new EPAC1 specific sulfonyl acetamide named I942 was discovered through competitive fluorescence. I942 is the first ever small molecule EPAC1 specific partial agonist.[47] Currently, only sparse structural information about the complexes of EPAC with its inhibitors is available, although the uncompetitive CE3F4R inhibitor has been extensively studied through NMR spectroscopy and other methods, as explained in Section 1.4. EPAC2 was speculated as a possible target for a group of antidiabetic drugs sulfonylurea as the introduction of sulfonylurea induces insulin secretion.[48] However, it was proven that there is no direct binding between EPAC2 and sulfonylurea *in vitro*.[49,50]

1.4 Mechanism of Action of the EPAC1 Specific Uncompetitive Inhibitor CE3F4R

The mechanism of action of CE3F4R is the best understood among all the small molecular inhibitors to EPAC. CE3F4, a tetrahydroquinoline compound, was first discovered by Courilleau *et al* through the fluorescence GDP guanine exchange factor assay[43] and the (R)-enantiomer of CE3F4 was later confirmed as an EPAC1 isoform specific inhibitor[44]. What makes CE3F4 unique is that it is an uncompetitive inhibitor to EPAC1. Instead of direct binding to EPAC1, it rather binds to the cAMP-bound EPAC1 complex.[43] Upon the discovery of CE3F4, several other tetrahydroquinoline compounds

were also studied, including a range of CE3F4 analogs. Despite extensive CE3F4 derivatization, the original CE3F4R compound was confirmed to retain the best EPAC1 inhibition potential among all the tested ligands.[45]

The CE3F4R mechanism of action was investigated by NMR spectroscopy. Paramagnetic relaxation enhancement (PRE) and 2D saturation transfer difference (STD) HSQC experiments as well as chemical shift analysis revealed that, beyond the fact that CE3F4R binds to the EPAC1:cAMP complex, it also binds in proximity of the α- and β-subdomain interface.[46] Unlike the PBC/hinge inactive "out"/"out" and active "in"/"in" conformations, the binding of CE3F4R to EPAC1 stabilizes a distinct mixed intermediate with a PBC "in"/hinge "out" conformation.[46] Although PBC is locked in the "in" conformation by cAMP binding, CE3F4R binding to the EPAC1:cAMP complex forces the hinge region to the "out" conformation. The "out" conformation of the hinge region in turn keeps EPAC1 in the auto-inhibitory closed topology, whereby the catalytic region is not be released from the regulatory region.

1.5 Mechanism of Action of EPAC Non-specific Inhibitors

The non-isoform specific competitive inhibitor of EPAC, ESI-09, was one of the first EPAC inhibitors[20] and has been proven to competitively inhibit EPAC at a low concentration of 20 μM by both 8-NBD-cAMP competitive fluorescence and guanine exchange enzymatic assays.[39] However, both ESI-09 and CE3F4R discussed in Chapter 1.4 are hydrophobic compounds with low solubility and form aggregates at high

concentration which interfere with EPAC inhibition non-specifically, despite that both inhibitors can also inhibit EPAC specifically.

Although ESI-09 is a specific competitive inhibitor of EPAC, its aggregation-prone properties make it a candidate for aggregation based non-specific inhibition of EPAC[51–55], which could be alleviated by the presence of non-ionic detergents such as Triton X-100[52–60]. ESI-09 aggregates were proven to be able to form a non-specific inhibitory complex with multiple EPAC molecules.[61] Addition of non-ionic detergent Triton X-100 or human serum albumin (HSA) was able to relieve the effect of ESI-09 aggregation-based inhibition, confirming the non-specific inhibition nature of ESI-09.[61]

Besides ESI-09, the uncompetitive inhibitor CE3F4R discussed in Chapter 1.4 was also aggregation-prone and proven to be another non-specific inhibitor to EPAC.[46,61] Though both ESI-09 and CE3F4R are able to act as non-specific aggregation-based inhibitor to EPAC, their mechanisms of non-specific action are different.[61] NMR spectroscopy and dynamic light scattering revealed that ESI-09 forms aggregates that will absorb and inhibit target protein, while CE3F4R aggregate act as a sink of free ligand that promotes the protein-ligand dissociation.[61]

ESI-09 and CE3F4R were both originally discovered as EPAC specific inhibitors. However, their high hydrophobicity and low solubility in water also makes their specificity to EPAC only effective at low concentrations before aggregation forms, which limits their therapeutic potential. It is critical to find EPAC specific inhibitors that function primarily as a specific inhibitor to EPAC with minimal non-specific interactions.

1.6 Novel EPAC1 Specific Competitive Inhibitor I942

Several cAMP analogs were discovered as EPAC agonists[62–67]. Although some of the cAMP analogs are resistant to phosphodiesterase (PDE) hydrolysis[66,67], being cyclic nucleotides generally makes most of the cAMP analogs vulnerable to PDE hydrolysis, as cAMP signaling through EPAC is subject to PDE4D3 termination.[68,69] Recently, an HTS assay based on 8-NBD-cAMP competitive fluorescence with EPAC resulted in the discovery of a sulfonyl acetamide compound, a partial agonist of EPAC1, called I942 (Figure 1.6).[47] It was the first ever discovery of a non-cyclic nucleotide EPAC1 specific partial agonist, which is important for it will not enter the termination cycle of EPAC1 activation.[47] In addition, I942 is much more soluble than ESI-09 and CE3F4R, which reduces the possibility of non-specific interaction between I942 and EPAC.

Through guanine exchange factor assays, I942 was proven to be able to induce about 10-20% activity compared to cAMP-bound EPAC1.[47] Although I942 is classified as a partial agonist to EPAC1, it is also clear that I942 inhibits the EPAC1 activity induced by cAMP.[47] Furthermore, I942 affects multiple EPAC1-dependent cellular functions, including the induction of the suppressor of cytokine signalling 3 (SOCS-3), which in turn suppress the expression of interleukin 6 (IL-6) signalling, as well as the downstream expression of vascular cell adhesion molecule 1 (VCAM-1) and the monocyte adhesion to human umbilical vascular endothelial cells (HUVEC).[70] This could be utilized for the suppression of inflammatory effect from atherosclerosis and provide an alternative drug approach for the treatment of atherosclerosis.[70,71] However, to build upon

and further improve the I942 lead, it is essential to determine its mechanism of action, which is the subject of this thesis.

1.7 Thesis Outline

1.7.1 Thesis Goal

Although the competitive nature of the EPAC1 inhibition by I942 has been established[47], how EPAC1 recognizes I942 and is inhibited by it is not yet understood. Knowing the binding mechanism between I942 and EPAC1 is central to understanding how I942 competes with cAMP for the EPAC1-CNB binding pocket and for the subsequent disruption on its auto-inhibition/activation equilibrium. Such binding model is also expected to inform future EPAC1-targeted drug design based on I942. No crystal structure is currently available for either active or inactive forms of EPAC1, which makes the combination of NMR spectroscopy and molecular dynamics simulations an ideal option to examine the I942 bound structure of EPAC1 at the atomic scale.

The experimental goal of the study is to establish the binding mechanism between I942 and EPAC1. In order to do so, we need to first understand the conformation changes of both parties involved in binding before probing the interaction between the two molecules. Hence, the study is separated into three main sections: the I942 conformation as bound to EPAC1, the EPAC1-CNB conformation as bound to I942 and the I942 - EPAC1 interactions. Since currently no crystal structure of EPAC1 is available, we will address these three main sections by relying mainly on NMR spectroscopy to probe the binding between I942 and EPAC1 at atomic resolution. Transfer NOESY experiments

were used to determine the free and the bound conformation of I942 and STD NMR was utilized for group epitope mapping to gauge the proximity of each I942 proton from the surface of EPAC1-CNB, whilst the EPAC1-CNB conformational changes were mapped by chemical shift analyses, such as the CHEmical Shift Projection Analysis (CHESPA)[36,72] and the CHEmical Shift Covariance Analysis (CHESCA)[73] designed to probe the EPAC1-CNB active/inactive equilibrium and the allosteric networks perturbed by I942 binding, respectively.

To detect protein-ligand intermolecular NOEs we relied on an isotope filtered 3D-NOESY-HSQC spectrum acquired for a uniformly $^{13}C,^{15}N$-labelled protein. A ^{15}N-NOESY-HSQC was modified with two ^{13}C-isotope filters with adiabatic pulses[74,75] and an ^{15}N isotope filter[75]. In theory, any NOE peak originated from protons coupled to ^{13}C and ^{15}N should be filtered out and only NOE peaks originated from ^{12}C remain. Hence, when the protein sample is uniformly $^{15}N/^{13}C$ labelled while ligand is not, only intermolecular NOEs between protein and ligand should appear in the spectrum. The NOE measurement was supplemented by guanidine HSQC to probe the involvement of the arginine side chain in binding, as arginines are known to be critical to bind cNMPs at the PBC. With the restraints based on the intermolecular NOEs between EPAC1 and I942 and guanidine HSQC, molecular dynamics simulations enable the generation of an approximate model of the EPAC1-CNB:I942 complex. Furthermore, the structure of the EPAC1:I942 complex can be related to active/inactive models of EPAC1 and help understand how this class of competitive inhibitors of EPAC1 functions, which is necessary to design drugs targeting EPAC1.

1.7.2 Chapter Outlines

Chapter 2 focuses on the NMR methodology need to investigate EPAC1 specific competitive inhibition mechanisms. This chapter will discuss the protein expression and purification, as well as NMR sample preparation, NMR experimental parameters for HSQC, STD, STD-HSQC, NOESY and NOESY-HSQC, competitive fluorescence assays and molecular dynamics simulations in detail. The chapter will also feature some of the data analysis methods for NMR experiments, including group epitope mapping and chemical shift mapping methods CHEmical Shift Projection Analysis (CHESPA) as well as CHEmical Shift Covariance Analysis (CHESCA).

Chapter 3 features the experimental results of the study. The results are grouped in three different aspects, *i.e.* the ligand conformation, protein conformation and protein-ligand interaction. First, competitive fluorescence confirms that I942 competes with cAMP for the binding pocket on EPAC1-CNB. NOESY spectra and group epitope mapping reveal the conformation of I942 in the free and bound forms, while the chemical shift projection analysis unveils conformational changes of I942-bound EPAC1 relative to the active/inactive states. The intermolecular NOEs and the salt bridges mapped through guanidinium HSQC are used as restraints in MD simulations with the goal to build an I942-binding model. The model was then validated by STD-HSQC data and complemented by chemical shift covariance analyses.

Chapter 4 will discuss the results from the NMR and competitive fluorescence experiments, notably the stimulated binding model between I942 and EPAC1-CNB with restraints from intermolecular NOE measurement and guanidine HSQC. The binding

model will be related back to both protein and ligand conformation changes observed through NMR experiments and chemical shift analysis in order to propose a mechanism of action of I942 binding to EPAC1.

Finally, chapter 5 will focus on the conclusions and future directions for EPAC1 specific inhibitor development. Throughout the study, it is established that I942 serves as a competitive inhibitor to EPAC1 by replacing the cAMP in the cyclic nucleotide binding domain. A stimulated interaction model reveals that the two distinctive aromatic regions interact with the base binding region (BBR) and the phosphate binding cassette (PBC) separately and that the sulfonyl group on the linker between the two aromatic regions mimics the phosphate group on cAMP to form hydrogen bonding with EPAC1.

Although this thesis contributes to the elucidation of the mechanism of action for I942 as a competitive EPAC1 inhibitor, some questions remains unanswered. It is established that I942 is an isoform specific inhibitor to EPAC1 but not EPAC2.[47] The cyclic nucleotide binding domain B on EPAC2 shares similar structure with EPAC1-CNB yet I942 has shown much lower binding potential. It is also worth noticing that I942 mimics cAMP in EPAC1 binding, so the EPAC1:I942 complex has the potential to be uncompetitively inhibited by CE3F4R, another EPAC1 specific inhibitor.[46]

1.8 References

(1)   Kawasaki, H.; Springett, G. M.; Mochizuki, N.; Toki, S.; Nakaya, M.; Matsuda, M.; Housman, D. E.; Graybiel, A. M. *Science* **1998**, *282*, 2275–2279.

(2)   de Rooij, J.; Zwartkruis, F. J. T.; Verheijen, M. H. G.; Cool, R. H.; Nijman, S. M.

B.; Wittinghofer, A.; Bos, J. L. *Nature* **1998**, *396*, 474–477.

(3)   de Rooij, J.; Rehmann, H.; van Triest, M.; Cool, R. H.; Wittinghofer, A.; Bos, J. L. *J. Biol. Chem.* **2000**, *275*, 20829–20836.

(4)   Schmidt, M.; Dekker, F. J.; Maarsingh, H. *Pharmacol. Rev.* **2013**, *65*, 670–709.

(5)   Robichaux, W. G.; Cheng, X. *Physiol. Rev.* **2018**, *98*, 919–1053.

(6)   Kaneko, M.; Takahashi, T. *J. Neurosci.* **2004**, *24*, 5202–5208.

(7)   Yang, Y.; Shu, X.; Liu, D.; Shang, Y.; Wu, Y.; Pei, L.; Xu, X.; Tian, Q.; Zhang, J.; Qian, K.; Wang, Y.-X.; Petralia, R. S.; Tu, W.; Zhu, L.-Q.; Wang, J.-Z.; Lu, Y. *Neuron* **2012**, *73*, 774–788.

(8)   Morel, E.; Marcantoni, A.; Gastineau, M.; Birkedal, R.; Rochais, F.; Garnier, A.; Lompré, A.-M.; Vandecasteele, G.; Lezoualc'h, F. *Circ. Res.* **2005**, *97*, 1296–1304.

(9)   Métrich, M.; Lucas, A.; Gastineau, M.; Samuel, J.-L.; Heymes, C.; Morel, E.; Lezoualc'h, F. *Circ. Res.* **2008**, *102*, 959–965.

(10)   Laurent, A.-C.; Bisserier, M.; Lucas, A.; Tortosa, F.; Roumieux, M.; De Régibus, A.; Swiader, A.; Sainte-Marie, Y.; Heymes, C.; Vindis, C.; Lezoualc'h, F. *Cardiovasc. Res.* **2015**, *105*, 55–64.

(11)   Fazal, L.; Laudette, M.; Paula-Gomes, S.; Pons, S.; Conte, C.; Tortosa, F.; Sicard, P.; Sainte-Marie, Y.; Bisserier, M.; Lairez, O.; Lucas, A.; Roy, J.; Ghaleh, B.; Fauconnier, J.; Mialet-Perez, J.; Lezoualc'h, F. *Circ. Res.* **2017**, *120*, 645–657.

(12)   Rangarajan, S.; Enserink, J. M.; Kuiperij, H. B.; de Rooij, J.; Price, L. S.; Schwede, F.; Bos, J. L. *J. Cell Biol.* **2003**, *160*, 487–493.

(13)   Bastian, P.; Balcarek, A.; Altanis, C.; Strell, C.; Niggemann, B.; Zaenker, K. S.;

Entschladen, F. *Cancer Lett.* **2009**, *274*, 218–224.

(14)   Yan, J.; Mei, F. C.; Cheng, H.; Lao, D. H.; Hu, Y.; Wei, J.; Patrikeev, I.; Hao, D.; Stutz, S. J.; Dineley, K. T.; Motamedi, M.; Hommel, J. D.; Cunningham, K. A.; Chen, J.; Cheng, X. *Mol. Cell. Biol.* **2013**, *33*, 918–926.

(15)   Almahariq, M.; Chao, C.; Mei, F. C.; Hellmich, M. R.; Patrikeev, I.; Motamedi, M.; Cheng, X. *Mol. Pharmacol.* **2014**, *87*, 142–149.

(16)   Hu, Y.; Robichaux, W. G.; Mei, F. C.; Kim, E. R.; Wang, H.; Tong, Q.; Jin, J.; Xu, M.; Chen, J.; Cheng, X. *Mol. Cell. Biol.* **2016**, *36*, 2440–2450.

(17)   Gao, M.; Ma, Y.; Bast, R. C.; Li, Y.; Wan, L.; Liu, Y.; Sun, Y.; Fang, Z.; Zhang, L.; Wang, X.; Wei, Z. *Med. Oncol.* **2016**, *33*, 73.

(18)   Kumar, N.; Gupta, S.; Dabral, S.; Singh, S.; Sehrawat, S. *Mol. Cell. Biochem.* **2017**, *430*, 115–125.

(19)   Hwang, M.; Go, Y.; Park, J.-H.; Shin, S.-K.; Song, S. E.; Oh, B.-C.; Im, S.-S.; Hwang, I.; Jeon, Y. H.; Lee, I.-K.; Seino, S.; Song, D.-K. *Int. J. Obes.* **2017**, *41*, 279–288.

(20)   Almahariq, M.; Tsalkova, T.; Mei, F. C.; Chen, H.; Zhou, J.; Sastry, S. K.; Schwede, F.; Cheng, X. *Mol. Pharmacol.* **2013**, *83*, 122–128.

(21)   Wang, X.; Luo, C.; Cheng, X.; Lu, M. *Acta Biochim. Biophys. Sin.* **2017**, *49*, 573–580.

(22)   Gong, B.; Shelite, T.; Mei, F. C.; Ha, T.; Hu, Y.; Xu, G.; Chang, Q.; Wakamiya, M.; Ksiazek, T. G.; Boor, P. J.; Bouyer, D. H.; Popov, V. L.; Chen, J.; Walker, D. H.; Cheng, X. *Proc. Natl. Acad. Sci.* **2013**, *110*, 19615–19620.

(23) Tao, X.; Mei, F.; Agrawal, A.; Peters, C. J.; Ksiazek, T. G.; Cheng, X.; Tseng, C.-T. K. *J. Virol.* **2014**, *88*, 3902–3910.

(24) Dawn, A.; Singh, S.; More, K. R.; Siddiqui, F. A.; Pachikara, N.; Ramdani, G.; Langsley, G.; Chitnis, C. E. *PLoS Pathog.* **2014**, *10*, e1004520.

(25) McPhee, I.; Gibson, L. C. D.; Kewney, J.; Darroch, C.; Stevens, P. A.; Spinks, D.; Cooreman, A.; MacKenzie, S. J. *Biochem. Soc. Trans.* **2005**, *33*, 1330–1332.

(26) Singhmar, P.; Huo, X.; Eijkelkamp, N.; Berciano, S. R.; Baameur, F.; Mei, F. C.; Zhu, Y.; Cheng, X.; Hawke, D.; Mayor, F.; Murga, C.; Heijnen, C. J.; Kavelaars, A. *Proc. Natl. Acad. Sci.* **2016**, *113*, 3036–3041.

(27) Wang, H.; Heijnen, C. J.; van Velthoven, C. T. J.; Willemen, H. L. D. M.; Ishikawa, Y.; Zhang, X.; Sood, A. K.; Vroon, A.; Eijkelkamp, N.; Kavelaars, A. *J. Clin. Invest.* **2013**, *123*, 5023–5034.

(28) Wan, X.; Torregrossa, M. M.; Sanchez, H.; Nairn, A. C.; Taylor, J. R. *PLoS One* **2014**, *9*, e107359.

(29) Bos, J. L. *Trends Biochem. Sci.* **2006**, *31*, 680–686.

(30) Rehmann, H.; Das, J.; Knipscheer, P.; Wittinghofer, A.; Bos, J. L. *Nature* **2006**, *439*, 625–628.

(31) Mazhab-Jafari, M. T.; Das, R.; Fotheringham, S. A.; SilDas, S.; Chowdhury, S.; Melacini, G. *J. Am. Chem. Soc.* **2007**, *129*, 14482–14492.

(32) VanSchouwen, B.; Selvaratnam, R.; Fogolari, F.; Melacini, G. *J. Biol. Chem.* **2011**, *286*, 42655–42669.

(33) Das, R.; Mazhab-Jafari, M. T.; Chowdhury, S.; SilDas, S.; Selvaratnam, R.;

Melacini, G. *J. Biol. Chem.* **2008**, *283*, 19691–19703.

(34)   Rehmann, H.; Arias-Palomo, E.; Hadders, M. A.; Schwede, F.; Llorca, O.; Bos, J. L. *Nature* **2008**, *455*, 124–127.

(35)   Rehmann, H.; Prakash, B.; Wolf, E.; Rueppel, A.; de Rooij, J.; Bos, J. L.; Wittinghofer, A. *Nat. Struct. Biol.* **2003**, *10*, 26–32.

(36)   Selvaratnam, R.; VanSchouwen, B.; Fogolari, F.; Mazhab-Jafari, M. T.; Das, R.; Melacini, G. *Biophys. J.* **2012**, *102*, 630–639.

(37)   Kraemer, A.; Rehmann, H. R.; Cool, R. H.; Theiss, C.; de Rooij, J.; Bos, J. L.; Wittinghofer, A. *J. Mol. Biol.* **2001**, *306*, 1167–1177.

(38)   Tsalkova, T.; Mei, F. C.; Li, S.; Chepurny, O. G.; Leech, C. A.; Liu, T.; Holz, G. G.; Woods, V. L.; Cheng, X. *Proc. Natl. Acad. Sci.* **2012**, *109*, 18613–18618.

(39)   Zhu, Y.; Chen, H.; Boulton, S.; Mei, F.; Ye, N.; Melacini, G.; Zhou, J.; Cheng, X. *Sci. Rep.* **2015**, *5*, 9344.

(40)   Brown, L. M.; Rogers, K. E.; McCammon, J. A.; Insel, P. A. *J. Biol. Chem.* **2014**, *289*, 8217–8230.

(41)   Brown, L. M.; Rogers, K. E.; Aroonsakool, N.; McCammon, J. A.; Insel, P. A. *J. Biol. Chem.* **2014**, *289*, 29148–29157.

(42)   Laudette, M.; Coluccia, A.; Sainte-Marie, Y.; Solari, A.; Fazal, L.; Sicard, P.; Silvestri, R.; Mialet-Perez, J.; Pons, S.; Ghaleh, B.; Blondeau, J.-P.; Lezoualc'h, F. *Cardiovasc. Res.* **2019**, cvz076.

(43)   Courilleau, D.; Bisserier, M.; Jullian, J.-C.; Lucas, A.; Bouyssou, P.; Fischmeister, R.; Blondeau, J.-P.; Lezoualc'h, F. *J. Biol. Chem.* **2012**, *287*, 44192–44202.

(44)   Courilleau, D.; Bouyssou, P.; Fischmeister, R.; Lezoualc'h, F.; Blondeau, J.-P. *Biochem. Biophys. Res. Commun.* **2013**, *440*, 443–448.

(45)   Sonawane, Y. A.; Zhu, Y.; Garrison, J. C.; Ezell, E. L.; Zahid, M.; Cheng, X.; Natarajan, A. *ACS Med. Chem. Lett.* **2017**, *8*, 1183–1187.

(46)   Boulton, S.; Selvaratnam, R.; Blondeau, J.-P.; Lezoualc'h, F.; Melacini, G. *J. Am. Chem. Soc.* **2018**, *140*, 9624–9637.

(47)   Parnell, E.; McElroy, S. P.; Wiejak, J.; Baillie, G. L.; Porter, A.; Adams, D. R.; Rehmann, H.; Smith, B. O.; Yarwood, S. J. *Sci. Rep.* **2017**, *7*, 294.

(48)   Zhang, C.-L.; Katoh, M.; Shibasaki, T.; Minami, K.; Sunaga, Y.; Takahashi, H.; Yokoi, N.; Iwasaki, M.; Miki, T.; Seino, S. *Science.* **2009**, *325* (5940), 607–610.

(49)   Tsalkova, T.; Gribenko, A. V.; Cheng, X. *Assay Drug Dev. Technol.* **2011**, *9*, 88–91.

(50)   Rehmann, H. *Biochem. Soc. Trans.* **2012**, *40*, 6–10.

(51)   McGovern, S. L.; Caselli, E.; Grigorieff, N.; Shoichet, B. K. *J. Med. Chem.* **2002**, *45*, 1712–1722.

(52)   Seidler, J.; McGovern, S. L.; Doman, T. N.; Shoichet, B. K. *J. Med. Chem.* **2003**, *46*, 4477–4486.

(53)   McGovern, S. L.; Helfand, B. T.; Feng, B.; Shoichet, B. K. *J. Med. Chem.* **2003**, *46*, 4265–4272.

(54)   Feng, B. Y.; Shelat, A.; Doman, T. N.; Guy, R. K.; Shoichet, B. K. *Nat. Chem. Biol.* **2005**, *1*, 146–148.

(55)   Feng, B. Y.; Simeonov, A.; Jadhav, A.; Babaoglu, K.; Inglese, J.; Shoichet, B. K.;

Austin, C. P. *J. Med. Chem.* **2007**, *50*, 2385–2390.

(56) Coan, K. E. D.; Maltby, D. A.; Burlingame, A. L.; Shoichet, B. K. *J. Med. Chem.* **2009**, *52*, 2067–2075.

(57) Jadhav, A.; Ferreira, R. S.; Klumpp, C.; Mott, B. T.; Austin, C. P.; Inglese, J.; Thomas, C. J.; Maloney, D. J.; Shoichet, B. K.; Simeonov, A. *J. Med. Chem.* **2010**, *53*, 37–51.

(58) Baell, J. B.; Holloway, G. A. *J. Med. Chem.* **2010**, *53*, 2719–2740.

(59) Owen, S. C.; Doak, A. K.; Wassam, P.; Shoichet, M. S.; Shoichet, B. K. *ACS Chem. Biol.* **2012**, *7*, 1429–1435.

(60) Duan, D.; Doak, A. K.; Nedyalkova, L.; Shoichet, B. K. *ACS Chem. Biol.* **2015**, *10*, 978–988.

(61) Boulton, S.; Selvaratnam, R.; Ahmed, R.; Van, K.; Cheng, X.; Melacini, G. *J. Med. Chem.* **2019**, *62*, 5063–5079.

(62) Schwede, F.; Maronde, E.; Genieser, H.-G.; Jastorff, B. *Pharmacol. Ther.* **2000**, *87*, 199–226.

(63) Enserink, J. M.; Christensen, A. E.; de Rooij, J.; van Triest, M.; Schwede, F.; Genieser, H. G.; Døskeland, S. O.; Blank, J. L.; Bos, J. L. *Nat. Cell Biol.* **2002**, *4*, 901–906.

(64) Christensen, A. E.; Selheim, F.; de Rooij, J.; Dremier, S.; Schwede, F.; Dao, K. K.; Martinez, A.; Maenhaut, C.; Bos, J. L.; Genieser, H.-G.; Døskeland, S. O. *J. Biol. Chem.* **2003**, *278*, 35394–35402.

(65) Rehmann, H.; Schwede, F.; Døskeland, S. O.; Wittinghofer, A.; Bos, J. L. *J. Biol.*

Chem. **2003**, *278*, 38548–38556.

(66)   Poppe, H.; Rybalkin, S. D.; Rehmann, H.; Hinds, T. R.; Tang, X.-B.; Christensen, A. E.; Schwede, F.; Genieser, H.-G.; Bos, J. L.; Doskeland, S. O.; Beavo, J. A.; Butt, E. *Nat. Methods* **2008**, *5*, 277–278.

(67)   Vliem, M. J.; Ponsioen, B.; Schwede, F.; Pannekoek, W.-J.; Riedl, J.; Kooistra, M. R. H.; Jalink, K.; Genieser, H.-G.; Bos, J. L.; Rehmann, H. *ChemBioChem* **2008**, *9*, 2052–2054.

(68)   Dodge-Kafka, K. L.; Soughayer, J.; Pare, G. C.; Carlisle Michel, J. J.; Langeberg, L. K.; Kapiloff, M. S.; Scott, J. D. *Nature* **2005**, *437*, 574–578.

(69)   Conti, M.; Beavo, J. *Annu. Rev. Biochem.* **2007**, *76*, 481–511.

(70)   Wiejak, J.; van Basten, B.; Luchowska-Stańska, U.; Hamilton, G.; Yarwood, S. J. *Biochim. Biophys. Acta - Mol. Cell Res.* **2019**, *1866*, 264–276.

(71)   Barker, G.; Parnell, E.; van Basten, B.; Buist, H.; Adams, D.; Yarwood, S. *J. Cardiovasc. Dev. Dis.* **2017**, *4*, 22.

(72)   Byun, J. A.; Melacini, G. *Methods* **2018**, *148*, 19–27.

(73)   Selvaratnam, R.; Chowdhury, S.; VanSchouwen, B.; Melacini, G. *Proc. Natl. Acad. Sci.* **2011**, *108*, 6133–6138.

(74)   Zwahlen, C.; Legault, P.; Vincent, S. J. F.; Greenblatt, J.; Konrat, R.; Kay, L. E. *J. Am. Chem. Soc.* **1997**, *119*, 6711–6721.

(75)   Melacini, G. *J. Am. Chem. Soc.* **2000**, *122*, 9735–9738.
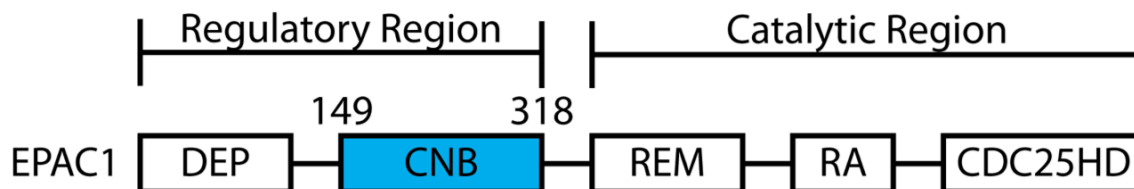
Figure 1.1 Domain organization of EPAC1. The full-length EPAC1 is organized as two major subdomains, the regulatory and catalytic regions, starting from regulatory domain of Disheveled Egl-10 Plectstrin (DEP) and Cyclic Nucleotide Binding (CNB) domain, to catalytic domain of RAS-Exchange Motif (REM), RAS Association (RA) domain and CDC25 Homology Domain (CDC25HD). The construct involved in this study is coloured blue with the starting (149) and ending (318) residue number stated above.
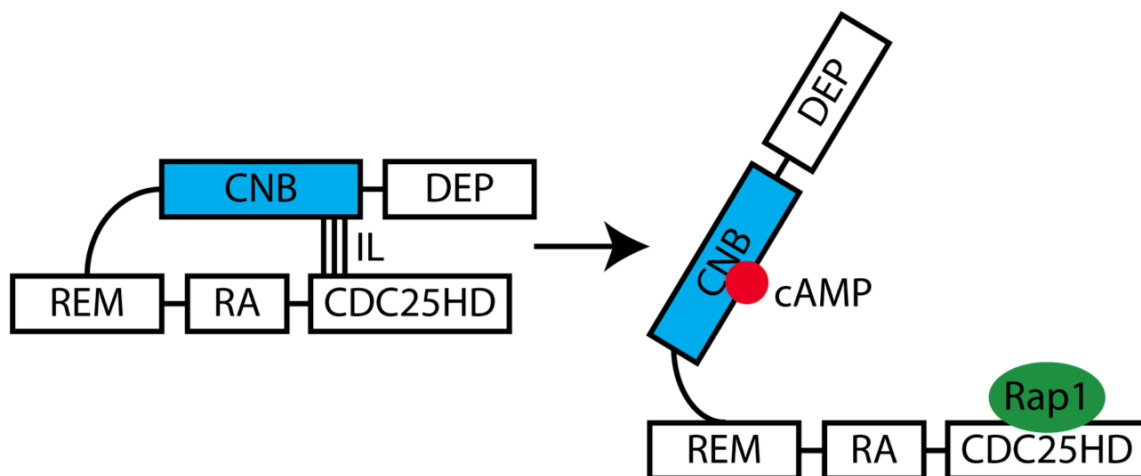
Figure 1.2 Scheme of EPAC1 activation. EPAC1 is initially in its auto-inhibition state where an ionic latch (IL) forms between the cyclic nucleotide binding domain on the regulatory domain and the CDC25 homology domain on the catalytic domain, effectively auto-inhibits EPAC. Upon binding with a cAMP on the cyclic nucleotide binding domain, EPAC1 is released from the auto-inhibition state and a Rap1 is incorporated onto the CDC25 homology domain.
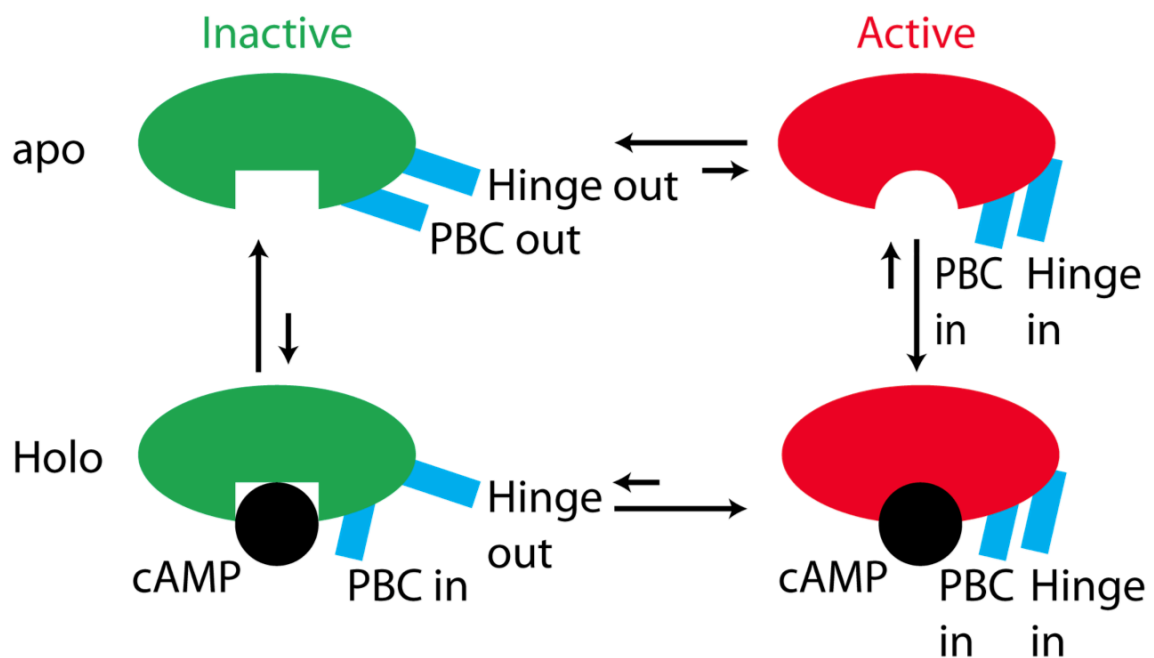
Figure 1.3 The thermodynamic cycle of cAMP binding and EPAC1-CNB active/inactive equilibrium. EPAC1-CNB is illustrated in the inactive (green) and active (red) states where the hinge region and the phosphate binding cassette (PBC) are in their "out" and "in" conformation respectively. The notable exception is the holo/inactive state where the PBC is in the "in" conformation when the hinge region is in the "out" conformation.
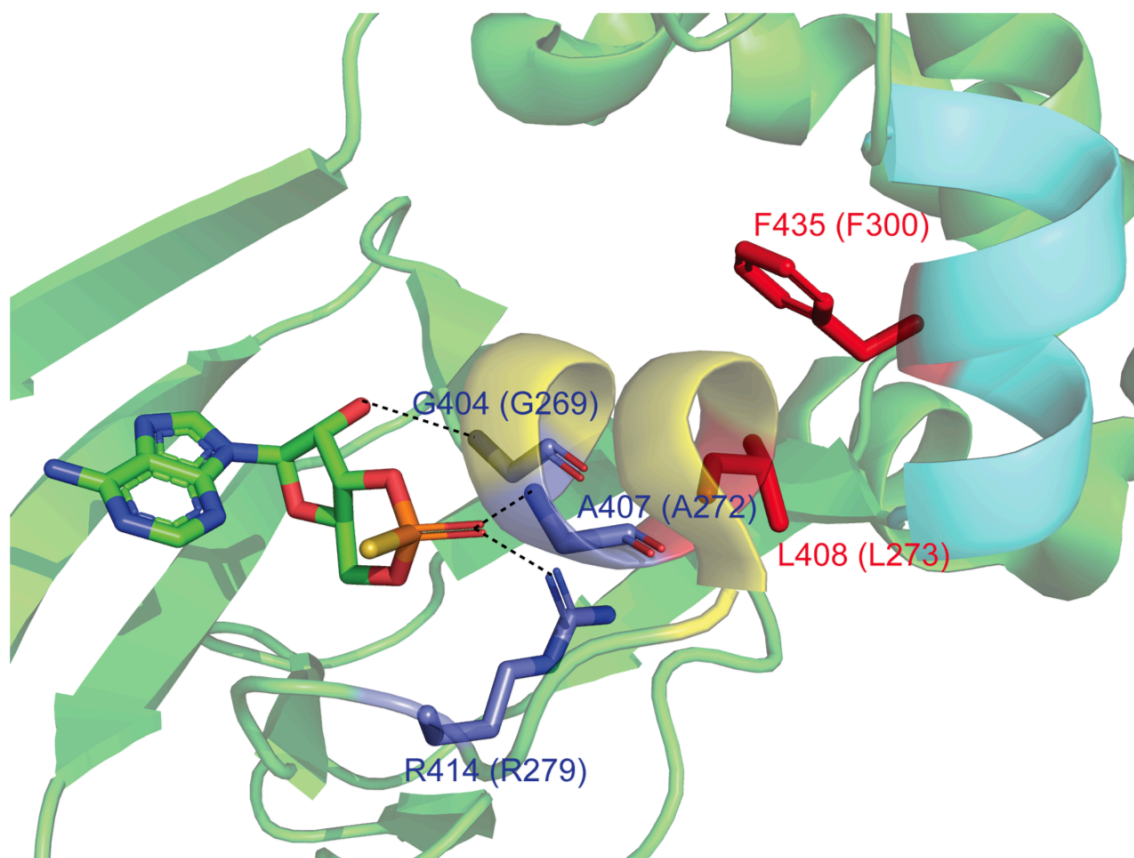
Figure 1.4 Structure highlight of Sp-cAMPS bound EPAC2-CNB.[34] Hydrogen bondings between Sp-cAMPS and EPAC2 marked with dashed blue lines. The interaction between L408 (L273 on EPAC1) on α5 helix (orange, PBC) and F435 (F300 on EPAC1) on α6 helix (purple, hinge) are highlighted with red side chains.
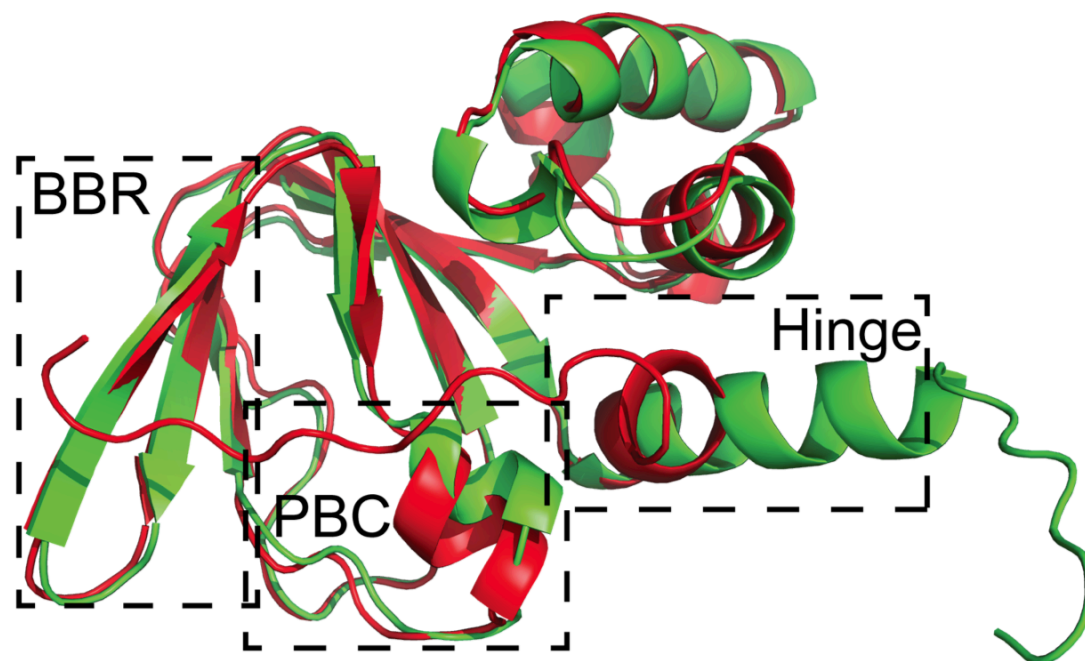
Figure 1.5 Illustration of EPAC1-CNB apo/holo structural differences. Both EPAC1 homology structures were computed from EPAC2-CNB. The dashed lines indicate the base binding region (BBR), the phosphate binding cassette (PBC) and the hinge region. The PBC and hinge region show the "out"/"in" conformation shifts from apo/inactive (green, PDB 2BYV[30]) to holo/active (red, PDB 3CF6[34]).
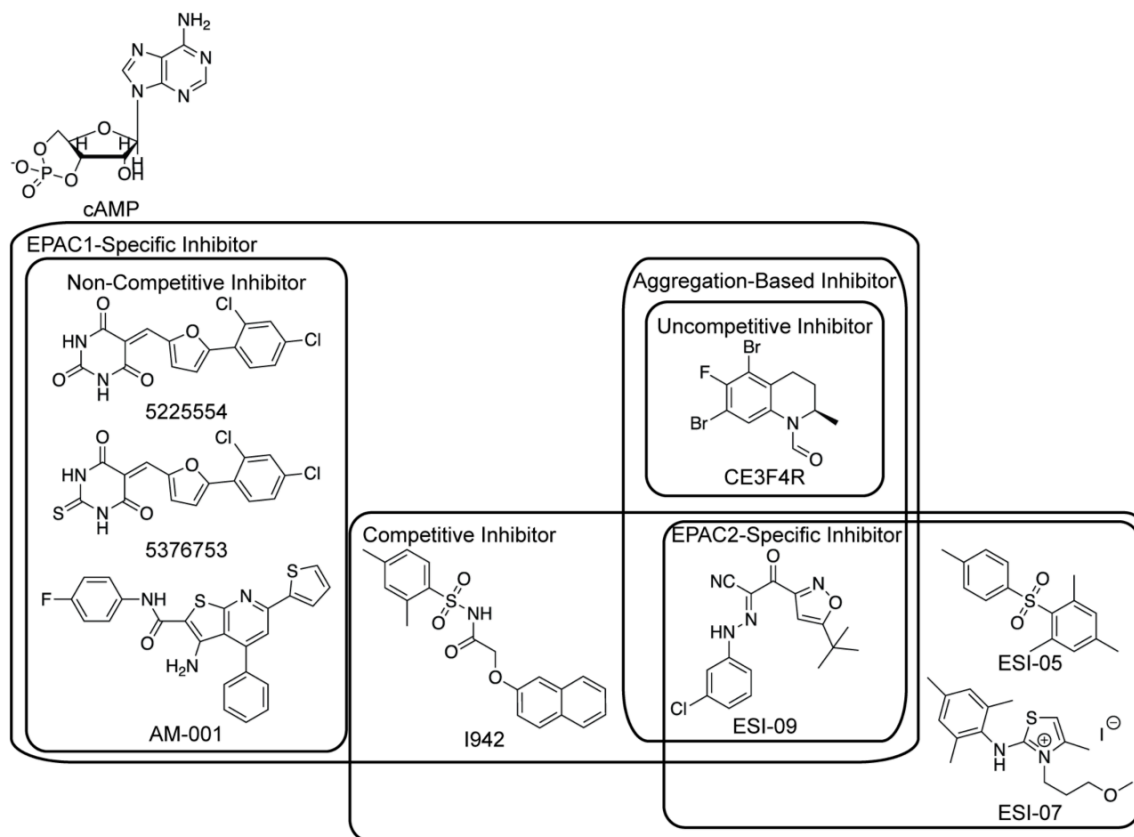
Figure 1.6 Molecular structures of cAMP and of EPAC inhibitors.

Chapter 2

Methodology of EPAC1 Specific Competitive Inhibition Mechanism Study

2.1 Protein Expression and Purification

The human EPAC1-CNB (149-318), referred here as EPAC1-CNB domain, either as wild-type, R279A or L273W mutants, was expressed and purified based on previously described protocols.[1–3] In summary, a GST (Glutathione S-transferase) tagged fusion protein clone was transformed into the *E. coli* BL21 (DE3) strain on ampicillin infused LB (Luria Broth) agar. A well-isolated colony was picked and grown in LB broth for 6 hours then inoculated in ^{15}N or ^{15}N/^{13}C labelled M9 minimal media depending on the requirement of nuclei for the NMR experiments. The inoculated culture was incubated at 37 °C until the optical density at 600 nm reached the 0.6-0.8 range. The grown culture was then induced with 0.5 mM of Isopropyl β-D-1-thiogalactopyranoside (IPTG) and incubated at 18-20 °C for 16-18 hours. Cells were harvested and lysed with a either a cell disruptor or a sonicator in a lysis buffer composed of phosphate buffered saline, 10% glycerol, 10 mM of EDTA, 1 mM of DTT, 12 μg of N_α-p-tosyl-L-lysine-chloromethyl ketone (TLCK) and N-p-tosyl-phenylalanyl-chloromethyl ketone (TPCK) and 0.24 mM of 4-(2-aminoethyl)benzenesulfonyl fluoride (AEBSF), pH 7.4. The cell lysate was purified with the Glutathione Sepharose 4B resin (GE Healthcare). First, the resin was washed with 50 mM Tris, 500 mM NaCl, 1 mM DTT, pH 8.0 and later washed and suspended in 50 mM Tris, 50 mM NaCl, 1 mM DTT, pH 7.6. The GST-tag was removed with biotinylated thrombin (EMD-Millipore) for 12-16 hours and the biotinylated

thrombin was later removed with Streptavidin Sepharose High Performance resin (GE Healthcare). The crude product was furtherly purified with the HiTrap Q HP anion exchange chromatography column (GE Healthcare) and dialyzed in 50 mM Tris, 50 mM NaCl, 1 mM DTT, pH 7.6 overnight.

2.2 NMR Sample Preparation

The final dialysis buffer mentioned in the previous paragraph was also utilized as buffer for the NMR experiments and the 8-NBD-cAMP competitive binding titration, except when a buffer devoid of detectable protons was required, as specified below. The latter is composed of 20 mM sodium phosphate buffer and 50mM NaCl in D_2O, pH 7.6. The inhibitor N-((2,4-dimethylphenyl)sulfonyl)-2-(naphthalen-2-yloxy)acetamide, also known as I942 (Life Chemicals) was dissolved in deuterated DMSO-d_6 as stock in 50mM concentration and diluted with the appropriate experiment specific buffer, as described below, when needed.

2.3 General NMR Spectroscopy

All NMR experiments were carried out on a Bruker Avance 700 MHz spectrometer equipped with a 5 mm TCI cryo-probe. Experiments were acquired at the temperature of 306 K except for ligand-based experiments, such as saturation transfer difference (STD) and 2D transfer NOESY, which were conducted at 298 K for more efficient cross-relaxation. All samples for NMR spectroscopy prepared with DMSO-d_6 had DMSO-d_6 content $\leqslant$ 2% v/v to minimize potential chemical shift perturbations from

the addition of DMSO-d$_6$[4] and all samples in non-deuterated buffer were supplied with

5% v/v of D$_2$O for locking purposes. A matching amount of DMSO-d$_6$ was added to apo

and cAMP-bound EPAC as a control for DMSO-d$_6$ induced chemical shift changes. The

1D experiments were processed and analyzed with TopSpin (Bruker) and the 2D/3D

experiments were processed with Topspin and/or NMRPipe[5] and analyzed with Sparky

(T. D. Goddard and D. G. Kneller, SPARKY 3, University of California, San Francisco).

The assignment of the I942 1D spectrum were determined based on COSY and TOCSY

experiments (Figure 2.1).

2.4 Chemical Shift Analysis

The NH-HSQC spectra of the apo, cAMP-bound and I942-bound EPAC1 samples

were acquired using 100 μM of the EPAC1-CNB domain without or with 1mM of cAMP

or I942. All HSQC samples were supplied with 60 μM of ^{15}N-Acetyl-Glycine as a

reference for alignment among different spectra. The NH-HSQC data were acquired with

1024 (^{1}H) and 128 (^{15}N) complex points, 8 scans, 16 dummy scans, spectral width of

14.0561 ppm (^{1}H) and 31.8248 ppm (^{15}N) and transmitter frequency at 4.701 ppm (^{1}H)

and 119.0 ppm (^{15}N). Peaks were assigned by comparison with previously acquired

spectra[2] and additionally acquired 3D HNCACB and CBCACONH spectra. Chemical

shifts were used in the Protein Energetic Conformational Analysis from NMR chemical

shifts (PECAN)[6] for assessing the secondary structure. The CHEmical Shift Projection

Analysis (CHESPA) was performed as previously described[7,8] with both apo and cAMP-

bound EPAC1-CNB samples supplied with 2% DMSO-d$_6$ to match the DMSO-d$_6$ content

in I942-bound EPAC1-CNB sample. The compounded chemical shift difference (ΔCCS), cosθ and fractional activation (X) (Figure 2.2) were computed as

$$\Delta CCS = \sqrt{(\Delta\delta H)^2 + (0.2 \times \Delta\delta N)^2}$$

$$cos\theta = \frac{\vec{A} \cdot \vec{B}}{|\vec{A}||\vec{B}|}$$

$$X = \frac{|\vec{A}|}{|\vec{B}|} cos\theta$$

The cosθ and fractional activation (X) were computed with a minimum cut-off of 0.05 ppm for the ΔCCS of both vectors A and B to exclude the most insignificant chemical shift differences from the analysis. The CHEmical Shift Covariance Analysis (CHESCA) was also performed with five different states: apo, cAMP or I942, 2'-OMe-cAMP, Rp-cAMPS and Sp-cAMPS bound as previously described[2,8] to probe the allosteric effect caused by I942. First, the compounded chemical shifts were calculated for each residue in every spectrum.

$$\delta = 0.2 \times \delta_N + \delta_H$$

Pair-wise residue linear correlations were then identified by computing the correlation matrix of the transpose of the residue × state CCS matrix. An absolute value Pearson correlation coefficient cut-off of 0.98 was used (Figure 2.3). The cAMP, 2'-OMe-cAMP and Sp-cAMPS samples served as active states of EPAC1-CNB, while the apo and Rp-cAMPS samples as inactive states in the CHESCA analysis. Then the cAMP-bound state was replaced with the I942-bound state. Except for I942 bound EPAC1-CNB, all spectra for the CHESCA analysis were acquired previously.[2] After the establishment

of the two matrices with cAMP or I942 along with all active and inactive states, the allosteric network differences occurring upon replacing cAMP with I942 were identified through the comparative analysis of two chemical shift correlation matrices. A control CHESCA with cAMP replaced by cAMP in I942-matching amount of DMSO-d_6 was also performed to minimize any effect caused by DMSO. The errors of I942-bound EPAC1-CNB compounded chemical shift were estimated through a technical triplicate and the errors of cAMP-bound EPAC1-CNB with matching DMSO-d_6 were calculated through previous published cAMP-bound spectra without DMSO-d_6[2] assuming DMSO-d_6 does not affect compounded chemical shifts. We also used the chemical shift correlation matrices for agglomerative clustering using Cluster 3.0[9] to find clusters that represent functional allosteric networks.

2.5 Saturation Transfer Difference (STD) and Group Epitope Mapping

The binding between EPAC1-CNB and I942 was probed by STD experiments. A 50 μM EPAC1-CNB domain sample was buffer exchanged into 20 mM sodium phosphate buffer supplied with 50 mM of NaCl, pH 7.6 in 99.9% D_2O with Zeba Spin Desalting Columns of 7K MWCO (Thermo Scientific). I942 was added to EPAC1-CNB at 300 μM. The samples were incubated at room temperature for at least 30 minutes to ensure that protein-ligand binding reached its equilibrium prior to NMR acquisition. Saturation transfer reference (STR) experiments were acquired with an off-resonance saturation at 30 ppm, whereas STD experiments were acquired with on-resonance saturation at 0.85 ppm where the methyl region of EPAC1 appears and where no I942 1D

signal is detected. The STD experiment monitors saturation transfer from EPAC1 to I942. The spectrum width was set at 11.9807 ppm with a transmitter frequency of 4.717 ppm for both STD and STR spectra. The STD experiment was performed with 512 scans and the STR experiment with 256 scans for STD experiment is less sensitive than STR, along with 8 dummy scans for both. The STD/STR signal intensity ratio for different peaks corresponding to I942 were computed and normalized to the largest STD/STR ratio to probe the binding group epitope mapping, which reflects the proximity of each proton of I942 to the surface of EPAC1.[10] A larger STD/STR ratio indicates the proton is closer to the surface of EPAC1.

2.6 2D-NOESY

The conformational changes between free and EPAC1-CNB-bound I942 were probed by NOESY and transfer NOESY experiments. 50 μM of EPAC1-CNB was buffer exchanged into the same buffer as the STD experiments with Zeba Spin Desalting Columns of 7K MWCO (Thermo Scientific) and 300 μM of I942 were added to the sample. Additional NOESY spectra of 100 μM of free I942 and 50 μM of free EPAC1-CNB were also acquired as free ligand and free protein controls respectively. All NOESY spectra were acquired with 2048 and 512 or 256 complex points in the direct and indirect dimensions, respectively, 64 dummy scans, 64 scans and spectral widths of 11.9807 ppm with a transmitter frequency of 4.696 ppm. The NOESY mixing time was 250 ms in the presence of EPAC1 and 750 ms for free I942.

2.7 Measurement of Intermolecular NOEs

Intermolecular NOEs were measured through isotopically filtered NOESY-HSQC experiment. The intermolecular NOEs between ^{15}N/^{13}C labelled EPAC1-CNB and I942 were acquired with samples in non-deuterated buffer because protein HN backbone would otherwise exchange with D_2O and eliminate any NOEs arisen from protein residues with exchangeable NH amides. ^{15}N and ^{13}C-isotopic-filters with ^{13}C adiabatic pulses were applied to the ^{15}N-NOESY-HSQC to measure intermolecular NOEs.[11,12] The experiment was acquired at 306 K with 128 dummy scans, 8 scans and complex points of 1024, 256 and 128 in the ^{1}H direct dimension, ^{1}H indirect dimension and ^{15}N dimension and spectral widths of 13.9, 14.0 and 32.0 ppm, respectively. The transmitter frequency was set at 4.7 and 119.0 for the ^{1}H and ^{15}N channels, respectively. The ^{15}N/^{13}C filtered NOESY-HSQC was acquired with a mixing time of 150 ms. We also recorded an ^{15}N-edited NOESY-HSQC spectrum on the ^{15}N,^{13}C-labeled EPAC1 (149-318) with a mixing time of 250 ms and without J_{13C-1H} refocusing or decoupling pulses to confirm the inter-molecular NOEs.

2.8 8-NBD-cAMP Competitive Binding

I942 competes with 8-(2-[7-nitro-4-benzofurazanyl]aminoethylthio)adenosine-3',5'-cyclic monophosphate (8-NBD-cAMP) for binding to the EPAC1-CNB domain and the K_d of the EPAC1-CNB:I942 complex was determined through the loss of fluorescence intensity of 8-NBD-cAMP bound to EPAC1-CNB.[13] A series of I942 samples with concentrations ranging from 0-300 μM was added to mixtures of 2.5 μM of

EPAC1-CNB and 0.5 µM of 8-NBD-cAMP in the NMR experiment buffer. The samples were incubated at room temperature for at least 30 minutes to promote protein-ligand binding equilibrium and loaded onto Corning 96 well half area plates afterwards. The plate was scanned with a Cytation 5 plate reader (BioTek) using an excitation wavelength of 485 nm and an emission wavelength of 535 nm. The competitive binding was fitted as previously described[14], which is summarized in the appendix below.

2.9 Guanidinium HSQC

The side chain guanidinium group ^{15}N signals resonates generally at around 85 ppm[15], which is usually not covered within the spectral width of routine HSQC experiments. Here, we changed the ^{15}N carrier frequency and expanded the HSQC ^{15}N spectral width to monitor the guanidinium group in arginine side chain. To evaluate the involvement of the EPAC1 Arginine 279 side chain guanidinium NH and NH_2 moieties in I942 binding, HSQC spectra with different ^{15}N dimension transmitter frequency of 80.0 ppm were acquired for wild-type apo, cAMP- and I942-bound states as well as the R279A mutant of the cAMP-bound state to assign the N-H peaks corresponding to the R279 guanidinium. To improve the signal-to-noise ratio, the number of scans was increased to 64. A guanidine HSQC of Sp-cAMPS bound wild-type EPAC1-CNB was also acquired to confirm, which NH_2 group of R279 is involved in I942 binding since the crystal structure of Sp-cAMPS bound EPAC2-CNB is known.[16]

2.10 STD-HSQC

^{13}C-STD-HSQC spectra were recorded to monitor the saturation transfer from I942 to the EPAC1-CNB domain. The ^{13}C-STD/STR-HSQC spectra were acquired in deuterated buffer in order to minimize residual water artifacts in the spectrum. Two samples of 250 µM EPAC1-CNB domain with and without 1 mM of I942 were prepared. The apo sample was prepared for saturation transfer leak through control purposes. Both the STR-HSQC and STD-HSQC spectra were acquired at 306 K with 64 dummy scans, 1024 (^{1}H) and 256 (^{13}C) complex points, spectral width of 13.0301 ppm (^{1}H) and 90.0 ppm (^{15}N) and transmitter frequencies at 1.0 ppm (^{1}H) and 39.0 ppm (^{15}N). The STR-HSQC spectrum was acquired with 8 scans, while the STD-HSQC spectrum was acquired with 64 scans as the STD-HSQC experiment is less sensitive compared to STR-HSQC. In addition, the STD-HSQC experiment was acquired with irradiation of I942 naphthalene signals to monitor saturation transfer from I942 to EPAC1.

2.11 I942 Docking and Molecular Dynamics Simulation

Both active[16] and inactive[17] EPAC1-CNB homology models were constructed using the Swiss-model server[18]. The inhibitor I942 structure was created with Open Babel[19], which was used in the following docking procedure. Docking for both active and inactive structures with I942 were performed using AutoDock Vina[20] and parameters were generated by AutoDockTools. The receptor includes rigid parts as well as flexible parts, *i.e.* the side chain of residues in the binding pocket (residues 261-264, 266-268, 270, 271, 273-276, 279). The number of modes was set to 20. The structure that best

matched the experimental intermolecular NOEs (Tables 2.1 and 2.2) was selected for subsequent MD simulations. The distances between selected residues and I942 were set based on the intensity of the NOE cross-peaks (Tables 2.1 and 2.2), while the I942 sulfur atom to the R279 guanidinium carbon atom distance was set to 5 Å based on the Sp-cAMPS phosphorus to R279 guanidinium carbon atom distance in the EPAC2 structure.

All simulations were carried out using AMBER18 (Case, D.A. *et al*, AMBER 2018, University of California, San Francisco) on the Shared Hierarchical Academic Research Computing Network (SHARCNET). The I942 geometry generated by Open Babel was optimized by conducting *ab initio* quantum mechanical calculation using the Gaussian 09 (Gaussian 09, Revision E.01, M.J. Frisch *et al*, Gaussian, Inc., Wallingford CT, 2016) at the HF/6-31G* level. Then the calculated electrostatic potentials were used to determine the partial atomic charges of I942 by using the standard restrained electrostatic potential (RESP) fitting procedure. The determined RESP charges were used for the calculation of the electrostatic energy. The general Amber force field was employed for missing force field parameters of I942. The Amber ff14SB force filed was used for all calculations. The simulations were set up to mimic the NMR experimental conditions mentioned in Chapter 2.7. All states were solvated in a rectangular box of TIP3P water molecules with minimum solute wall distance of 12 Å. The system was neutralized, and the number of ions corresponded to a NaCl concentration of 100 mM. As pH is 7.6, hydrogen atoms were added such that all Histidine side chains were in their un-ionized τ-state, and the N/C termini and all Asp, Glu, Arg and Lys side chains were in their ionized states.

The simulations were conducted whilst restraining the distance of selected EPAC1 CNB domain NH amides to the I942 ligand protons based on the inter-molecular NOEs from the filtered ^{15}N-NOESY-HSQC experiments using a 15 kcal/mol force constant. As the PBC. α-helix spanning residues 270-276 is preserved upon binding of I942, as shown by NMR secondary chemical shifts, 3 Å N-O restraints on three pairs of hydrogen bonds between the backbone N-H and C=O groups were applied with a 15 kcal/mol restraint force constant. Energy minimization was carried out prior to the equilibration simulation in the solvent for 40 ps from 0 K to 100 K in the NVT ensemble with a 5 kcal/mol restraint on backbone atoms relative to the initial structure. Subsequently, these backbone restrains were progressively relaxed. Specifically, the initial equilibration simulation was followed by 160 ps from 100 K to 306 K in the NPT ensemble with a restraint on the solute of 3 kcal/mol. Next, an equilibration simulation was implemented in the solvent for 100 ps with 1 kcal/mol restraint and followed by 100 ps equilibration without restraints. Finally, the entire system was subjected to 300 ns MD simulation at 306 K in the NPT ensemble. During the simulation, structures were saved every 20000-time steps (*i.e.* every 40 ps) for analysis purposes.

2.12 References

(1)   Mazhab-Jafari, M. T.; Das, R.; Fotheringham, S. A.; SilDas, S.; Chowdhury, S.; Melacini, G. *J. Am. Chem. Soc.* **2007**, *129*, 14482–14492.

(2)   Selvaratnam, R.; Chowdhury, S.; VanSchouwen, B.; Melacini, G. *Proc. Natl. Acad. Sci.* **2011**, *108*, 6133–6138.

(3) Boulton, S.; Selvaratnam, R.; Blondeau, J.-P.; Lezoualc'h, F.; Melacini, G. *J. Am. Chem. Soc.* **2018**, *140*, 9624–9637.

(4) Zhu, Y.; Chen, H.; Boulton, S.; Mei, F.; Ye, N.; Melacini, G.; Zhou, J.; Cheng, X. *Sci. Rep.* **2015**, *5*, 9344.

(5) Delaglio, F.; Grzesiek, S.; Vuister, G. W.; Zhu, G.; Pfeifer, J.; Bax, A. *J. Biomol. NMR* **1995**, *6*, 277–293.

(6) Eghbalnia, H. R.; Wang, L.; Bahrami, A.; Assadi, A.; Markley, J. L. *J. Biomol. NMR* **2005**, *32*, 71–81.

(7) Selvaratnam, R.; VanSchouwen, B.; Fogolari, F.; Mazhab-Jafari, M. T.; Das, R.; Melacini, G. *Biophys. J.* **2012**, *102*, 630–639.

(8) Byun, J. A.; Melacini, G. *Methods* **2018**, *148*, 19–27.

(9) de Hoon, M. J. L.; Imoto, S.; Nolan, J.; Miyano, S. *Bioinformatics* **2004**, *20*, 1453–1454.

(10) Mayer, M.; Meyer, B. *J. Am. Chem. Soc.* **2001**, *123*, 6108–6117.

(11) Zwahlen, C.; Legault, P.; Vincent, S. J. F.; Greenblatt, J.; Konrat, R.; Kay, L. E. *J. Am. Chem. Soc.* **1997**, *119*, 6711–6721.

(12) Melacini, G. *J. Am. Chem. Soc.* **2000**, *122*, 9735–9738.

(13) Tsalkova, T.; Mei, F. C.; Cheng, X. *PLoS One* **2012**, *7*, e30441.

(14) Wang, Z.-X. *FEBS Lett.* **1995**, *360*, 111–114.

(15) Yamazaki, T.; Pascal, S. M.; Singer, A. U.; Forman-Kay, J. D.; Kay, L. E. *J. Am. Chem. Soc.* **1995**, *117*, 3556–3564.

(16) Rehmann, H.; Arias-Palomo, E.; Hadders, M. A.; Schwede, F.; Llorca, O.; Bos, J.

L. *Nature* **2008**, *455*, 124–127.

(17)   Rehmann, H.; Das, J.; Knipscheer, P.; Wittinghofer, A.; Bos, J. L. *Nature* **2006**, *439*, 625–628.

(18)   Waterhouse, A.; Bertoni, M.; Bienert, S.; Studer, G.; Tauriello, G.; Gumienny, R.; Heer, F. T.; de Beer, T. A. P.; Rempfer, C.; Bordoli, L.; Lepore, R.; Schwede, T. *Nucleic Acids Res.* **2018**, *46*, W296–W303.

(19)   O'Boyle, N. M.; Banck, M.; James, C. A.; Morley, C.; Vandermeersch, T.; Hutchison, G. R. *J. Cheminform.* **2011**, *3*, 33.

(20)   Trott, O.; Olson, A. J. *J. Comput. Chem.* **2010**, *31*, 455–461.
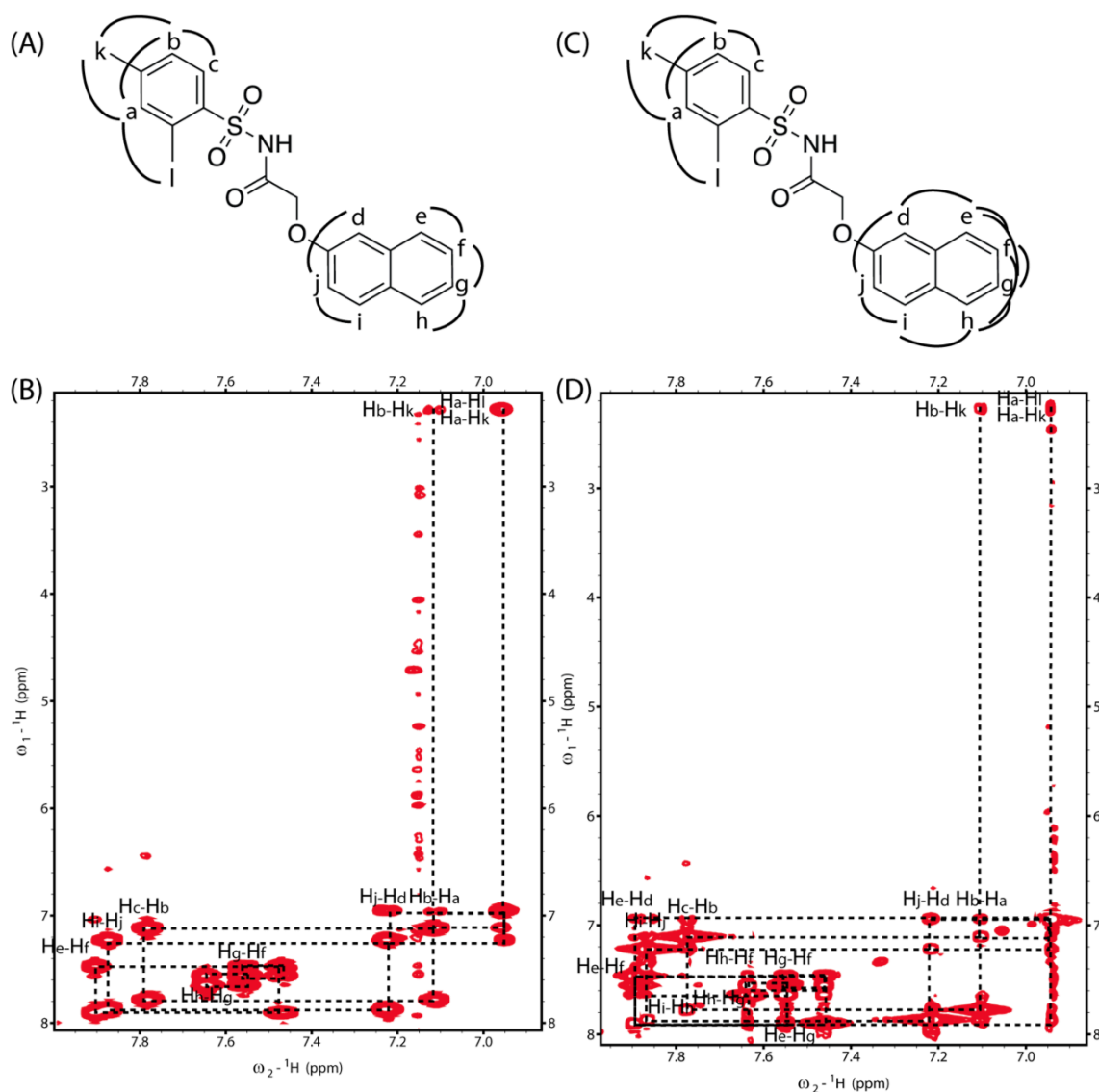
Figure 2.1 COSY and TOCSY spectra of I942. Panels B and D show the COSY and TOCSY spectra, respectively. The dashed boxes in the spectra indicates the cross-peaks between two protons of I942. Panel A and C illustrate the cross-peak from COSY and TOCSY spectra, respectively.
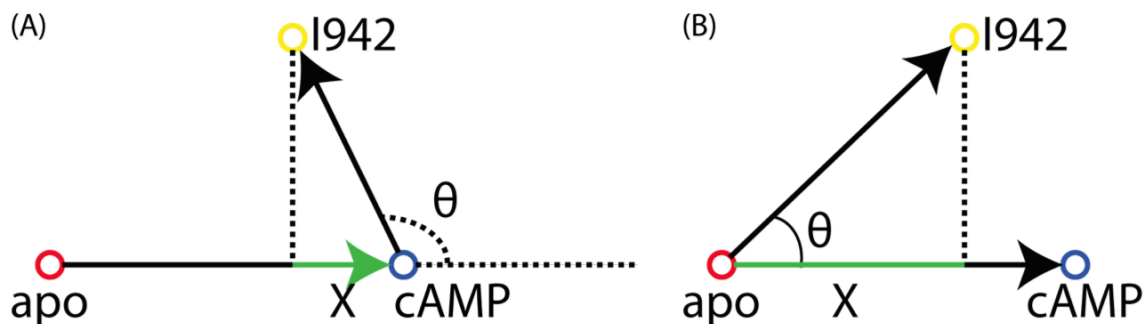
Figure 2.2 Schemes of the vectors utilized for the CHEmical Shift Projection Analysis (CHESPA). Circles represents HN-HSQC cross-peaks of the apo, cAMP- and I942-bound EPAC1-CNB domain. The green line represents the projection of the perturbation vector onto the refefence vector. (A) and (B) represents I942 as an antagonist and an agonist, respectively. X is the normalized fractional inhibition (A)/activation (B) relative to the cAMP-bound (A) or apo (B) EPAC1-CNB domain, whereas $\cos\theta$ defines the linearity of chemical shifts of the three states.
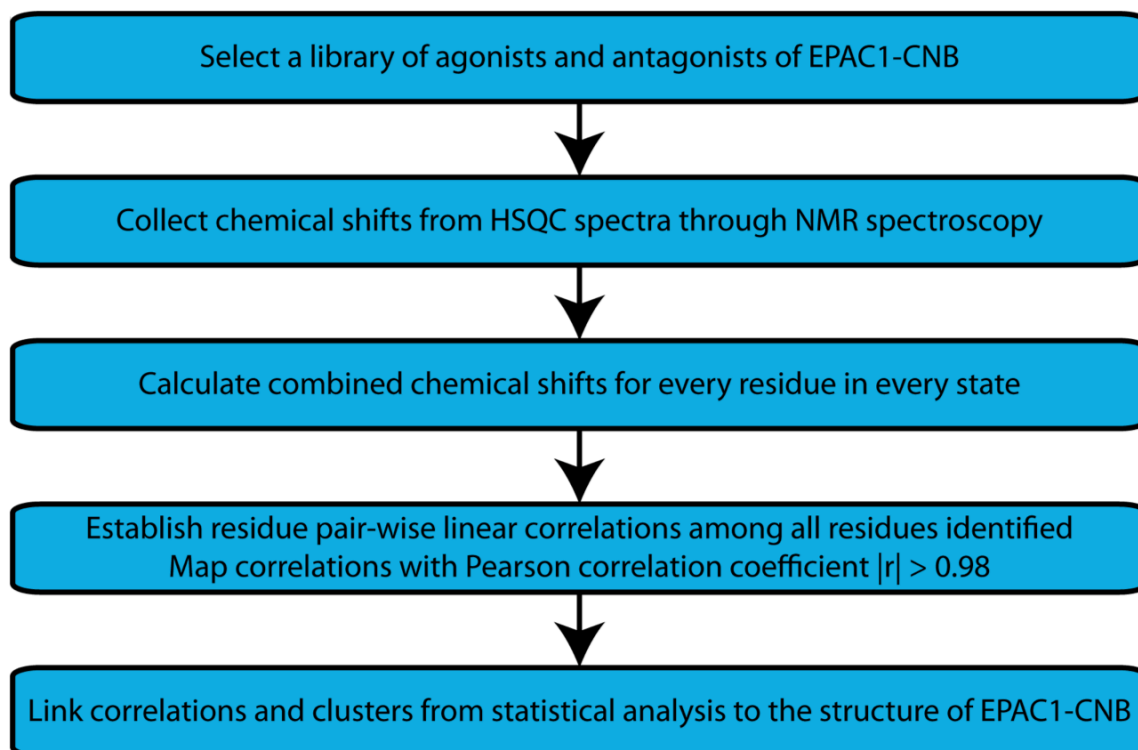
Figure 2.3 Flowchart of the CHEmical Shift Covariance Analysis (CHESCA).

Table 2.1 Distance (Å) between EPAC1 residues and I942 in docking models for active

state.

Models	A272N…C_c	A280N…C_c	A281N...C_c	A277N…C_b	A280N…C_b	T261N…C_e	Q270NE2…C_a	R279CZ...S	RMSD
Model1	7.79	5.57	4.93	12.51	5.70	17.53	12.89	8.31	5.94
Model2	8.33	9.43	9.17	14.37	10.69	16.89	10.93	9.26	6.54
Model3	5.51	4.44	5.13	8.59	4.34	10.51	10.28	7.12	[b]**3.09**
Model4	10.50	11.25	10.74	15.44	11.72	11.79	7.57	12.11	6.58
Model5	9.36	7.35	6.38	14.20	7.45	13.09	13.50	8.44	5.74
Model6	8.00	5.46	4.75	10.95	4.20	13.45	12.07	11.47	5.11
Model7	10.43	10.77	10.17	15.80	11.67	15.68	7.54	10.90	6.92
Model8	6.14	4.62	4.73	9.48	4.33	11.00	11.50	6.81	3.62
Model9	8.00	5.05	4.33	12.18	5.03	14.29	13.03	9.08	5.29
[a]**Expt**	4.00	4.00	5.00	6.00	6.00	6.00	4.00	4.97	0.00

[a] Reference distance between atoms from NOE experimental data.

[b] Docking structure selected for MD simulation.

Table 2.2 Distance (Å) between EPAC1 residues and I942 in docking models for inactive state.

Models	A272N…C_c	A280N…C_c	A281N...C_c	A277N…C_b	A280N…C_b	T261N…C_e	Q270NE2…C_a	R279CZ...S	RMSD
Model 1	7.37	8.51	9.05	10.86	7.21	10.07	6.67	12.65	4.41
Model 2	10.36	8.40	7.13	14.25	7.40	13.13	10.66	12.47	5.98
Model 3	8.36	5.52	5.51	12.33	5.95	9.08	11.42	7.65	4.08
Model 4	10.57	8.77	7.51	14.62	7.78	13.02	8.26	12.75	5.89
Model 5	6.64	4.43	4.83	10.85	4.59	8.46	10.34	10.26	3.66
Model 6	11.19	6.22	5.28	12.36	5.65	13.46	15.95	13.09	6.72
Model 7	7.22	8.14	8.26	11.45	6.96	10.86	8.06	11.64	4.38
Model 8	8.00	8.73	8.69	14.62	9.91	8.47	5.74	11.32	4.89
Model 9	11.31	8.73	7.38	16.55	9.87	11.35	9.37	11.48	6.20
Model 10	8.88	6.55	5.48	12.44	5.54	16.42	10.14	10.52	5.58
Model 11	6.22	6.07	6.44	9.98	4.97	9.18	10.03	10.03	3.54
Model 12	10.87	7.36	5.99	14.64	7.37	12.90	12.31	6.49	5.65
Model 13	10.92	8.14	7.36	15.59	9.42	9.93	13.55	8.23	6.04
Model 14	11.42	8.64	7.99	15.63	9.26	9.19	12.24	8.91	5.94
Model 15	6.62	6.75	7.03	12.38	8.13	9.61	8.29	5.05	3.45
Model 16	8.17	9.45	9.44	15.11	11.57	7.76	9.01	6.45	5.14
Model 17	6.21	6.06	6.44	9.98	4.93	11.55	9.99	10.01	3.88
Model 18	8.03	6.07	6.73	10.22	5.77	9.68	8.02	8.94	[b]**3.29**
Model 19	7.31	6.69	6.55	11.84	5.68	17.70	9.59	11.95	5.83
Model 20	9.72	6.48	5.47	12.77	5.57	16.73	10.42	8.86	5.66
[a]**Expt**	4.00	4.00	5.00	6.00	6.00	6.00	4.00	4.97	0.00

[a] Reference distance between atoms from NOE experimental data.

[b] Docking structure selected for MD simulation.

Appendix: Mathematic fitting model for 8-NBD-cAMP competitive binding (adopted from Wang, *FEBS Lett*, 1995[14])

The dissociation constant of EPAC and ligand, where A stands for 8-NBD-cAMP, B stands for the ligand (*e.g.* I942 or cAMP) and P stands for EPAC, are defined as:

$$K_{d,A} = \frac{[P][A]}{[P-A]} \quad (1)$$

$$K_{d,B} = \frac{[P][B]}{[P-B]} \quad (2)$$

If subscripted T stand for total concentration, then:

$$[A]_T = [A] + [P-A] \quad (3)$$

$$[B]_T = [B] + [P-B] \quad (4)$$

$$[P]_T = [P] + [P-A] + [P-B] \quad (5)$$

Rearranging equations 1 and 2 for equation 3 and 4, then:

$$[P-A] = \frac{[P][A]_T}{K_{d,A} + [P]} \quad (6)$$

$$[P-B] = \frac{[P][B]_T}{K_{d,B} + [P]} \quad (7)$$

Substituting equations 6 and 7 into equation 5, we obtain:

$$[P]_T = [P] + \frac{[P][A]_T}{K_{d,A} + [P]} + \frac{[P][B]_T}{K_{d,B} + [P]} \quad (8)$$

Equation 8 can be rearranged as,

$$[P]^3 + \left(K_{d,A} + K_{d,B} + [A]_T + [B]_T - [P]_T\right)[P]^2$$

$$+ \left\{K_{d,A}K_{d,B} + K_{d,B}([A]_T - [P]_T) + K_{d,A}([B]_T - [P]_T)\right\}[P]$$

$$- K_{d,A}K_{d,B}[P]_T = 0 \quad (9)$$

To simplify equation 9, we define:

$$a = K_{d,A} + K_{d,B} + [A]_T + [B]_T - [P]_T$$

$$b = K_{d,A}K_{d,B} + K_{d,B}([A]_T - [P]_T) + K_{d,A}([B]_T - [P]_T)$$

$$c = -K_{d,A}K_{d,B}[P]_T$$

$$[P]^3 + a[P]^2 + b[P] + c = 0 \quad (10)$$

Then we can solve equation 10 as,

$$[P] = -\frac{a}{3} + \frac{2}{3}\sqrt{a^2 - 3b}\cos\left(\frac{\theta}{3}\right) \quad (11)$$

where

$$\theta = arccos \frac{-2a^3 + 9ab - 27c}{2\sqrt{(a^2 - 3b)^3}}$$

So, the concentration of protein-ligand complex is calculated by substituting equation 11 into 6 and 7,

$$[P - A] = \frac{[A]_T\left\{-a + 2\sqrt{a^2 - 3b}\cos\left(\frac{\theta}{3}\right)\right\}}{3K_{d,A} - a + 2\sqrt{a^2 - 3b}\cos\left(\frac{\theta}{3}\right)} \quad (12)$$

$$[P - B] = \frac{[B]_T\left\{-a + 2\sqrt{a^2 - 3b}\cos\left(\frac{\theta}{3}\right)\right\}}{3K_{d,B} - a + 2\sqrt{a^2 - 3b}\cos\left(\frac{\theta}{3}\right)} \quad (13)$$

Assuming that the concentration of bound ligand is equal to the concentration of protein-ligand complex, the fraction of bound ligand versus total ligand concentration is determined through equation 12 and 13 divided by the total ligand concentration,

$$X_A = \frac{-a + 2\sqrt{a^2 - 3b}\cos\left(\frac{\theta}{3}\right)}{3K_{d,A} - a + 2\sqrt{a^2 - 3b}\cos\left(\frac{\theta}{3}\right)}$$

$$X_B = \frac{-a + 2\sqrt{a^2 - 3b}\cos\left(\frac{\theta}{3}\right)}{3K_{d,B} - a + 2\sqrt{a^2 - 3b}\cos\left(\frac{\theta}{3}\right)}$$

K_d was determined by finding the lowest root-square-mean deviation (RMSD) between the computed and calculated X_A values for 8-NBD-cAMP binding to the EPAC1-CNB domain during the I942 titrations.

Chapter 3

Results

3.1 I942 Competes with cAMP for Binding to EPAC1-CNB Domain

3.1.1 The EPAC1-CNB Domain Construct Recapitulates the Determinants of I942

Binding to EPAC1

As a first step towards understanding how I942 interacts with EPAC1, we measured the affinity of I942 for the EPAC1-CNB domain, *i.e.* human EPAC1 (149-318). For this purpose, the 8-NBD-cAMP analog is a convenient tool[1] since its displacement by I942 causes a loss of bound 8-NBD-cAMP fluorescence intensity. Hence, monitoring the fluorescence decrease during a I942 titration provides an effective means to measure the affinity of I942 for the EPAC1-CNB. The effective K_d between I942 and EPAC1-CNB is 6.6 ± 0.1 μM (Figure 3.1A), which is comparable to the previously published K_d between cAMP and EPAC1-CNB of 4.5 ± 0.1 μM[2], indicating that I942 is an effective competitive inhibitor of the cAMP-bound EPAC1-CNB. Furthermore, the K_d value observed for I942 and our EPAC1-CNB construct does not exceed the IC_{50} and AC_{50} values reported for I942 in the context of full length EPAC1[3], suggesting that our NMR-amenable construct adequately recapitulates the main determinants of I942 binding to longer EPAC1 constructs.

3.1.2 I942 Exhibits Comparable Affinities for the Inactive and Active States of EPAC1

We also measured the affinity of I942 for the L273W EPAC1 mutant, which is known to stabilize the inactive state of the CNB domain[4]. The L273W mutations perturbs the communication between L273 and F300, which is a residue pair critical to the control of the hinge region conformational shift upon cAMP binding. The bulky side chain on the L273W mutant effectively prevents the hinge region from adopting the "in" (or active) conformation even when cAMP binds to the PBC.[4,5] By 8-NBD-cAMP competitive fluorescence binding experiment, it was found that I942 binds to EPAC1-CNB with a K_d value of 4.9 ± 0.1 μM (Figure 3.1B). This indicates that silencing the allosteric network between the PBC and hinge regions through the L273W mutation, only affects the I942 affinity to the EPAC1-CNB marginally. Hence, I942 does not preserve the active *vs.* inactive selectivity of cAMP, which is known to bind the wild-type (WT) EPAC1-CNB with five-fold higher affinity relative to L273W[4]. These I942 *vs.* cAMP differences provide an initial explanation as to why I942 functions only as a partial agonist as opposed to a full agonist.

3.2 Binding of I942 to the EPAC1-CNB Causes a Shift of Critical Allosteric Sites towards the Inactive State

The HN-HSQC spectrum of the I942-bound EPAC1-CNB domain was assigned through comparison with the apo and cAMP-bound spectra as well as through triple-resonance spectra. The overlay of the apo, cAMP- and I942-bound EPAC1-CNB HSQCs

(Figure 3.2A) reveals that I942 causes major perturbations relative to both apo and cAMP-bound states. The residue-specific I942 *vs.* apo chemical shift changes (Figure 3.4B) indicate marked differences at the cAMP-binding sites, *i.e.* the phosphate binding cassette (PBC) and the base binding region (BBR), in agreement with the cAMP-competitive nature of the I942 ligand. Interestingly, significant I942 *vs.* apo chemical shift variations are also observed beyond the PBC and BBR, *i.e.* at allosteric sites, such as the hinge region and the β2-β3 loop (Figure 3.4B).

To gain further insight on the nature of the I942-induced perturbations, we examined also the I942 *vs.* cAMP chemical shifts (Figure 3.3), which indicate relevant differences both at the cAMP-binding and the allosteric sites[6,7]. For example, while hydrogen-bonding to the cAMP phosphate causes a major down-field ^{1}H shift for the amides of A280 and A272 in the PBC, as expected based on the H-bonds donated by these backbone amides to the cAMP phosphate, I942 causes only a marginal down-field ^{1}H shift (A280; Figure 3.2B) or an up-field ^{1}H shift (A272; Figure 3.2C), pointing to a significant weakening of the inter-molecular hydrogen-bonds donated by the corresponding amides. Considering that the hydrogen-bond with A272 is unique to the active conformation of the EPAC1-CNB[4], these differences are fully consistent with the partial agonism previously reported for I942. Overall, the preliminary comparative chemical-shift analyses of Figure 3.2 and 3.3 reveal that, while I942 targets the PBC and BBR similar to cAMP, the nature of the short-range interactions with the EPAC1-CNB is markedly different from the endogenous effector cAMP. Furthermore, the I942 *vs.* cAMP chemical shift differences at the allosteric sites (Figure 3.3B) point to variations in

long-range effects as well.

To further examine the nature of conformational changes induced by I942 binding to EPAC1-CNB, the CHEmical Shift Projection Analysis (CHESPA) was performed according to the vector definition illustrated in Figure 3.4A. Consistently negative cosθ and fractional activation values are observed at the PBC and hinge regions (Figure 3.4C & D), which suggests that I942 induces an inhibitory shift at these critical allosteric sites controlling EPAC1 activation. The shift of the PBC to the inactive state upon replacing cAMP with I942 is also supported by the overall negative CHESPA fractional activation values measured for the β2-β3 loop region, which is adjacent to the PBC (Figure 3.5B). When the EPAC1-CNB binds to cAMP, the β2-β3 loop, although not interacting directly with cAMP, is sensitive to the change in PBC conformation caused by PBC.[6] Furthermore, the hinge region, which is not a direct cAMP binding site but is allosterically coupled to the PBC through the L273-F300 side chain interaction[4,6,8], is also partially inhibited. The somewhat inhibited hinge and PBC indicate that the cAMP-bound EPAC1-CNB domain is partially shifting back to the auto-inhibited state as a result of the I942 competition. Comparing the average of partial inhibition of the PBC and hinge region, it is clear that I942 inhibits the hinge region stronger than the PBC (Figure 3.4D). By mapping the strongly inhibited (X < average) residues on the EPAC1-CNB active homology structure (Figure 3.5A), a clear pocket at cAMP binding site is identified, consistent with I942 binding to the PBC and BBR regions.

3.3 I942 Adopts Similar Conformations in its Free and EPAC1-Bound Forms

The conformational change of the ligand in the protein-ligand binding process is as important as the conformational shift of the protein receptor. To probe the conformational shift of I942 upon its binding to EPAC1-CNB, Nuclear Overhauser Effect Spectroscopy (NOESY) was applied to evaluate the binding interaction and conformation of I942 in the absence and presence of EPAC1-CNB. The NOESY spectra of EPAC1-CNB bound (Figure 3.6B) and free (Figure 3.6D) I942 reveal that I942 adopts similar conformations in these two states, suggesting minimal conformational changes in I942 upon binding to EPAC1. Furthermore, in the NOESY spectra, both 2,4-dimethylbenzyl and naphthalene ring exhibit intra-moiety NOE cross-peaks, whereas no evidence of inter-moiety NOE cross-peaks was detected, which suggests that the two distinct moieties of I942 are unlikely to interact with one another, either free or bound to EPAC1. So, I942 maintains an "open-arm" conformation regardless of whether it is free or bound to EPAC1.

3.4 The Intermolecular NOEs Reveal that the Two Aromatic Moieties of I942 are in Contact with the Two Main cAMP Binding Sites in EPAC1-CNB, *i.e.* **the PBC and BBR Regions**

The measurement of intermolecular NOEs between I942 and EPAC1-CNB is pivotal in mapping the EPAC1:I942 interface. It provides key elements of the molecular basis for the recognition of I942 by EPAC1. The intermolecular NOEs were acquired with a modified ^{15}N-NOESY-HSQC pulse program, including two ^{13}C isotope filters with

51

adiabatic pulses and an ^{15}N isotope filter. The ^{13}C,^{15}N-filtered and ^{15}N-edited experiment distinguishes protons coupled to ^{13}C/^{15}N *vs.* ^{12}C/^{14}N atoms and filters out protein-protein intramolecular NOEs within a ^{15}N/^{13}C isotopically labelled protein.[9,10] The experiment resulted in several NOE peaks originating from the backbone or side chain amides of selected PBC and BBR residues (Figure 3.7A-F). These intermolecular NOEs clearly demonstrate that the two distinct regions on I942 molecular structure interact with two different binding regions on EPAC1-CNB, *i.e.* the PBC and BBR, respectively (Figure 3.7H). More specifically, the 2',4'-dimethylbenzyl moiety mimics the ribose ring of cAMP and docks within the PBC, while the naphthalene ring mimics the adenine base of cAMP and docks at the BBR.

The engagement of both the 2',4'-dimethylbenzyl and the naphthalene moieties of I942 in forming contacts with EPAC1-CNB was independently confirmed through Saturation Transfer Difference (STD) NMR. STD NMR identifies which groups within I942 are in close contact with the EPAC1-CNB receptor. STD measures the saturation transfer from protein to ligand and the STD *vs.* STR (saturation transfer reference) intensity ratio of all protons on I942 reflects the proximity of such protons to the surface of EPAC1[11] (Figure 3.8). Figure 3.8 indicates that, although the majority of protons exhibits similar STD/STR intensity ratios, the two methyl groups on the 2,4-dimethylbenzyl moiety exhibit exceptionally low STD/STR ratios, whereas proton j on the naphthalene ring results in the highest STD/STR ratio, which reflects the closest I942 to EPAC1-CNB contact.

While the inter-molecular NOEs together with the STD data are extremely useful

to position I942 within the EPAC1-CNB, they provide only a limited number of constrains for the sulfonyl group, which is devoid of NMR detectable protons. To further probe to what extent the negative sulfonyl charge mimics the cyclic phosphate of cAMP with complemented the inter-molecular NOE measurements with mutations of the arginine residue known to form salt-bridges with cAMP phosphate, *i.e.* R279.[8]

3.5 The Sulfonyl group on I942 Mimics the Cyclic Phosphate of cAMP and Interacts with the R279 Guanidinium in EPAC1

I942 contains a sulfonyl group instead of the cyclic phosphate group of cAMP. A viable hypothesis is that the sulfonyl group forms hydrogen bonds and/or salt-bridges with the R279 side chain guanidinium group[8] similar to cAMP. To test this hypothesis, we acquired Guanidinium-HSQC spectra and we selectively assigned the R279 guanidinium group through an R279A mutant. If cAMP stabilizes the guanidinium of R279 by forming hydrogen bonding and reducing the rate of rotation of its NH_2 moieties to fall within the slow exchange limit, all five N-H signals arising from the guanidinium's two NH_2 groups and N_ε-H_ε bond are expected to be visible in the HSQC spectrum of the cAMP-bound WT EPAC1-CNB domain. These five signals should be also expected to disappear and/or move upon removal of either cAMP (*i.e.* in the WT apo sample) or the R279 guanidinium (*i.e.* in the R279A cAMP-bound sample). Figure 3.9 shows that five peaks in the Arg-HSQC spectrum of cAMP-bound EPAC1-CNB meet these criteria and were therefore assigned to the guanidinium of R279 (Figure 3.9).

Interestingly, the Arg-HSQC spectrum of I942-bound WT EPAC1-CNB preserves

the signals from only one of the two NH_2 groups of R279 observed for cAMP-bound WT EPAC1-CNB. In order to gauge the allosteric role of the two R279 NH_2 groups, we then acquired Arg-HSQC spectra for Sp-cAMPS-bound WT EPAC1-CNB. Sp-cAMPS is a well-known super-agonist of EPAC in which the axial exocyclic oxygen of the cyclic phosphate group is replaced by a sulfur atom. Sulfur is bulkier and more polarizable than oxygen and therefore perturbs hydrogen bonds and salt-bridges involving the cyclic phosphate. The comparative analysis of the Arg-HSQC spectra of the Sp-cAMPS- and I942-bound samples shows that Sp-cAMPS and I942 preserve clearly different arginine NH_2 signals, indicating that, unlike Sp-cAMPS, I942 is unable to engage the R279 NH_2 group necessary for activation, while still forming hydrogen-bonds and/or salt-bridges with the other R279 NH_2 moiety. These observations provide a further rationale to explain the molecular basis of the I942 partial agonism and provide an additional critical constraint between the R279 guanidinium and the I942 sulfonyl groups to be utilized, together with the complementary inter-molecular NOEs, as restraint in molecular dynamics (MD) simulations aimed at proposing a model for the I942:EPAC1-CNB complex. Additional restraints for the MD simulations were obtained through secondary structure analyses.

3.6 Secondary Structure Prediction Based on NMR Chemical Shifts Indicates that the α5 Helix in the PBC is Retained

Protein secondary structure can be predicted from Protein Energetic Conformational Analysis from NMR chemical shifts (PECAN) to confirm the secondary

conformational shift from addition of ligand.[12] The chemical shifts of ^{1}H and ^{15}N as well as ^{13}Cα and ^{13}Cβ from NH-HSQC and HNCACB experiments were utilized in the prediction. The prediction result (Figure 3.10) indicated that the majority of the secondary structures of cAMP-bound EPAC1-CNB are preserved upon replacement of cAMP with I942. Outliers include the N-terminal α1 and the C-terminal region after α6, where most the assignments are missing due to flexibility and lack of sufficient resolution. In addition, the α6 helix in the hinge region was partially unfolded based on this prediction similar to the cAMP-bound EPAC[8]. Another important aspect in the prediction is that the α5 helix on the PBC is retained by I942 binding. The α5 helix in the PBC is also included as a H-bond restraint for the MD simulation of the I942-bound EPAC1-CNB structure. Other secondary structure elements were reproduced by the MD simulations without the need of active restraints.

3.7 Model of the I942-Bound EPAC1-CNB Structure and Proposed I942 Mechanism of Action Based on Molecular Dynamics Simulations with Restraints from NOESY-HSQC and Guanidinium HSQC Experiments

We utilized MD simulations to propose a model for the I942-bound EPAC1-CNB structure consistent with the restrains from the intermolecular NOEs, guanidinium HSQC and secondary structure data. The simulation was performed starting from both the active and inactive EPAC1-CNB structures as I942 exhibits comparable affinities to both conformations of EPAC1. During the simulations of the active and inactive models, most of the distances for the restrained atom pairs fall within the experimental upper limits

(Figure 3.11C,D). The MD simulations also include an additional restraint not shown in this Figure (A280 NH – I942 H_b) because it is comparable to the noise level and it was consistently violated in both sets of MD simulations. Hence, new MD simulations should be run without this NOE restraint.

Comparison of the simulated I942-bound models with the original active and inactive structures of the EPAC1-CNB domain through the similarity indexes (SM) reveal that both the PBC and hinge helices are subject to a partial shift from the active to the inactive orientations (Figure 3.12A,B), which is a trend in agreement with the experimental CHESPA data. These results suggest that EPAC1-CNB adopts a third conformation in contrast to the classical "out" and "in" two-state equilibrium.

3.8 STD-HSQC Experiment Validates the Proposed Model for the I942-Bound EPAC1-CNB Structure

The ^{13}C-STD-HSQC experiment monitors saturation transfer from ligand to protein and the STD *vs.* STR intensity ratio of each residue reflects the interaction between each C-H pair and I942. The saturation was placed at 7.85 ppm close to the resonance frequency of proton e (Figure 3.8). Both the I942-bound and a control apo EPAC1-CNB STD-HSQC spectra were acquired. The apo spectrum was acquired to correct the I942-bound spectrum for saturation transfer leak throughs.

Several side chain C-Hs at or near the PBC display consistently high STD *vs.* STR intensity ratios, including A272, A277 and I283 (Table 3.1; Figure 3.13). Among these residues, A272 and A277 were identified earlier in the measurement of intermolecular

NOEs, suggesting that both backbone amide and side chain methyl groups on these two residues are involved in I942 binding. In the BBR region, the Cδ-H of L262 exhibits a significant STD *vs.* STR intensity ratio (Table 3.1). In addition, another BBR residue, V251, also displays STD *vs.* STR intensity ratios for its two Cγ-H bonds (Table 3.1; Figure 3.13). These BBR residues that interact with I942 validate the interaction between BBR and I942 described earlier based on the NOE data.

3.9 The CHEmical Shift Covariance Analysis (CHESCA) Reveals How I942 Perturbs the Allosteric Network of the EPAC1-CNB

The allosteric network within the EPAC1-CNB is critical to release EPAC1 from autoinhibition. Previously, the allosteric network of the EPAC1-CNB was identified through an NMR chemical shift analysis method called CHEmical Shift Covariance Analysis (CHESCA).[7] The previously determined correlation matrix reveals a strong correlation of the hinge region with both the PBC and the α4 helix.[7] The allosteric network between the hinge region and the PBC is critical for EPAC1 activation. The residue pair L273-F300 between the PBC and the hinge region controls the positions of the auto-inhibitory equilibrium of EPAC1[8], whereas the allosteric network between the hinge region and the adjacent α4 helix is sensitive to the orientation of the hinge region due to the similar conformation of α4 helix in the active and inactive form[4,8,13].

To examine how I942 perturbs the EPAC1-CNB allosteric network, the cAMP-bound EPAC1-CNB state was replaced with the I942-bound state and the CHESCA recomputed. A control CHESCA with cAMP-bound EPAC1-CNB including I942-

matching amount of DMSO-d_6 was also performed to minimize the potential effects arising from the addition of DMSO-d_6. Upon replacing cAMP with I942, we observed a significant loss of correlations relative to the control CHESCA (Figure 3.14A,B). Despite such loss, the I942 matrix still retains multiple correlations of the hinge region with the α4 helix as well as the PBC (Figure 3.14B). Selected correlations between the hinge and the α4 helices were either weakened or lost, *i.e.* most of the correlations between residues Q298, D299, E308 and the α4 helix were retained (Figure 3.15A,B,E,F), whereas most of the correlations between F300, N301, V307 and α4 helix were lost (Figure 3.15C,D). The correlations between the hinge region and its adjacent region, the α4 helix, are an indicator of whether the hinge region adopts a third conformation other than the common "in" or "out" orientation. Though α4 helix conformation generally is minimally affected by ligand binding at the cAMP binding pocket, the loss of correlations between the hinge region and the α4 helix suggests that the hinge region is not engaged in a simple "in"/"out" orientation equilibrium in the presence of I942.

Another critical aspect of the allosteric network regulating EPAC1 activation is the coupling between the hinge region and the PBC, which controls the orientation of the hinge (α6) helix.[4,8,13] Though the L273-F300 pair-wise correlation did not reach the absolute Pearson correlation coefficient criteria of 0.98 in the control CHESCA, it did achieved an absolute coefficient of 0.97 (Figure 3.16A). The L273-F300 pair correlation was established in the I942 matrix with an absolute Pearson correlation coefficient > 0.98 and, according to this pairwise correlation, I942 is partitioned between the inactive apo state and the agonist states, *i.e.* I942 falls in the partial activator category (Figure 3.16B).

A residue close to L273, *i.e.* N275, is another interesting case. Its correlations with F300, I303 and V307 (Figure 3.16D) were lost with the I942-CHESCA, while its correlation with E308 was retained as an activator (Figure 3.16F). Loss of correlation at the N-terminal end of α6 helix indicates that while some key residue pair correlation are present, *e.g.* L273-F300, several other interactions between the two helices are lost, confirming that the α6 helix adopts a conformation that is distinct from the traditional structures of apo and cAMP-bound EPAC1 involved in the two-state model previously proposed to explain EPAC1 activation, thus pointing to a three-state partial agonism model for I942.

3.10 References

(1)   Tsalkova, T.; Mei, F. C.; Cheng, X. *PLoS One* **2012**, *7*, e30441.

(2)   Boulton, S.; Selvaratnam, R.; Ahmed, R.; Van, K.; Cheng, X.; Melacini, G. *J. Med. Chem.* **2019**, *62*, 5063–5079.

(3)   Parnell, E.; McElroy, S. P.; Wiejak, J.; Baillie, G. L.; Porter, A.; Adams, D. R.; Rehmann, H.; Smith, B. O.; Yarwood, S. J. *Sci. Rep.* **2017**, *7*, 294.

(4)   Rehmann, H.; Prakash, B.; Wolf, E.; Rueppel, A.; de Rooij, J.; Bos, J. L.; Wittinghofer, A. *Nat. Struct. Biol.* **2003**, *10*, 26–32.

(5)   Selvaratnam, R.; VanSchouwen, B.; Fogolari, F.; Mazhab-Jafari, M. T.; Das, R.; Melacini, G. *Biophys. J.* **2012**, *102*, 630–639.

(6)   Mazhab-Jafari, M. T.; Das, R.; Fotheringham, S. A.; SilDas, S.; Chowdhury, S.; Melacini, G. *J. Am. Chem. Soc.* **2007**, *129*, 14482–14492.

(7) Selvaratnam, R.; Chowdhury, S.; VanSchouwen, B.; Melacini, G. *Proc. Natl. Acad. Sci.* **2011**, *108*, 6133–6138.

(8) Rehmann, H.; Arias-Palomo, E.; Hadders, M. A.; Schwede, F.; Llorca, O.; Bos, J. L. *Nature* **2008**, *455*, 124–127.

(9) Zwahlen, C.; Legault, P.; Vincent, S. J. F.; Greenblatt, J.; Konrat, R.; Kay, L. E. *J. Am. Chem. Soc.* **1997**, *119*, 6711–6721.

(10) Melacini, G. *J. Am. Chem. Soc.* **2000**, *122*, 9735–9738.

(11) Mayer, M.; Meyer, B. *J. Am. Chem. Soc.* **2001**, *123*, 6108–6117.

(12) Eghbalnia, H. R.; Wang, L.; Bahrami, A.; Assadi, A.; Markley, J. L. *J. Biomol. NMR* **2005**, *32*, 71–81.

(13) Rehmann, H.; Das, J.; Knipscheer, P.; Wittinghofer, A.; Bos, J. L. *Nature* **2006**, *439*, 625–628.

Table 3.1 2D STD-^{13}C-HSQC results.

Region	Residue	Resonance	STD/STR
BBR	V251	$C_{\gamma1}$-$H_{\gamma1}$	0.38 ± 0.05
		$C_{\gamma2}$-$H_{\gamma2}$	0.80 ± 0.05
	L262	C_{δ}-H_{δ}	0.58 ± 0.03
PBC	A272	C_{β}-H_{β}	0.72 ± 0.03
	A277	C_{β}-H_{β}	0.34 ± 0.02
	I283	C_{δ}-H_{δ}	0.64 ± 0.13
		C_{γ}-H_{γ}	0.52 ± 0.06
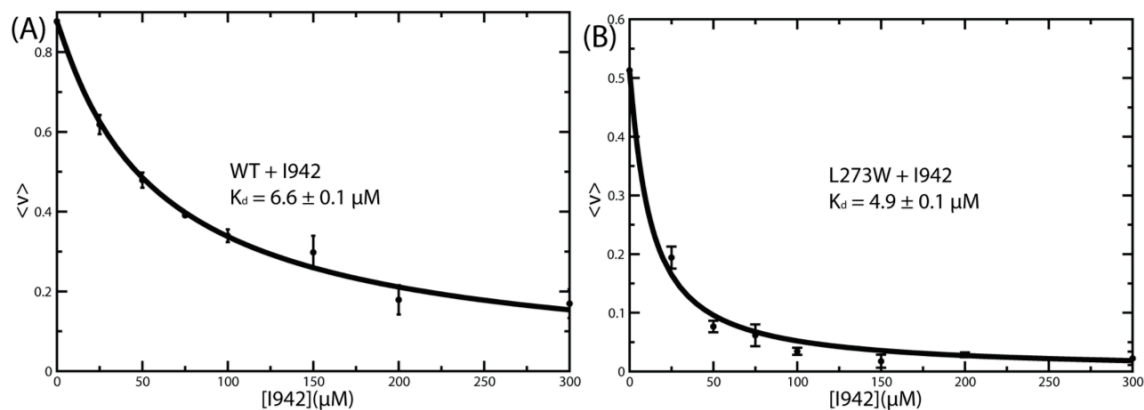
Figure 3.1 I942 *vs.* 8-NBD-cAMP Competition binding isotherms for EPAC1-CNB

monitored by fluorescence losses. (A) Binding isotherm of wild-type EPAC1-CNB and

I942. (B) As (A) but for the L273W mutant of EPAC1-CNB, which mimics the inactive
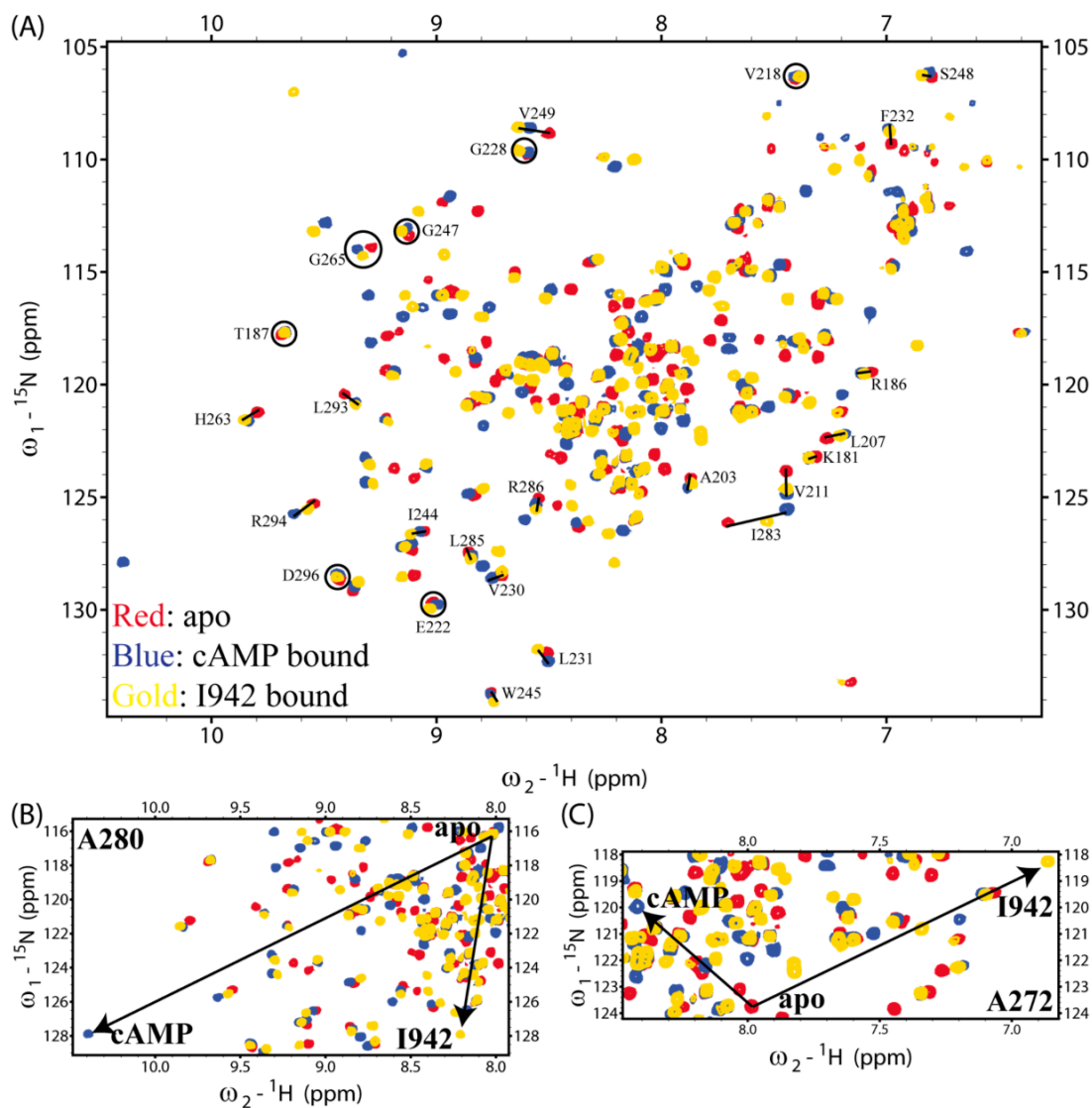
conformation of EPAC.

Figure 3.2 HSQC spectra comparison. (A) HSQC spectra of the apo, cAMP- and I942-bound EPAC1-CNB domain, shown in red, blue and gold, respectively. Lines and circles connect the cross-peaks arising from the same residue in different HSQC spectra. (B, C) Zoomed in regions, highlighting representative residues from the phosphate binding cassette (PBC) with a non-linear pattern. The amides of A280 and A272 donate hydrogen-bonds to the cAMP phosphate in the cAMP:EPAC complex.
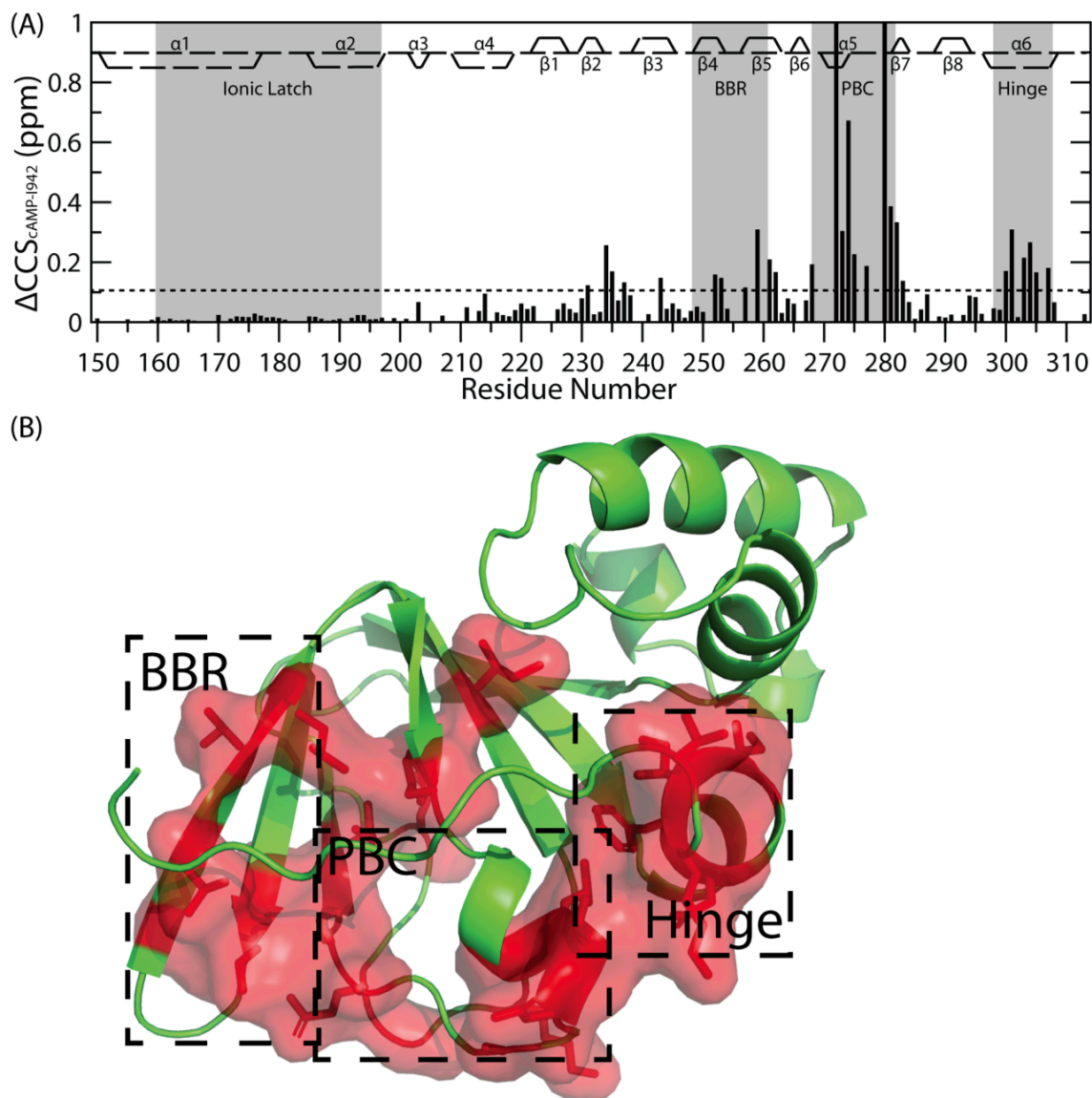
Figure 3.3 Comparision of HSQC spectra of cAMP- and I942-bound EPAC1-CNB domain. (A) CCS difference between cAMP- and I942- bound EPAC1-CNB domain. Note that any CCS over 1 ppm is off scale. Secondary structure of EPAC1 is marked on the plot along with residue number. The dashed line indicates the average ppm value over all residues. (B) 3D map of chemical shifts greater than average ppm. Such residues are marked with red surface.
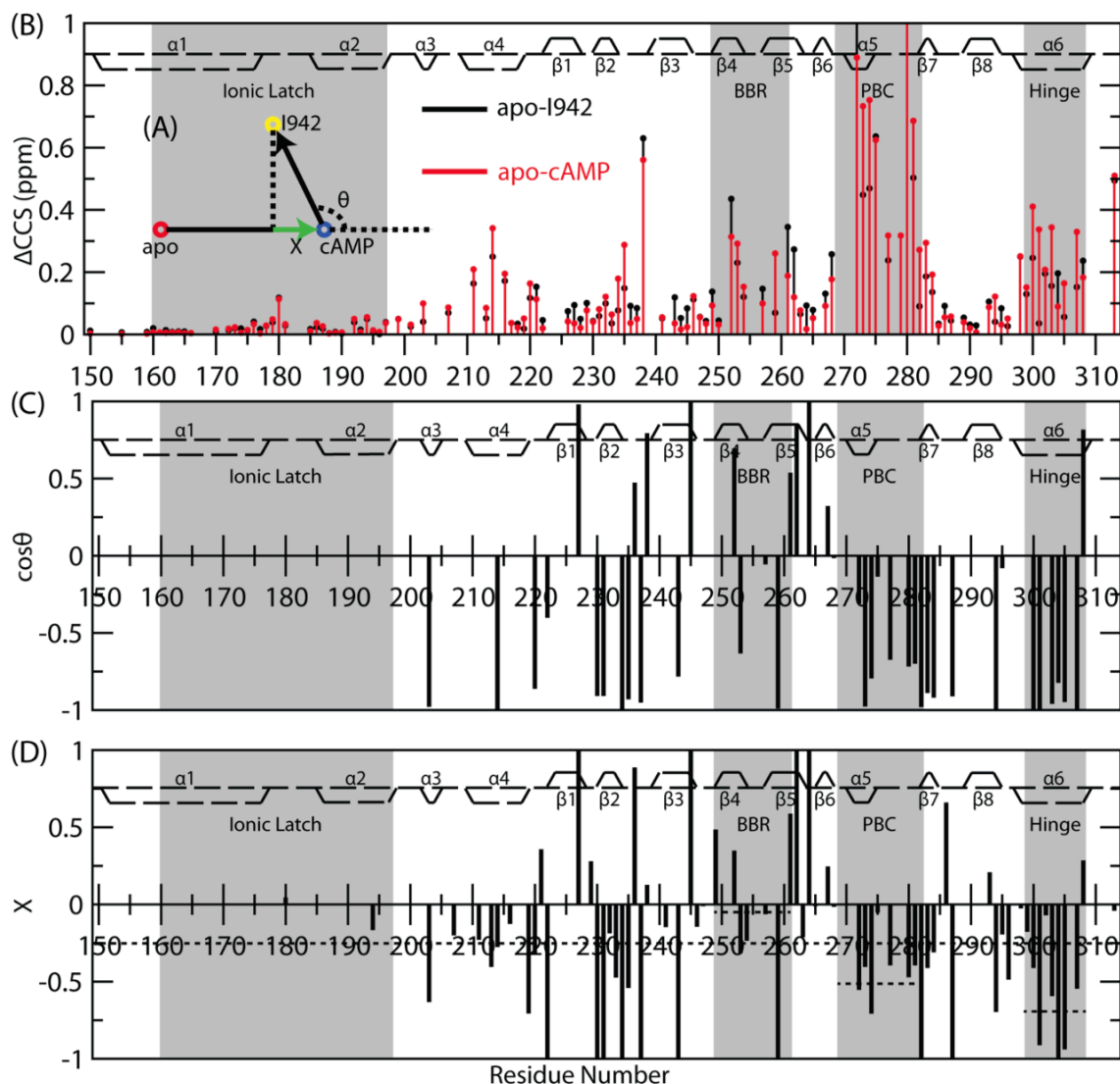
Figure 3.4 CHEmical Shift Projection Analysis (CHESPA) of I942 binding to EPAC1-CNB. All secondary structures are plotted along with residue number. (A) Vectors included in the analysis. (B) Compounded chemical shift (CCS) of cAMP (red) and I942 (black) bound EPAC1-CNB from the apo form. (C) cosθ to measure the linearity of chemical shift changes. (D) Fractional activation (X) of I942 relative to cAMP with dashed lines as overall or local average of the BBR, PBC and hinge region. Values greater than 1 or lower than -1 are off-scale.
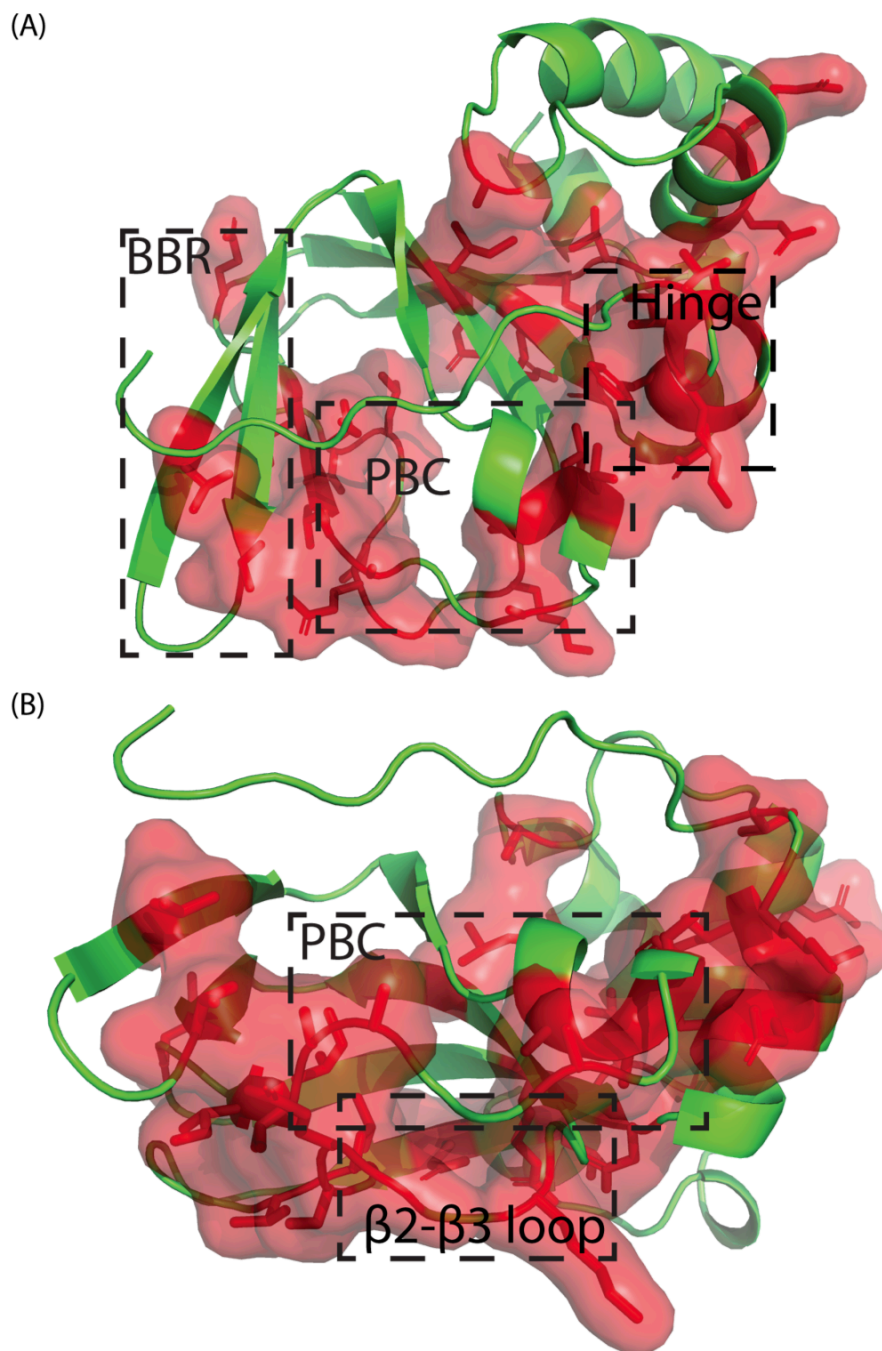
Figure 3.5 3D map of CHESPA result. (A) X lower than average were mapped red. (B)

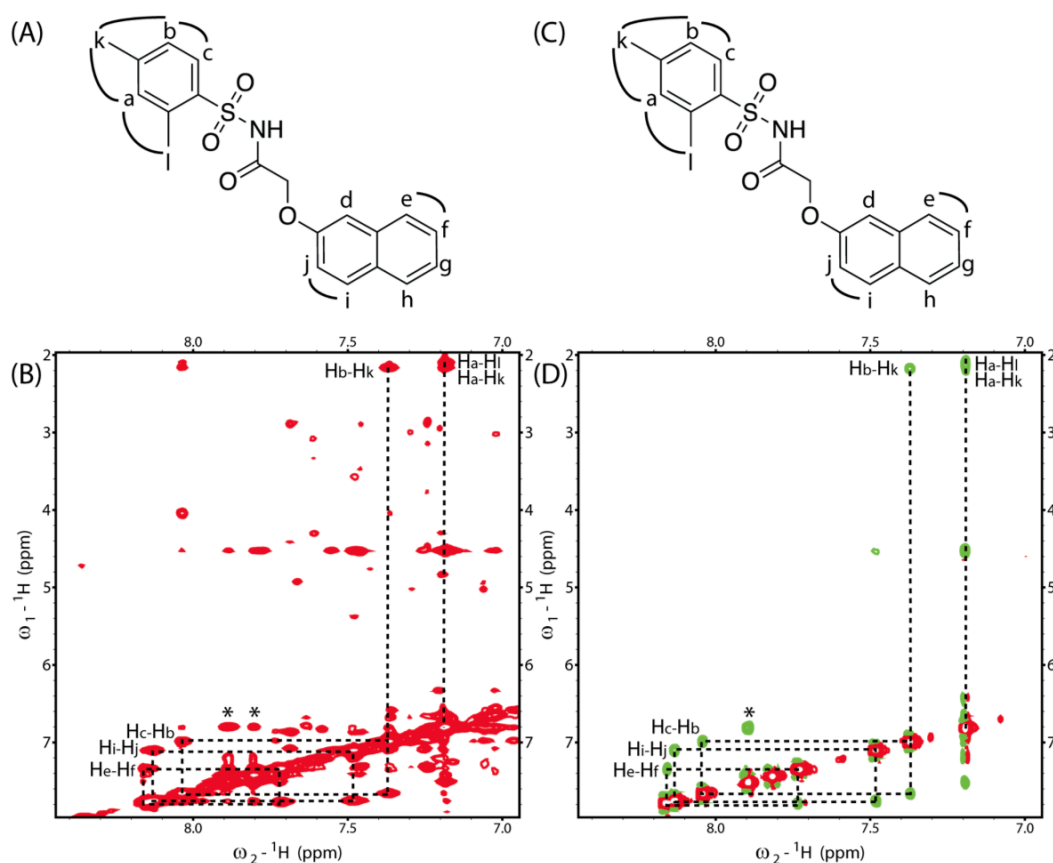As (A), but in a different orientation to display the β2-β3 loop.

Figure 3.6 Intra-ligand NOEs for EPAC1-CNB domain-bound (A, B) and free (C, D) I942. Panels B and D show NOESY spectra acquired in the presence and absence of EPAC1-CNB contruct, respectively. Dashed boxes indicate NOE cross-peaks between two protons of I942. In the presence of EPAC1 the transfer NOE effect prevails generating cross-peaks of the same sign as the diagonal, whereas in the absence of EPAC1 opposite signs are observed due to the fast tumbling of free I942. The asterisks indicate peaks that may be false positives due to spin diffusion, as indentified by a ROESY experiment with mixing time of 25ms for the EPAC1-bound I942.
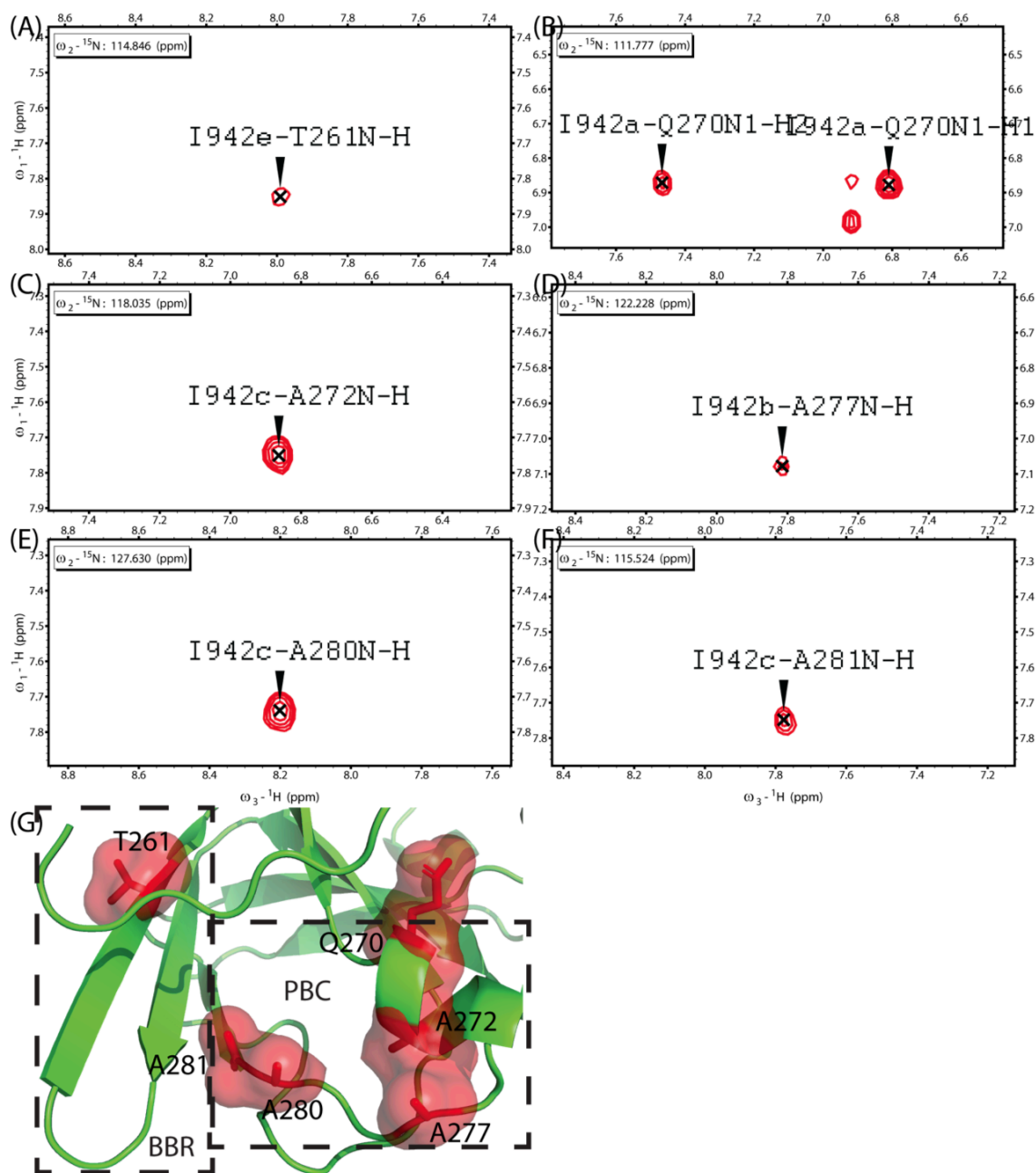
Figure 3.7 Intermolecular NOE peaks from the $^{13}C,^{15}N$-filtered NOESY-HSQC spectrum. (A-G) Spectral expansions showing the assigned intermolecular NOE cross-peaks. (H) 3D map of residues identified in NOESY-HSQC spectrum. Red surface indicates the presence of an NOE to I942 originating from the labelled residue.
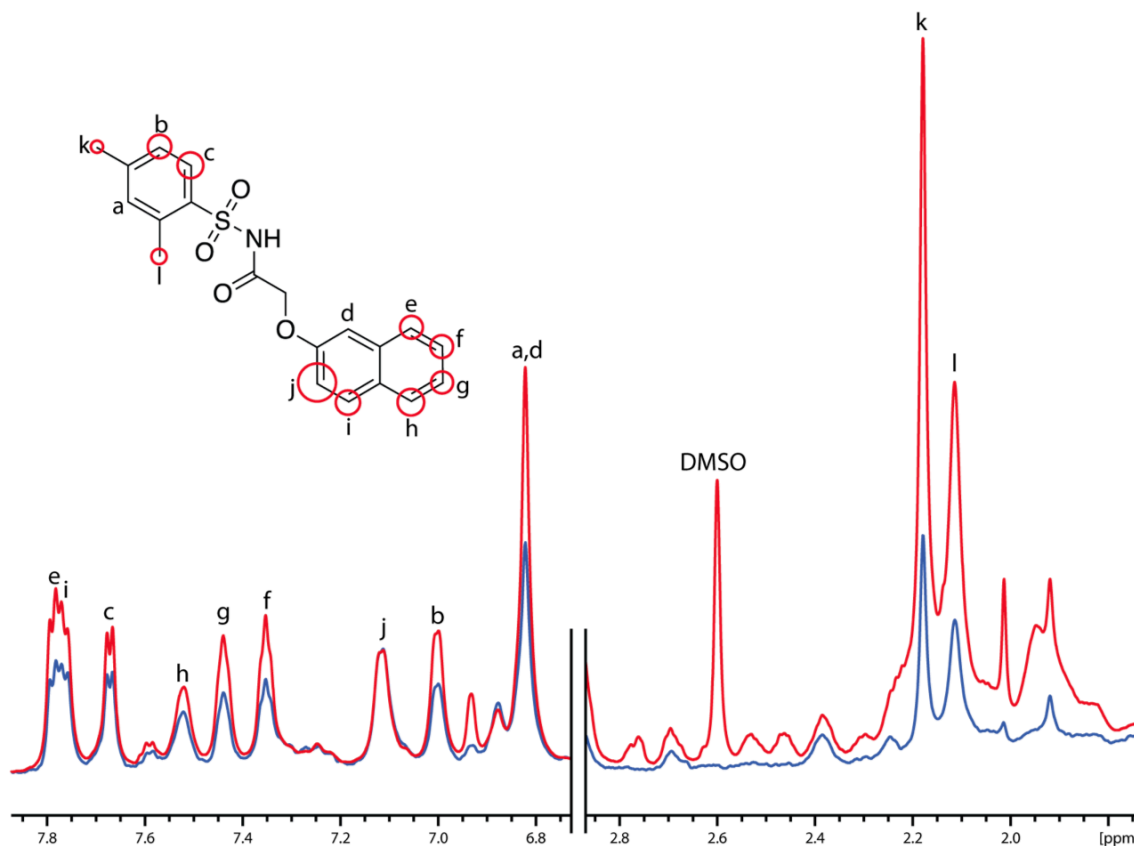
Figure 3.8 Saturation transfer difference and group epitope mapping for I942 binding to the EPAC1-CNB domain. 1D spectra of STR (red) and STD (blue) are overlayed with the STD spectrum rescaled so that the intensities of proton j in both spectra match. Proton j was selected as it exhibits the maximum STD/STR ratio. The assignments of the spectra are indicated through the labels in the molecular structure, whereas the radii of the red circles indicate the proximity of I942 protons to the EPAC1 surface, as gauged based on the normalized STD/STR ratios.
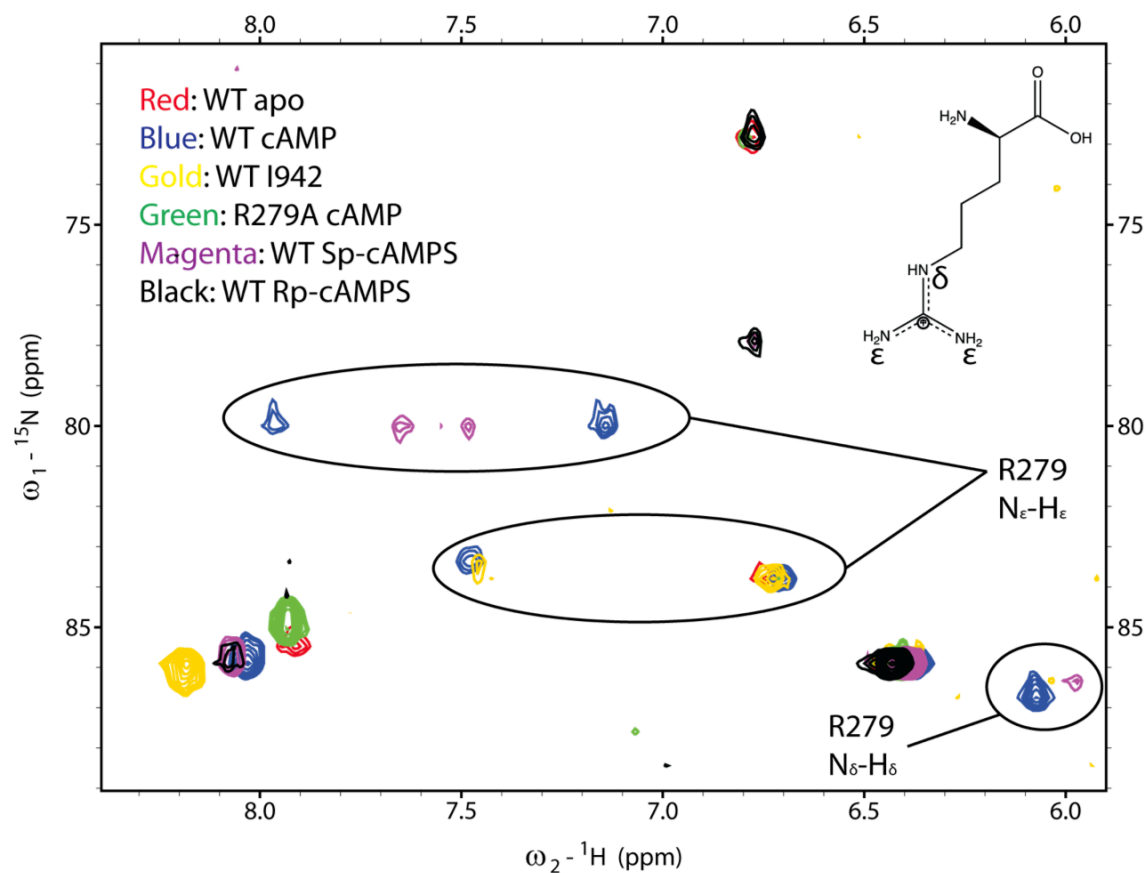
Figure 3.9 Guanidinium-HSQC spectra. The spectra overlay includes WT and R279A mutant of EPAC1-CNB domain in the apo form or saturated with different ligands, as per the legend in the spectra. The circled peaks are assigned to the N_δ-H_δ and N_ε-H_ε guanidinium moieties of Arginine 279.
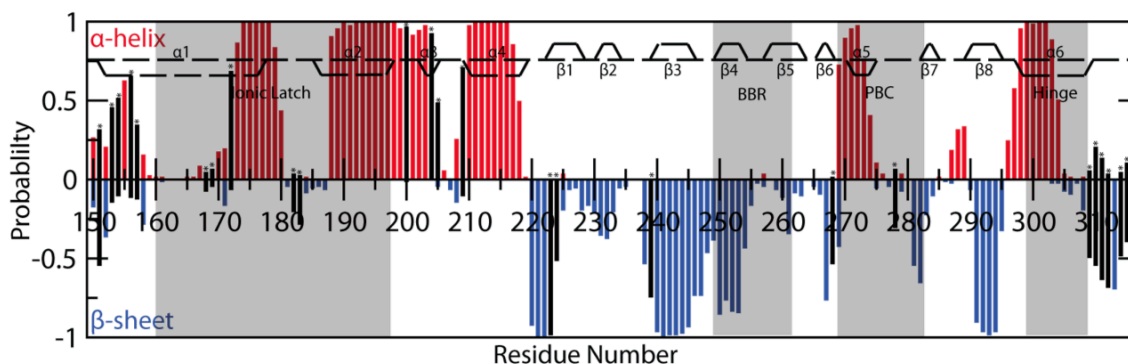
Figure 3.10 Protein Energetic Conformational Analysis from NMR (PECAN) chemical shift prediction of I942-bound EPAC1-CNB secondary structure. The secondary structure from the X-ray structure of apo EPAC1 is plotted along with the residue number. Red bars indicates the probability of residues forming an α-helix, while blue bars indicate the probability of residues forming a β-sheet. Residues without any assignment are marked with an asterick and the bars of such residues are marked in black.
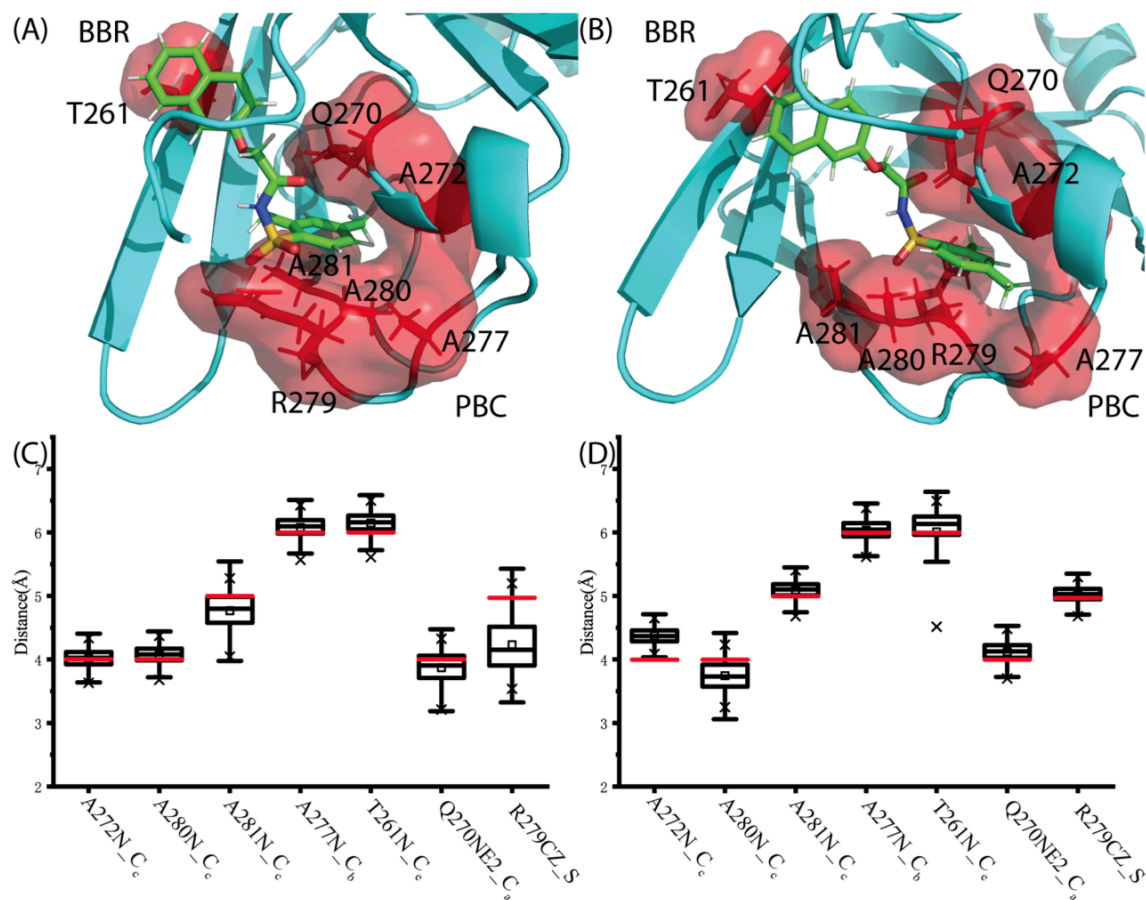
Figure 3.11 Representative simulated models of I942 bound EPAC1-CNB. (A,B) Simulated I942-bound EPAC1-CNB structures with restrainted residues illustrated as red surface. The simulation was performed starting from the apo (A) and cAMP-bound (B) EPAC1-CNB homology structures. (C,D) Distribution of distances between restrainted residues and I942 for the 300-ns MD trajectories starting from the inactive (C) and active (D) structures. The red line is the distance applied as upper limit restraint during MD simulations. In the box plots, the middle, bottom, and top lines of the box represent the median, 25th percentile and 75th percentiles, respectively. The whiskers are data falling with 1.5*IQR above the 75th percentile and below the 25th percentile; the small cubic box inside is the mean and two crosses represent the 1st and 99th percentiles of the data.
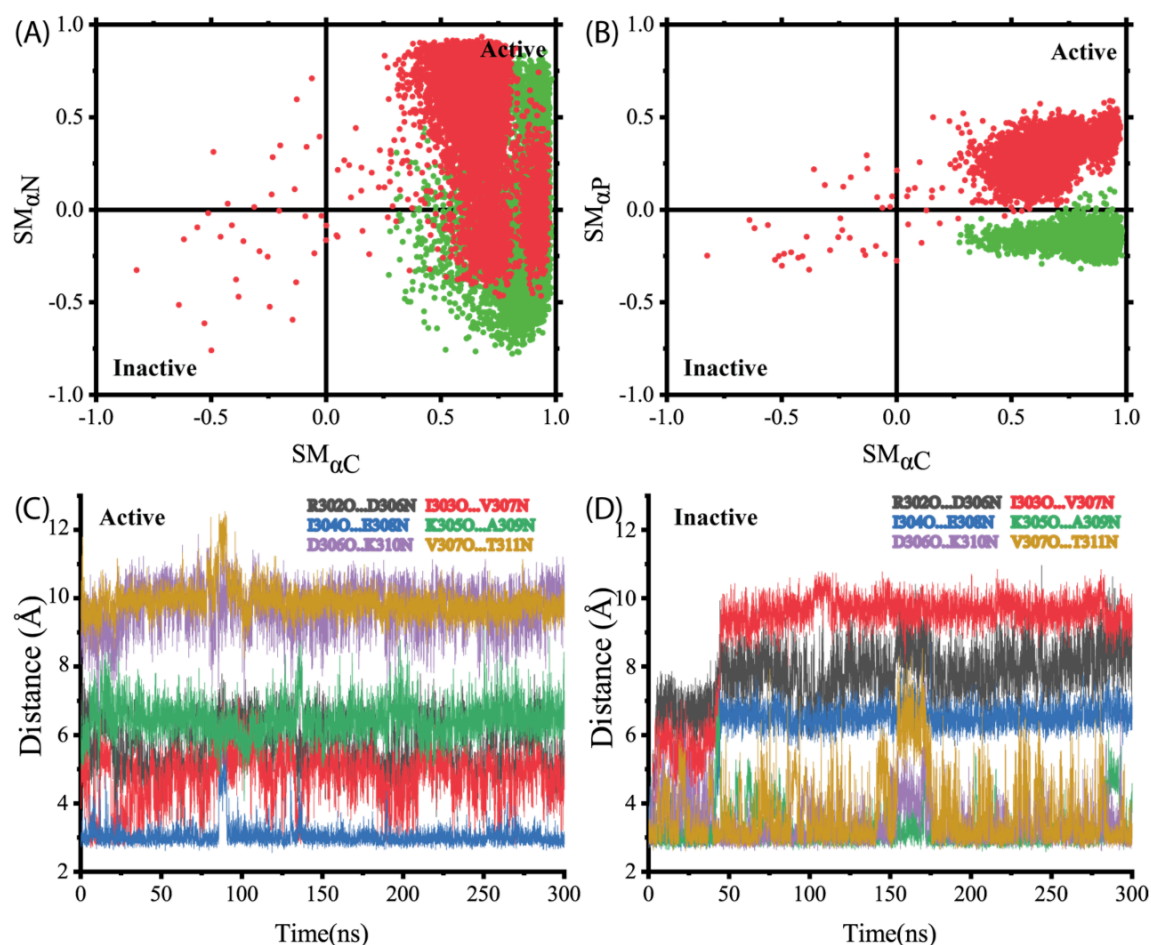
Figure 3.12 Similarity measures (SM) plots for the active versus inactive structures. (A, B) SM plots for the active versus inactive structures for the N terminal α-helices (A), PBC region α-helices (B) against C terminal α-helices (end at R305). Each quadrant represents different active *vs.* inactive combinations. Trajectories starting from the active (inactive) conformation of the EPAC1-CNB domain are shown in green (red). (C, D) the hydrogen bond interactions between residues in the C terminal helices (residue 305-310) of active (C) and inactive (D) states.
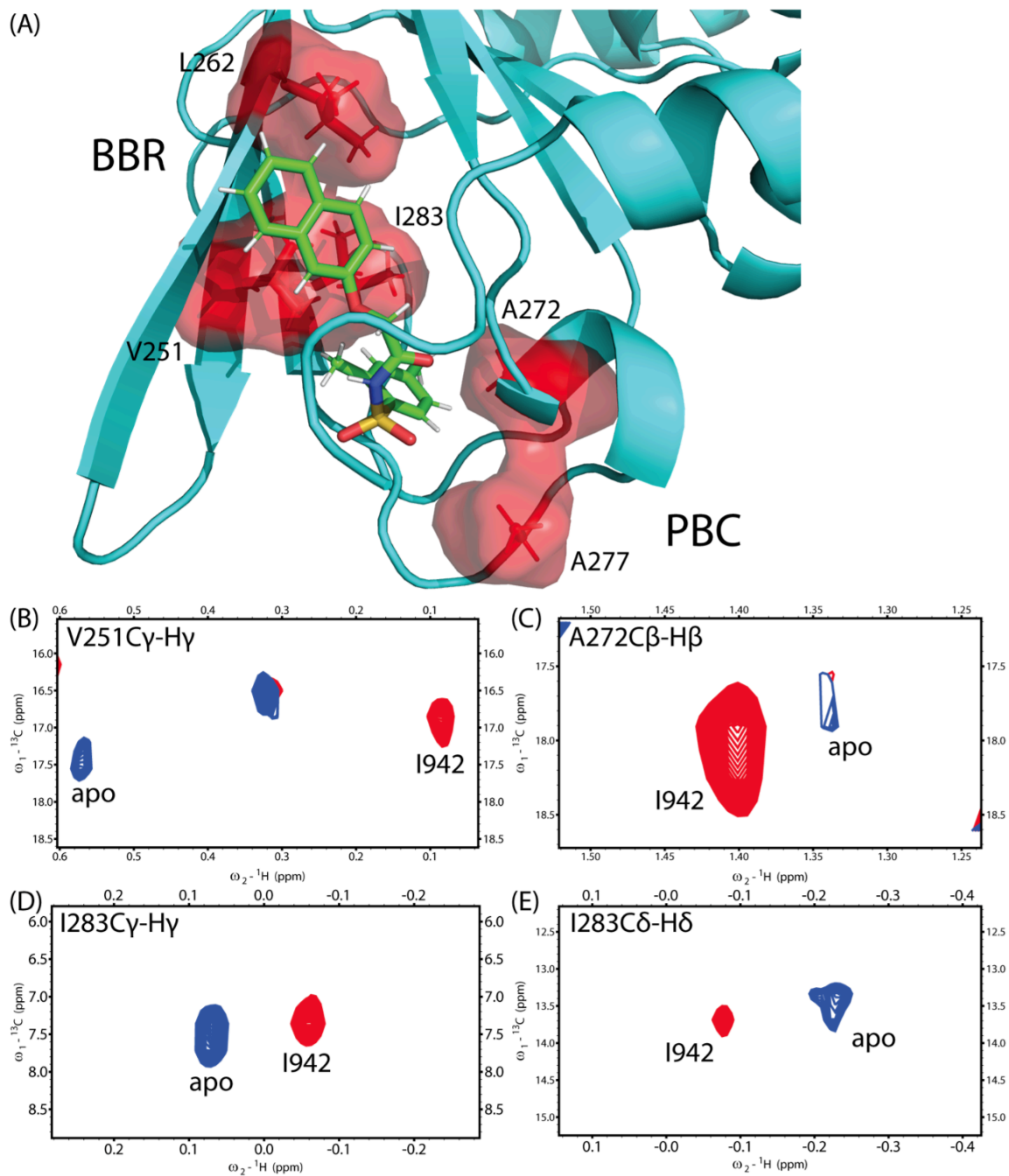
Figure 3.13 Visualization of STD-^{13}C-HSQC results. (A) 3D map of STD-^{13}C-HSQC results. Residues identified in Table 3.1 are mapped with red surface. (B-E) Representative 2D STD spectra of residues with significant chemical shifts.
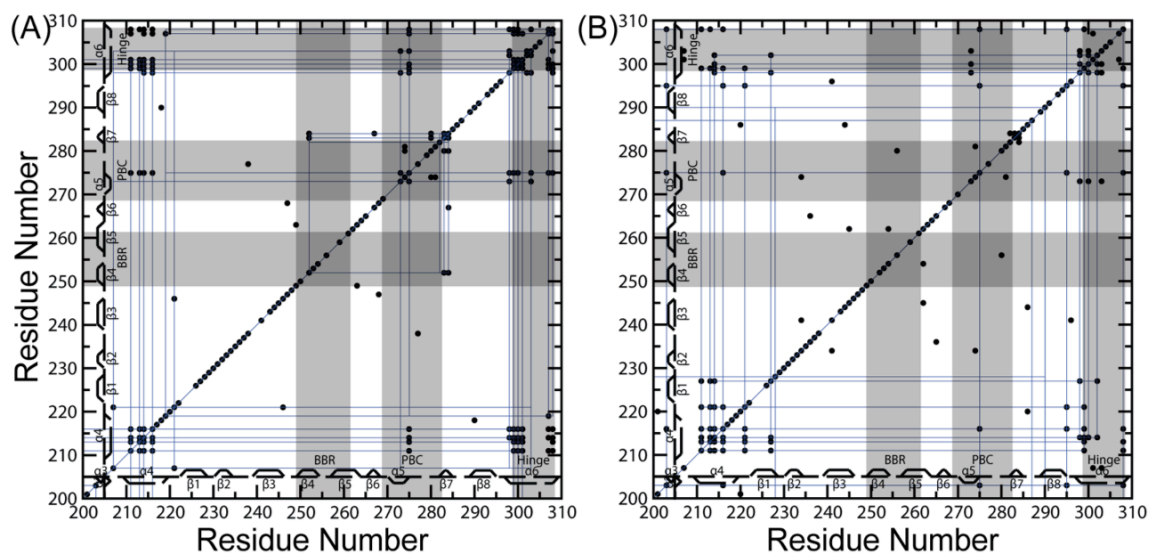
Figure 3.14 Chemical shift correlation matrices from CHESCA. All secondary structures are plotted along with residue number. Each point represents a residue pair with Pearson correlation coefficient ≥ 0.98 and residues identified to belong to the major cluster from agglomerative clustering are connected with blue lines. Each matrix includes apo, 2'-OMe-cAMP, Rp-cAMPS, Sp-cAMPS bound as well as DMSO-d$_6$ matched cAMP- (A) or I942- (B) bound EPAC1-CNB.

Figure 3.15 Representative pair-wise residue correlations from hinge-α4 helix allosteric network. (A), (C) and (E) represents correlations with cAMP in the CHESCA matrix and (B), (D) and (F) represents correlations with I942 in the CHESCA matrix.

Figure 3.16 Representative pair-wise residue correlations from hinge-PBC allosteric network. (A), (C) and (E) represents correlations with cAMP in the CHESCA matrix and (B), (D) and (F) represents correlations with I942 in the CHESCA matrix.
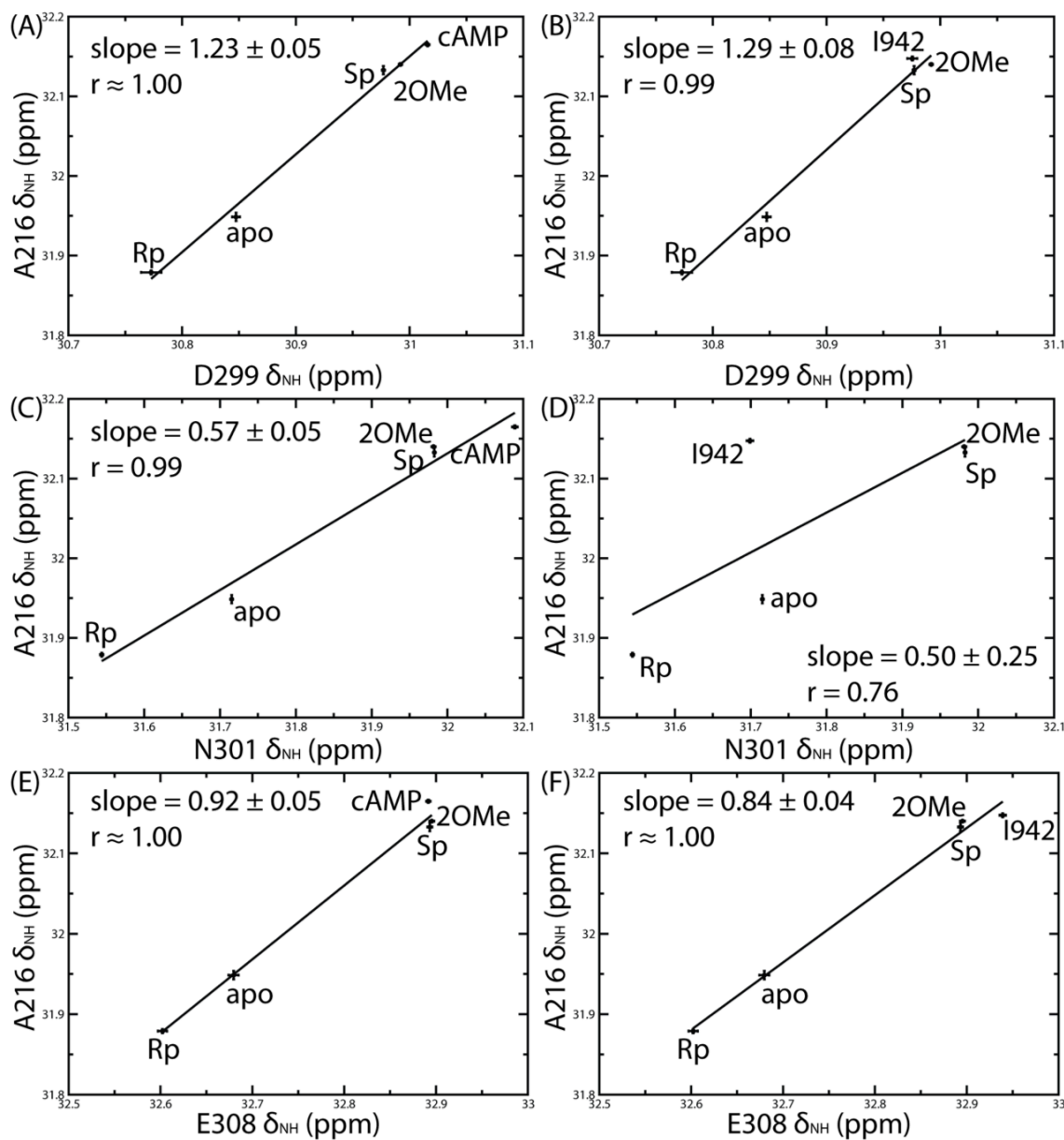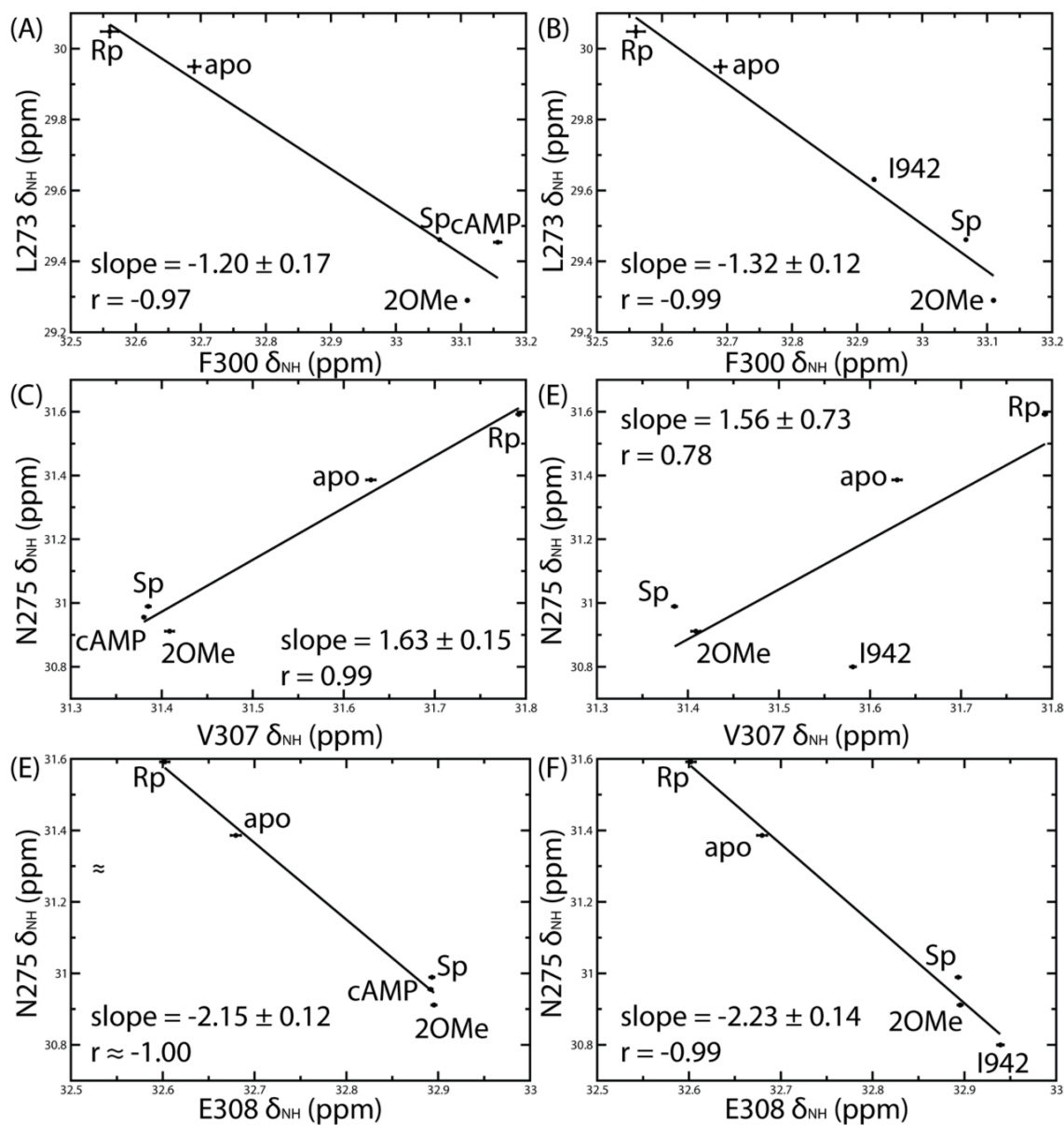
Chapter 4

Discussion and Proposal of a Mechanism for I942 - EPAC1 Binding and Partial Agonism

4.1 The Interaction between I942 and the EPAC1-CNB and the Subsequent Conformational Shifts

The conformation of I942 and EPAC1-CNB before and after interaction was examined by NOESY and CHESPA experiments, respectively. The I942 conformation before and after binding to EPAC1-CNB undergoes minimal changes as the NOE cross-peaks of both free and bound I942 are comparable to one another (Figure 3.6). The NOESY spectra of free and bound I942 also revealed that I942 remains in an "open-arm" conformation as no evidence was found of direct NOEs between the 2',4'-dimethylbenzyl moiety and the naphthalene ring. Since cAMP engages the PBC and BBR with the ribose ring and the adenine base respectively, and I942 displaces 8-NBD-cAMP causing a loss of 8-NBD-cAMP fluorescence intensity (Figure 3.1A), the "open-arm" conformation of I942 suggests that the 2',4'-dimethylbenzyl moiety and the naphthalene ring also interact with the two cAMP docking regions, PBC and BBR, distinctively. This result is independently confirmed by the chemical shift changes, the inter-molecular NOEs and the STD-HSQC data.

The protein conformational shift probed by CHESPA also reveals the inhibitory nature of I942 towards the cAMP-bound EPAC1-CNB. Similar to cAMP-bound EPAC1-CNB, the I942 interaction with EPAC1-CNB leads to significant chemical shifts

compared to apo EPAC1-CNB at the β2-β3 loop, BBR, PBC and hinge region (Figure 3.4B). However, when comparing the I942-bound and cAMP-bound EPAC1-CNB, there are differences caused by the two different ligands to EPAC1 (Figure 3.3A). The most significant differences are at the PBC. The differences indicate that while I942 displaces cAMP from the binding pocket, the PBC adopts different conformations when bound to the two ligands. Furthermore, the CHESPA fractional inhibition analysis reveals a strong inhibition at the PBC and hinge regions (Figure 3.4D). The inhibition indicates that I942 binding shifts these critical allosteric sites responsible for the release of EPAC1 autoinhibitory state partially back to their inactive states.

The partial inhibition emerging from the CHESPA data is in full agreement with the partial agonism observed for I942[1]. However, the CHESPA analysis also indicates that the extent of reversal from the active to the inactive state is highly residue dependent, suggesting that the partial agonism of I942 does not arise from a simple shift of the original two-state active *vs.* inactive conformational equilibrium previously proposed for EPAC[2–5]. It is likely that I942 stabilizes intermediates conformations in which selected elements of the active state are compromised or lost. For example, comparative chemical shift analysis clearly indicate that the hydrogen bonds with the amide of A272 and A280 in the PBC are significantly weaker in the I942-EPAC1 *vs.* the cAMP:EPAC1 complex (Figure 3.2B,C) and that I942 significantly perturbs the salt bridge with the allosterically critical guanidinium of R279 (Figure 3.9).

The intermolecular NOEs acquired through an isotope-filtered NOESY-HSQC include multiple NOE cross-peaks between the PBC and the 2',4'-dimethylbenzyl moiety

as well as cross-peaks between the BBR and the naphthalene ring, which confirms our speculation that the 2',4'-dimethylbenzyl moiety and the naphthalene ring binds with two different cAMP docking regions. The guanidinium-HSQC spectra indicate that only one N_ε-$H_{\varepsilon 2}$ group in the Arginine 279 residue is involved in the formation of a salt bridge with the sulfonyl group in I942, and that this N_ε-$H_{\varepsilon 2}$ group is different from the one engaged by the super-agonist Sp-cAMPS (Figure 3.9). The CHESCA analysis also indicates that I942 perturbs the allosteric couplings between the hinge helix and other pivotal elements of the EPAC1-CNB, *e.g.* the PBC (Figure 3.14).

Based on distance restraints from the NOE measurements and Guanidinium-HSQC experiments, MD simulation was performed starting from both inactive and active EPAC1-CNB homology models built using the EPAC2 crystal structures[3,4]. The simulation performed on the inactive structure captured the correct interaction between R279 guanidinium and I942 sulfonyl group according to the comparison between I942- and the Sp-cAMPS-bound EPAC1-CNB guanidinium HSQC. In addition, this simulation also captured the intermediate conformation of PBC and hinge region between active and inactive states. These results suggest that the simulations initiated from the inactive structure provide a better model of I942-bound EPAC1-CNB, as also expected considering that I942 only activates EPAC1 by approximately 20%[1]. In fact, the intermediate conformation between active and inactive states explains the partial agonism of I942 towards EPAC1.

4.2 The I942 Inhibition Mechanism of Action towards EPAC1

It is well known that cAMP binding to EPAC1 leads to a shift of the PBC and hinge helices orientations from "out" to "in", pointing away and to the β-barrel, respectively.[2–4] The out-to-in transitions induced by cAMP at the hinge region facilitate the displacement of the regulatory region away from the catalytic region, which in turn enables the catalytic site of EPAC to bind to Rap1 and promote GEF activity[6,7].

Based on the simulation performed on the inactive EPAC1-CNB homology model, an I942-bound EPAC1-CNB structure was proposed. The simulation captured the partial "in" conformation of PBC and hinge regions, the partial α6 helix unfolding predicted by PECAN based on the secondary chemical shifts, which is critical to release the catalytic region from the regulatory region and upregulate the GEF function of EPAC1.

When I942 is bound to EPAC1-CNB, it mimics cAMP and occupies the cAMP binding pocket, but comparing the binding of I942 and cAMP to EPAC1-CNB reveals that the critical hydrogen bonds between the backbone N-H of A272 and the equatorial oxygen atom of cAMP and between the backbone N-H of A280 and the axial oxygen atom of cAMP are disrupted (Figure 4.1A). Meanwhile, the salt bridge between the guanidinium N-Hs of R279 and the equatorial oxygen atom of cAMP is preserved by the interaction between the sulfonyl oxygens of I942 and the guanidinium N-Hs (Figure 4.1A). In addition, the interaction between side chain of V251 and the imidazole ring of the adenine base is preserved by I942 naphthalene binding (Figure 4.1A). The disruption

of the A272 and A280 to cAMP hydrogen bonds by I942 binding is crucial to explain the I942 partial agonism.

In summary, the 2,4-dimethylbenzyl group, the sulfonyl group and the naphthalene ring of I942 mimic the ribose ring, the cyclic phosphate group and the adenine base of cAMP, respectively (Figure 4.1C). Besides, through the disruption of hydrogen bonding between I942 and the PBC, I942 binding also disturbs the allosteric network between the PBC and the hinge region (Figure 4.1B), which controls EPAC1 activation upon cAMP binding. The allosteric network between the hinge region and the α4 helix is also disturbed by I942 binding (Figure 4.1B). The loss of both allosteric networks supports that the hinge region does not adopt a traditional "in"/"out" conformational equilibrium when the CNB is bound to I942, but rather starts to sample an intermediate conformation that is not fully active. Thus, when bound to I942, EPAC1 is partial active.

The mechanism of inhibition of I942 towards EPAC1 based on the available data described above is presented in Figure 4.2. In summary, the I942 replaces cAMP in the cAMP binding pocket of the EPAC1-CNB domain, which in turn leads to a significant conformational change at the PBC and hinge regions. The I942 *vs.* cAMP replacement induces a partial shift back of these regions from the "in" to "out" orientation and compromises the allosteric network between them, as indicated by comparative CHESCA analyses. While both the PBC and hinge region are in an intermediate state between the "in" and "out" conformation, the PBC is in direct contact with I942 and on average favors the "in" orientation more than the hinge region (Figure 3.4C). The differential in-to-out

transition of the PBC *vs.* hinge regions is consistent with the compromised allosteric couplings observed by CHESCA for the I942-bound EPAC1-CNB domain and is explained through the partial stabilization by I942 of a third intermediate with a PBC-in and hinge-out topology (Figure 4.2). Considering that the hinge-in orientation is necessary for full activation, such intermediate is expected to be inhibitory, thus rationalizing the partial agonism observed for I942 in GEF assays[1].

4.3 Mechanism of Action Comparison between I942 and Other Known EPAC1 Inhibitors

Two other inhibitors to EPAC1, CE3F4R and ESI-09, have been previously investigated by NMR. Both inhibitors are specific inhibitors at low concentrations. ESI-09 acts as a competitive inhibitor to EPAC1 and competes for the cAMP binding pocket with cAMP[8], whereas CE3F4R acts as an uncompetitive inhibitor to EPAC1 and binds to the EPAC1:cAMP complex at the α-, β-subdomain interface of the EPAC1-CNB, promoting a PBC "in", hinge region "out" inhibitory conformation[9]. However, the specific interactions of both inhibitors are significantly hindered by their low solubility and their aggregation-prone tendency. Specific inhibitory interactions with EPAC1 occurring at low ligand concentrations compete with non-specific effects arising from ligand aggregates formed at higher ligand concetrations.[10] At high concentrations, the inhibitor aggregates form and either absorb and inactivate EPAC1, as observed in the case of ESI-09, or serve as a ligand-sink, as reported in the case of CE3F4R.[10] I942 is significant more soluble than ESI-09 and CE3F4R and therefore it is more difficult for

I942 to form aggregates. Although the non-specific interaction between I942 and EPAC1 cannot be ruled out if the I942 reaches sufficiently high concentrations, the specific interactions between I942 and EPAC1 prevails over a wider concentration range compared to the other EPAC-specific inhibitors, CE3F4R and ESI-09. Interestingly, the mechanism of action of I942 is somewhat hybrid between those reported for CE3F4R and ESI-09. Similar to CE3F4R, I942 stabilizes the inhibitory PBC-in/hinge-out intermediate. However, rather than acting as an uncompetitive allosteric inhibitor, I942 compete with cAMP, similar to ESI-09.

4.4 References

(1)   Parnell, E.; McElroy, S. P.; Wiejak, J.; Baillie, G. L.; Porter, A.; Adams, D. R.; Rehmann, H.; Smith, B. O.; Yarwood, S. J. *Sci. Rep.* **2017**, *7*, 294.

(2)   Rehmann, H.; Prakash, B.; Wolf, E.; Rueppel, A.; de Rooij, J.; Bos, J. L.; Wittinghofer, A. *Nat. Struct. Biol.* **2003**, *10*, 26–32.

(3)   Rehmann, H.; Das, J.; Knipscheer, P.; Wittinghofer, A.; Bos, J. L. *Nature* **2006**, *439*, 625–628.

(4)   Rehmann, H.; Arias-Palomo, E.; Hadders, M. A.; Schwede, F.; Llorca, O.; Bos, J. L. *Nature* **2008**, *455*, 124–127.

(5)   Das, R.; Mazhab-Jafari, M. T.; Chowdhury, S.; SilDas, S.; Selvaratnam, R.; Melacini, G. *J. Biol. Chem.* **2008**, *283*, 19691–19703.

(6)   Kawasaki, H.; Springett, G. M.; Mochizuki, N.; Toki, S.; Nakaya, M.; Matsuda, M.; Housman, D. E.; Graybiel, A. M. *Science* **1998**, *282*, 2275–2279.

(7)   de Rooij, J.; Zwartkruis, F. J. T.; Verheijen, M. H. G.; Cool, R. H.; Nijman, S. M. B.; Wittinghofer, A.; Bos, J. L. *Nature* **1998**, *396*, 474–477.

(8)   Zhu, Y.; Chen, H.; Boulton, S.; Mei, F.; Ye, N.; Melacini, G.; Zhou, J.; Cheng, X. *Sci. Rep.* **2015**, *5*, 9344.

(9)   Boulton, S.; Selvaratnam, R.; Blondeau, J.-P.; Lezoualc'h, F.; Melacini, G. *J. Am. Chem. Soc.* **2018**, *140*, 9624–9637.

(10)   Boulton, S.; Selvaratnam, R.; Ahmed, R.; Van, K.; Cheng, X.; Melacini, G. *J. Med. Chem.* **2019**, *62*, 5063–5079.
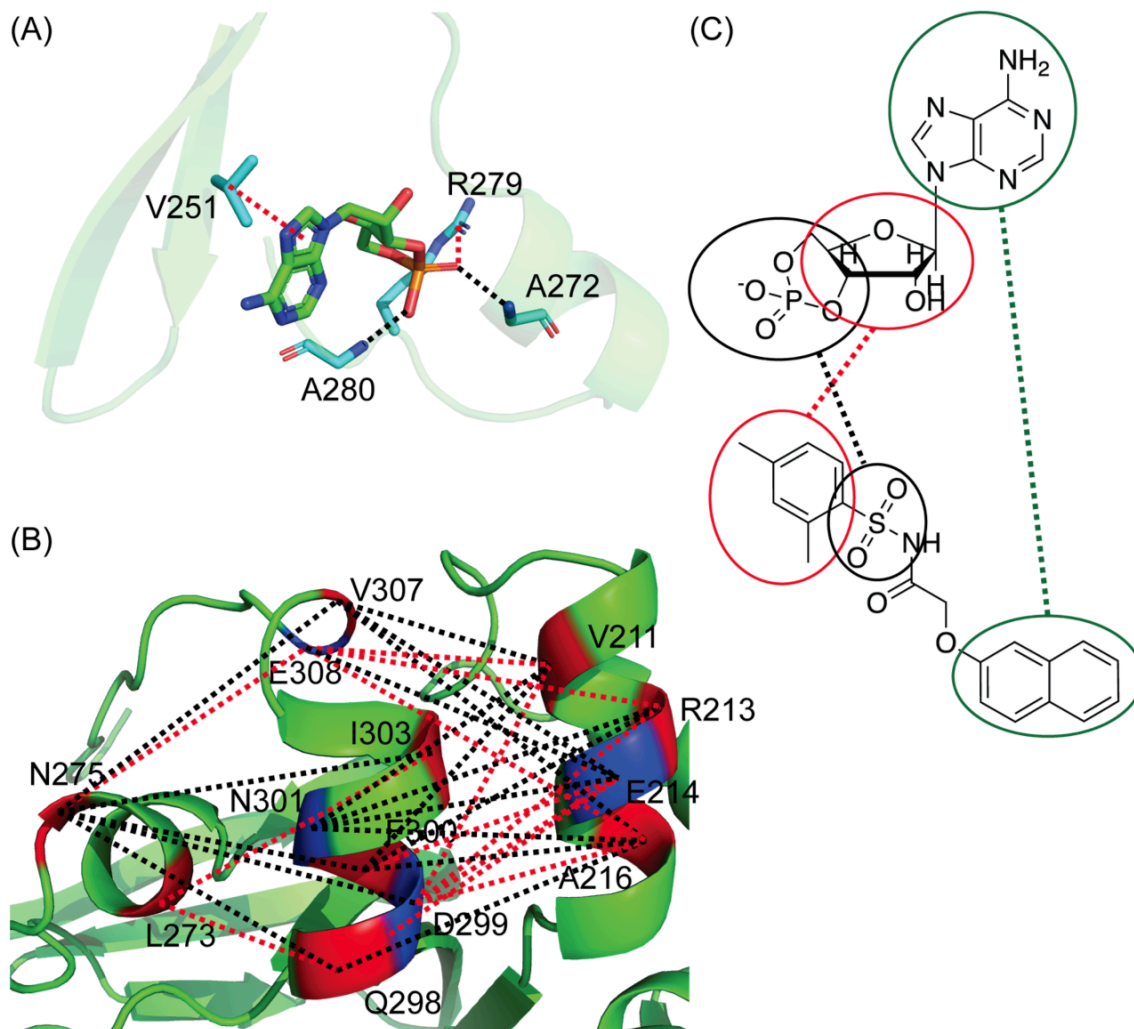
Figure 4.1 Illustration of interactions preserved or perturbed by I942 binding compared to cAMP binding. Interactions or correlations disrupted by I942 binding are depicted by black dashed lines and interactions preserved by I942 binding are shown as red dashed lines in the (A) interaction between cAMP and cAMP binding pocket and (B) allosteric network between α4 helix/α5 helix (PBC) and hinge region. (C) Molecular basis for the I942 *vs.* cAMP mimicry. Circle and dashed lines indicate how I942 mimics cAMP when bound to EPAC1.
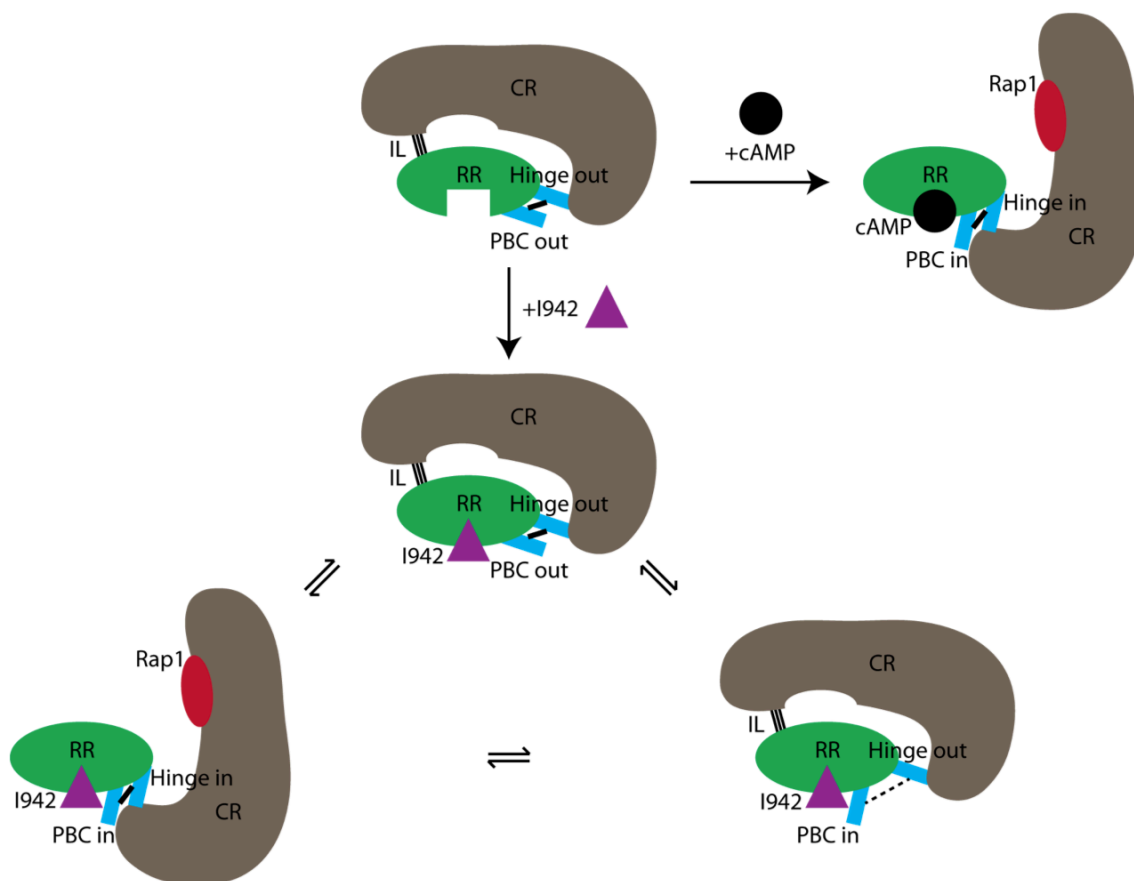
Figure 4.2 Proposed mechanism of action of I942 inhibition towards EPAC1. The scheme includes the activation of EPAC1 by cAMP binding and a three-stage equilibrium of I942-bound states of EPAC1.

Chapter 5

Conclusion and Future Directions on EPAC1 Specific Inhibitor

5.1 Conclusion of the Study

In this thesis, we established the binding and inhibition mechanism of I942 towards EPAC1. The interactions between I942 and EPAC1 were mapped through intermolecular NOEs and molecular dynamics (MD) simulation. I942 was found able to engage the BBR and PBC in EPAC1-CNB and recruit the PBC to the "in" conformation similar to cAMP. When the PBC is shifted to the "in" active conformation by I942, the hinge region on the other hand, does not fully rotate to the "in" conformation typical of the cAMP-bound state. Instead, the hinge helix undergoes a shift to an intermediate state between the "in" and "out" conformation, explaining the partial agonism observed for I942 based on guanine exchange enzymatic assays.[1]

5.2 Future Directions on EPAC1 Specific Inhibitors

Over the years, the mechanisms of action of multiple EPAC inhibitors have been dissected, including the EPAC1 specific uncompetitive inhibitor CE3F4R[2], the EPAC non-isoform specific competitive inhibitor ESI-09[3] as well as the aggregation-based EPAC non-specific interaction of both ESI-09 and CE3F4R[4]. In this thesis, we examined the mechanism of action of an EPAC1 specific competitive inhibitor I942 through NMR spectroscopy, fluorescence and MD simulations. However, some questions still remain unanswered regarding I942. In addition, our work on I942 opens new directions for future

investigations on EPAC1 inhibition. In this chapter, we will review the currently open questions on I942 as well as future opportunities for further I942-related lead development.

5.2.1 Further Refinement of I942-Bound EPAC1-CNB Model by MD Simulation

Although the current model of I942-bound EPAC1-CNB reflects most of the features of the I942 inhibition of EPAC1 as revealed by NMR data, it needs further refinement. The current MD simulated model of I942-bound EPAC1-CNB structure was created with a total length of 300 ns of MD simulation and a total length of 1 us would be more accurate for the simulation model. Another concern for the EPAC1 construct used in the simulation is that, while the hinge region has been proven pivotal in I942 inhibition, the hinge region is on the C-terminus of the input protein construct. So, not only the structure of the hinge region is subjected to I942 binding, but also being located at the C-terminus of the input protein structure makes the hinge region more flexible, which adds to the uncertainty of the hinge region structure and leads to a less accurate I942-bound EPAC1-CNB model. A longer EPAC1 model at the C-terminus should be inputted to the MD simulation to minimize the flexibility of the hinge region.

5.2.2 I942 EPAC Isoform 1 versus 2 Specificity

As discussed in Chapter 1.1, the two major isoforms of EPAC, *i.e.* 1 and 2, have different tissue distributions and functionalities[5]. So, it is important to determine the isoform specificity when screening inhibitors for EPAC to target different diseases. The

studies described in Chapter 2-4 are specifically focused on EPAC1 since I942 was discovered to function as an EPAC1 specific partial agonist.[1] Evidence suggested that I942 has lower binding affinity towards EPAC2 than EPAC1 and introduces much higher agonistic guanine exchange factor (GEF) activity on EPAC1 over EPAC2.[1] So it is important to determine the structural differences between EPAC 1 and 2 that contribute to this binding and functional specificity.

One of the major differences between the EPAC isoforms is the PBC residue glutamine 270 on EPAC1 (or lysine 405 on EPAC2)[2,6]. Hence, we performed the CHESPA analysis of the Q270K EPAC1-CNB mutant bound to I942 (Figure 5.1). Major WT:I942 *vs.* Q270K:I942 chemical shift differences are identified at the PBC and hinge regions as well as the N-terminal alpha helical bundle (Figure 5.1B). This could mean that I942 binding to EPAC2 could potentially disengage the PBC-hinge allosteric interaction and prevent the release of the catalytic region from the regulatory region to keep EPAC2 in its auto-inhibited state. However, triple resonance experiments are needed to fully assign the hinge region to support such hypothesis. In addition, it is also possible that the Q270K lowers the affinity for I942 and therefore the K_d for this mutant should be measured in the future.

5.2.3 I942 Interaction with Other Cyclic Nucleotide Binding Domains

Besides EPAC, kinases and ion channels are also regulated by homologous cyclic nucleotide binding domains. Due to the similarity in structures and mechanisms of action of the cyclic nucleotide binding domains of EPAC, cAMP-dependent Protein Kinase

(PKA), cGMP-dependent Protein Kinase (PKG) and Hyperpolarization-activated Cyclic Nucleotide-modulated channels (HCN)[7], it is possible that I942 also binds with other eukaryotic CNBs. However, kinase assays indicate that PKA activity remains unaffected by addition of I942.[1] This means even if I942 mimics cAMP in its binding to EPAC1, it is specific towards the CNB on EPAC *vs.* PKA. Another candidate to I942 binding is PKG, for which cAMP is a partial agonist[8]. Addition of 10-fold excess of I942 to PKGIβ CNB-B, which is critical for PKG activation, caused only subtle chemical shifts in the HSQC spectrum (Figure 5.2), suggesting weak and possibly non-specific binding of I942 to PKGIβ CNB-B. Other CNB domains, such as those of HCN or other isoforms and domains of PKG, remain to be examined. Even though both PKA and PKG are not candidates for I942 specific binding, understanding why I942 does not bind or not bind specifically to these CNBs will significantly facilitate the future design of EPAC selective inhibitors.

5.2.4 Non-specific Interactions of I942 with EPAC1

Aggregation-prone ligands that act as enzyme-specific inhibitors at low concentrations may form large aggregates in solution at higher concentration. Such ligand-aggregates are notorious for their non-specific inhibitory action through adsorption of target proteins. A notable example of this type of non-specific inhibition involving EPAC is ESI-09[3,4]. Though relatively more soluble compared to ESI-09, I942 still exhibits a limited solubility in aqueous buffers and may promote non-specific interaction with EPAC1 at high concentrations.

Due to the relative high solubility and high affinity of I942 towards EPAC1, the non-specific interactions might co-exist with specific interaction with EPAC1. One strategy to dissect specific *vs.* non-specific binding effects is to utilize site-directed mutagenesis to silence the I942-EPAC1 specific interactions. For example, the R279A mutant described in Chapters 2 and 3 eliminates the binding between the R279 side chain guanidinium and the sulfonyl group of I942. Thus, the specific interaction between I942 and EPAC1 is significantly hindered.

The CHESPA fractional activation plot (Figure 5.3B) indicates that the majority of residues on EPAC1-CNB R279A mutant shift to the inhibited state. However, this is not without exceptions. The "active" residues concentrate in three regions that precede the PBC and the hinge helix and a few residues fall in the hinge region. The "active" regions may reflect interactions with I942 independently of the PBC, suggesting either there is a secondary binding site apart from the cAMP binding pocket or there are weak non-specific interactions between EPAC1 and I942. Triple resonance experiments are needed to fully assign the R279A spectra and pursue this direction further. Another approach is to use some less invasive mutations but with the risk of not fully eliminating cAMP (or I942) binding capability. The aggregation-based non-specific interaction could also be investigated with STD experiments and dynamic light scattering.

5.2.5 CE3F4R as an Uncompetitive Inhibitor towards I942

I942 is a competitive inhibitor to EPAC1 that partially mimics cAMP when bound to EPAC1-CNB. It is also known that another small molecule CE3F4R forms a

EPAC1:cAMP:CE3F4R ternary complex and acts as an uncompetitive inhibitor.[2,9–11] So, it is speculated that CE3F4R may interact with the EPAC1:I942 binary complex similar to the EPAC1:cAMP complex, *i.e.* we hypothesize that CE3F4R may function as an uncompetitive inhibitor against I942-bound EPAC1. If so, the combined inhibition effect of both inhibitors offers a new direction in EPAC based drug design.

To test our hypothesis about I942 and CE3F4R, we implemented CHESPA to analyze the inhibitory effect of CE3F4R on I942-bound EPAC1-CNB (Figure 5.4). 250 μM of I942 was added to 100 μM of EPAC1-CNB to represent I942-bound EPAC1-CNB, and 200 μM of CE3F4R was later added to the mixture. The chemical shifts caused by CE3F4R relative to I942-bound EPAC1-CNB (Figure 5.4B) is reduced relative to what previously reported for cAMP under similar experimental conditions.[2] However, the fractional activation plot indicates that the EPAC1:I942 complex is systematically shifting towards inhibited state (Figure 5.4C). These shifts should be compared to those observed upon addition of CE3F4R to apo EPAC. Optimization of both the I942 and CE3F4R structures may amplify this inhibition effect arising from the synergy between I942 and CE3F4R.

5.2.6 I942-like EPAC Ligands: Compound I178

Along with I942, another compound that inhibits the cAMP-dependent activation of EPAC1 GEF activity, yet with weaker agonistic potential, was discovered and named I178[1] (Figure 5.5). The main difference between I942 and I178 is that the two methyl groups on the 2',4'-dimethylbenzyl moiety are missing in I178. Like I942, I178 exhibits

higher affinity towards EPAC1 than EPAC2 and it elicits significantly less GEF activity than cAMP when bound to EPAC1. It will be interesting to see the extent of involvement of the two methyl groups on I942 in EPAC1 binding. Another direction for this compound is to add other functional groups to the benzene ring to determine the optimal structure of I942 derivatives for EPAC1 inhibition. In summary, the synthesis of a second-generation library of I942 derivatives will enable the determination of structure-activity relationships (SAR) through further NMR and functional characterizations and will help further refine the model of the I942:EPAC1-CNB domain complex. For example, such second-generation library of functionally annotated I942 derivatives will serve as perturbation set for new implementations of CHESCA, which will define binding *vs.* allosteric clusters. Furthermore, the differential chemical shift changes of the EPAC1 CNB domain induced by I942 *vs.* I178 may help further locate the EPAC1 residues interacting with the methyl groups of I942. Overall, the second-generation library of I942 derivatives will provide valuable additional insight into the mechanism of action of I942.

5.2.7 New EPAC1 Inhibitors: The Non-competitive Inhibitor AM-001

More recently, another EPAC1-specific inhibitor was discovered by Laudette *et al.*[12] This compound, named AM-001, was discovered through a bioluminescence resonance energy transfer assay and determined to function as a non-competitive inhibitor for EPAC1.[12] As AM-001 does not compete with cAMP for the binding pocket on EPAC1-CNB, we hypothesize that it will bind with another region on EPAC1 capable of triggering the conformational shift of EPAC1 to the inactive state. Hence, it is vital to

pinpoint the binding pocket of AM-001 to understand the mechanism of action of AM-001. However, a major challenge in applying NMR experiments to profile the AM-001-EPAC1 interactions is that AM-001 is less soluble even than ESI-09 and CE3F4R in aqueous solutions and the compound stock solution in DMSO precipitates when diluted in NMR experiment buffer to as low as 200 µM. In fact, AM-001 has only around 60 µM solubility in aqueous buffer.[12] This means that there is only a very narrow concentration window left for NMR experiment. To remedy this limit, the emulsifiers like Kolliphor used in the original AM-001 *in vivo* study[12] could be used to improve the solubility. However, the effect of Kolliphor on NMR experiments is currently unknown, and it could interfere with NMR data acquisition. Further investigations of the optimum Kolliphor/buffer ratio need to be determined. Due to the limited solubility of AM-001, the filtered/edited NOESY-HSQC approach utilized in the study of I942 might not be suitable for AM-001. Alternative NMR approaches are paramagnetic relaxation enhancement (PRE) experiments similar to the NMR study of CE3F4R.[2] After evaluating the preliminary chemical shift data and CHESPA, the approximate location of the binding pocket could be identified, and multiple cysteine mutants for MTSL spin-labels should be placed within ~15-20 Å from the suspected pocket so that the binding pocket for AM-001 could be pinpointed through triangulation.

5.3 References

(1)   Parnell, E.; McElroy, S. P.; Wiejak, J.; Baillie, G. L.; Porter, A.; Adams, D. R.; Rehmann, H.; Smith, B. O.; Yarwood, S. J. *Sci. Rep.* **2017**, *7*, 294.

(2)   Boulton, S.; Selvaratnam, R.; Blondeau, J.-P.; Lezoualc'h, F.; Melacini, G. *J. Am. Chem. Soc.* **2018**, *140*, 9624–9637.

(3)   Zhu, Y.; Chen, H.; Boulton, S.; Mei, F.; Ye, N.; Melacini, G.; Zhou, J.; Cheng, X. *Sci. Rep.* **2015**, *5*, 9344.

(4)   Boulton, S.; Selvaratnam, R.; Ahmed, R.; Van, K.; Cheng, X.; Melacini, G. *J. Med. Chem.* **2019**, *62*, 5063–5079.

(5)   Kawasaki, H.; Springett, G. M.; Mochizuki, N.; Toki, S.; Nakaya, M.; Matsuda, M.; Housman, D. E.; Graybiel, A. M. *Science* **1998**, *282*, 2275–2279.

(6)   Schwede, F.; Bertinetti, D.; Langerijs, C. N.; Hadders, M. A.; Wienk, H.; Ellenbroek, J. H.; de Koning, E. J. P.; Bos, J. L.; Herberg, F. W.; Genieser, H.-G.; Janssen, R. A. J.; Rehmann, H. *PLOS Biol.* **2015**, *13*, e1002038.

(7)   Rehmann, H.; Wittinghofer, A.; Bos, J. L. *Nat. Rev. Mol. Cell Biol.* **2007**, *8*, 63–73.

(8)   VanSchouwen, B.; Selvaratnam, R.; Giri, R.; Lorenz, R.; Herberg, F. W.; Kim, C.; Melacini, G. *J. Biol. Chem.* **2015**, *290* (48), 28631–28641.

(9)   Courilleau, D.; Bisserier, M.; Jullian, J.-C.; Lucas, A.; Bouyssou, P.; Fischmeister, R.; Blondeau, J.-P.; Lezoualc'h, F. *J. Biol. Chem.* **2012**, *287*, 44192–44202.

(10)   Courilleau, D.; Bouyssou, P.; Fischmeister, R.; Lezoualc'h, F.; Blondeau, J.-P. *Biochem. Biophys. Res. Commun.* **2013**, *440*, 443–448.

(11)   Sonawane, Y. A.; Zhu, Y.; Garrison, J. C.; Ezell, E. L.; Zahid, M.; Cheng, X.; Natarajan, A. *ACS Med. Chem. Lett.* **2017**, *8*, 1183–1187.

(12)   Laudette, M.; Coluccia, A.; Sainte-Marie, Y.; Solari, A.; Fazal, L.; Sicard, P.; Silvestri, R.; Mialet-Perez, J.; Pons, S.; Ghaleh, B.; Blondeau, J.-P.; Lezoualc'h, F.
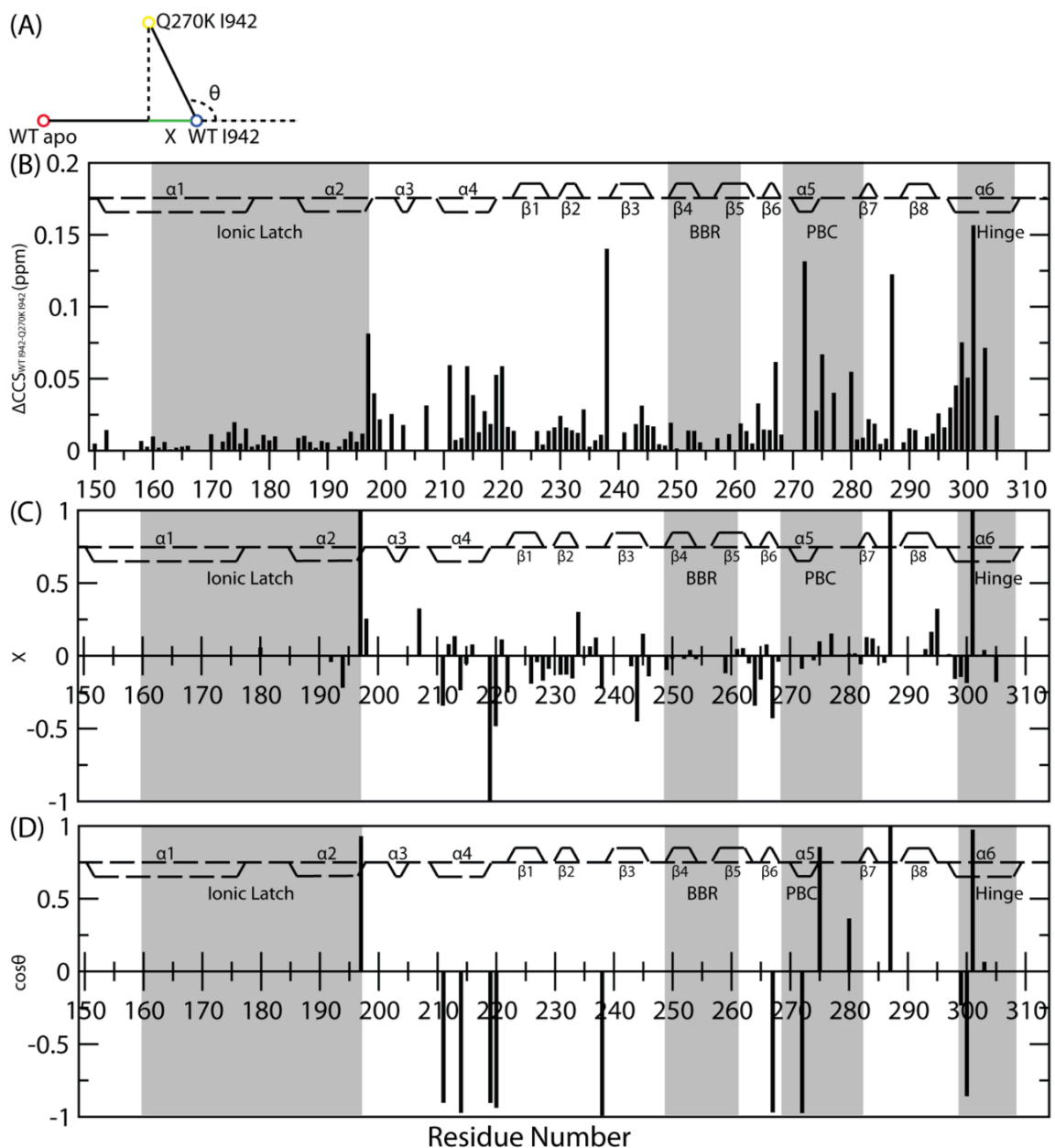
Cardiovasc. Res. **2019**, cvz076.

Figure 5.1 CHESPA analysis of I942 bound EPAC1-CNB Q270K mutant. All figures include secondary structure plotted along with residue number. Any value greater than 1 or lower than -1 are off scale. (A) Scheme of CHESPA analysis. (B) Compounded chemical shifts (CCS) from I942 bound wild-type to Q270K EPAC1-CNB. (C) Fractional activation (X) and (D) $\cos\theta$ of I942 bound Q270K compared to WT.
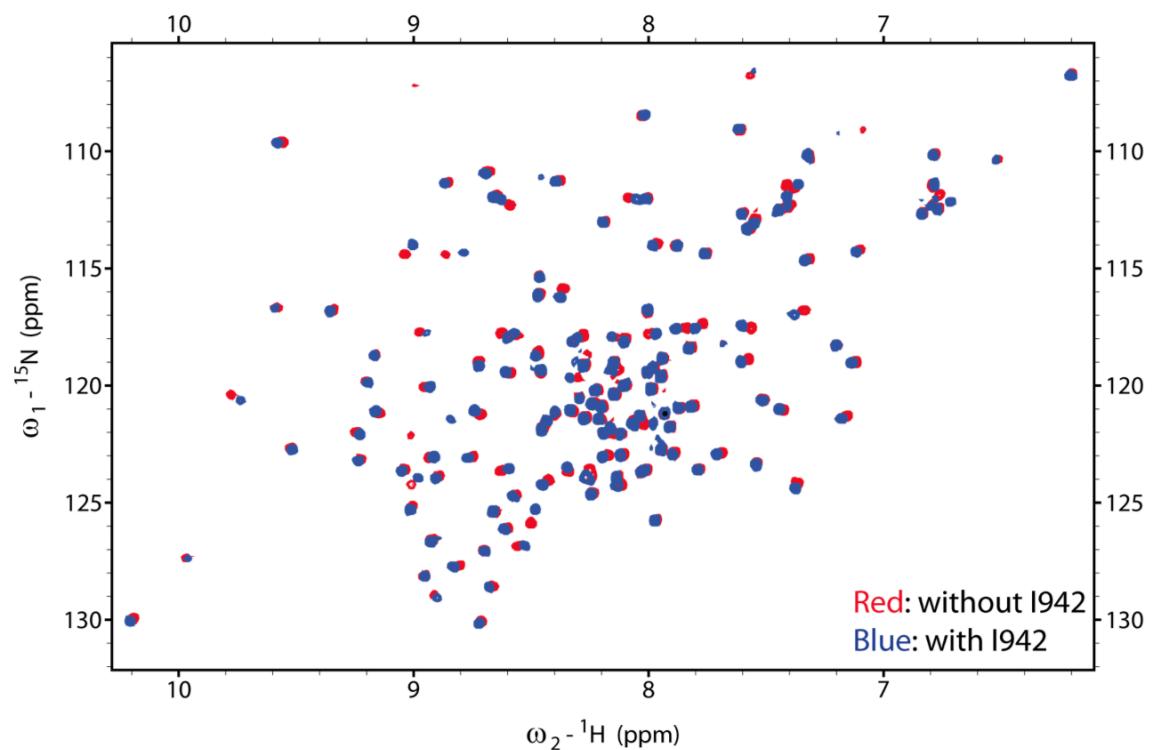
Figure 5.2 HSQC spectra overlay of PKGIβ CNB-B in the absence and presence of 10-
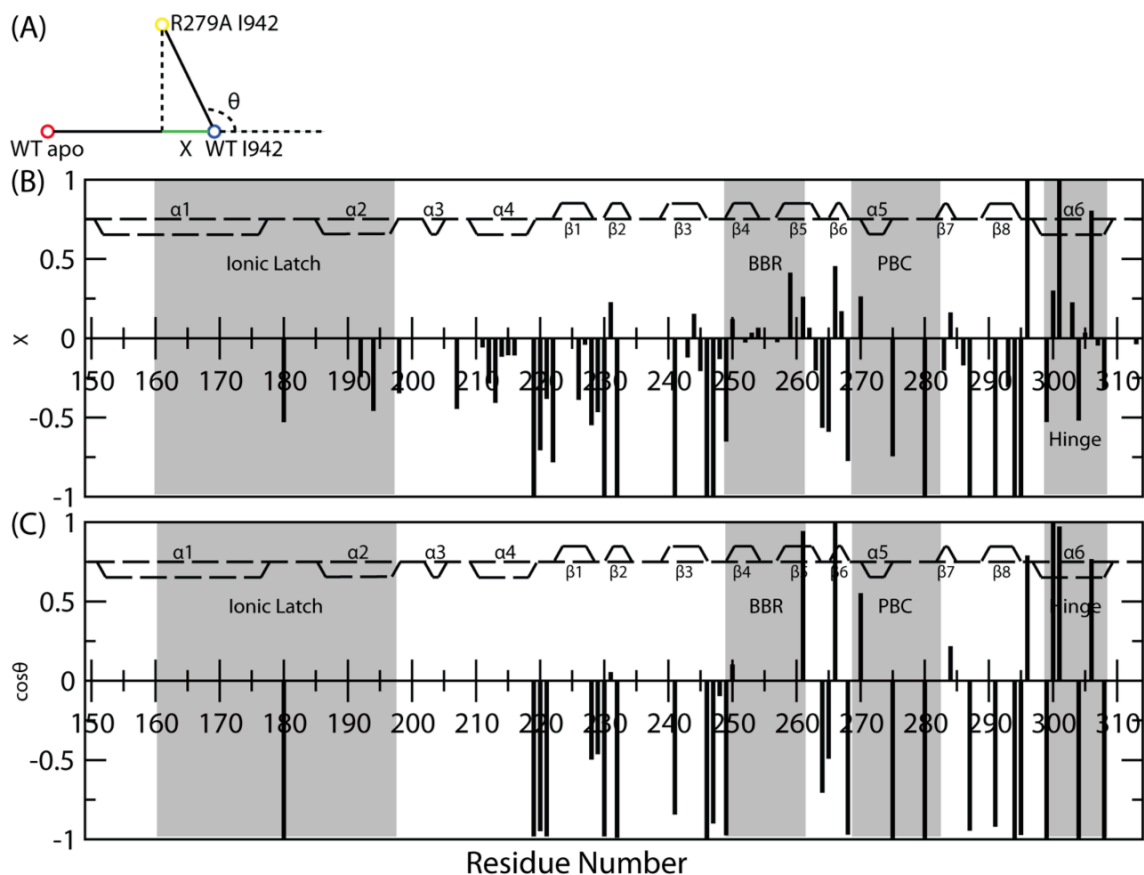
fold I942 excess.

Figure 5.3 CHESPA analysis of I942 bound EPAC1-CNB R279A mutant. All figures include secondary structure plotted along with residue number. Any X value greater than 1 or lower than -1 is off scale. (A) Scheme of CHESPA analysis. (B) Fractional activation (X) and (C) cosθ of the I942-bound R279A mutant compared to I942 bound WT EPAC1-CNB.
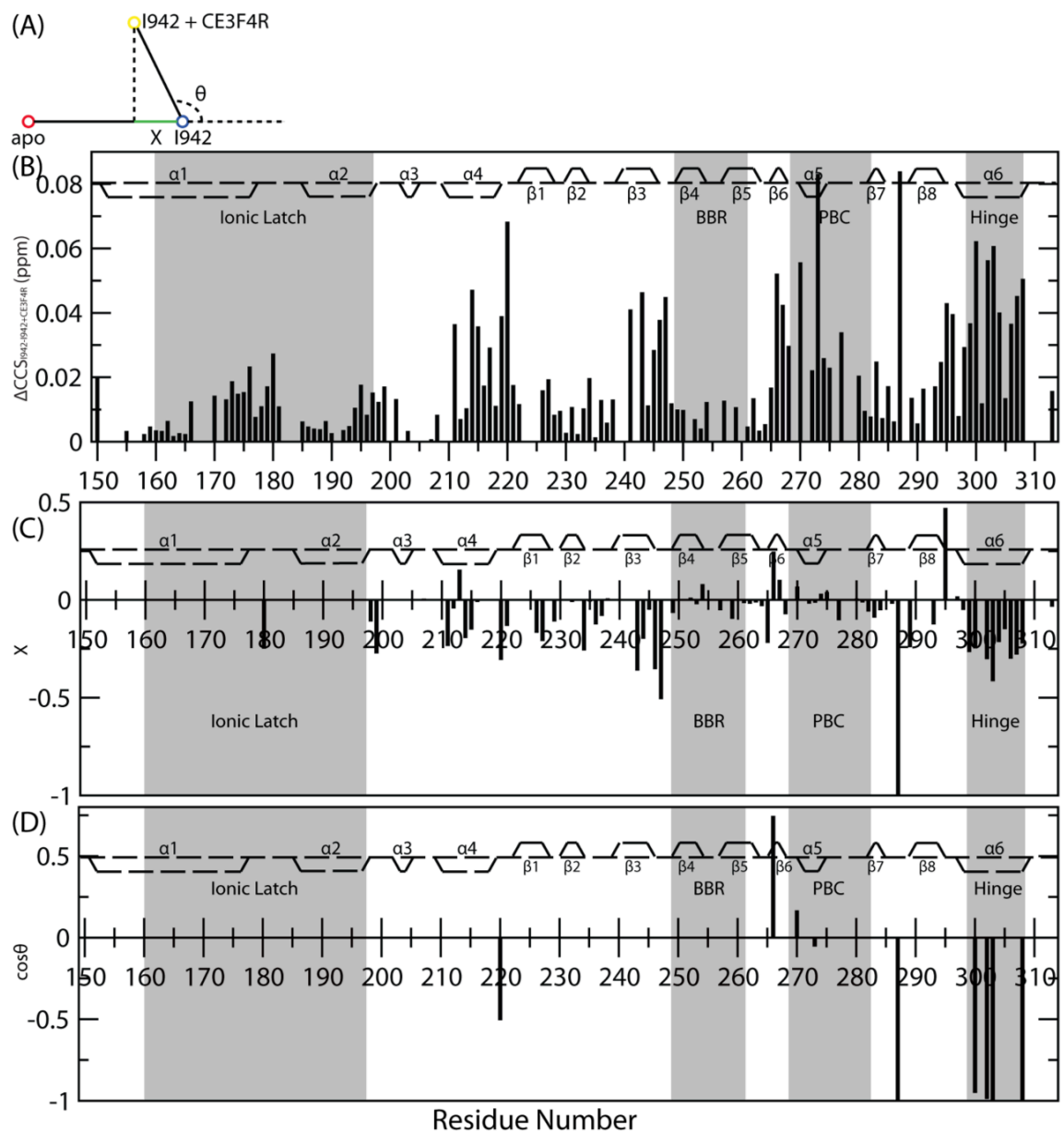
Figure 5.4 CHESPA analysis of CE3F4R uncompetitive inhibiting I942. All plots include secondary structure plotted along with residue number. Any X lower than -1 are off scale. (A) Scheme of CHESPA vectors. (B) Compounded chemical shifts (CCS) between the I942-bound and I942 and CE3F4R-bound EPAC1-CNB domain. (C) Fractional activation (X) and (D) cosθ of I942 and CE3F4R-bound compared to I942 only EPAC1-CNB.
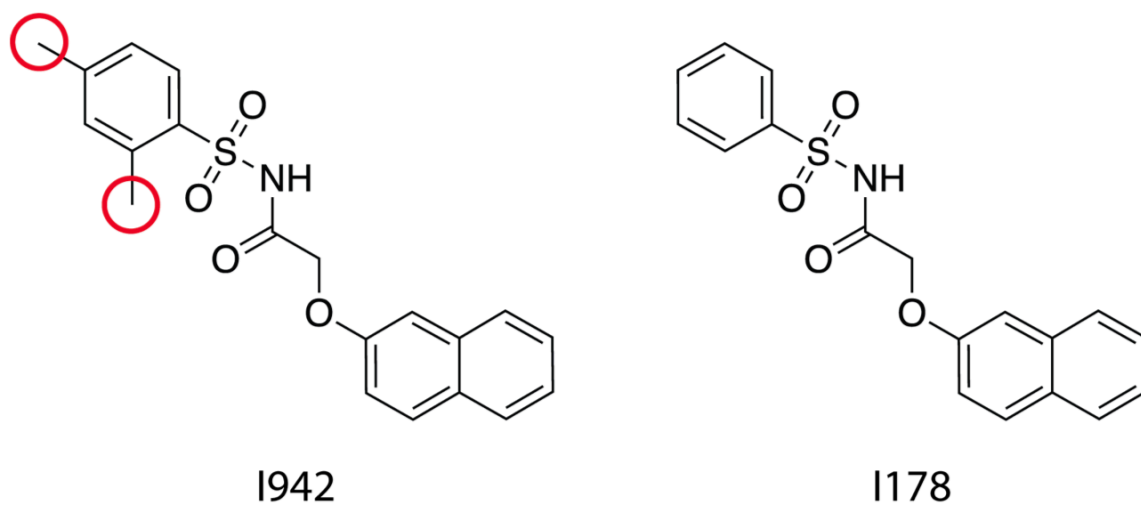
Figure 5.5 Structrual comparison between I942 and I178, another EPAC1-selective

partial agonist.[1]